INFORMATION TO USERS

This manuscript has been reproduced from the microfilm master. UMI films the text directly from the original or copy submitted. Thus, some thesis and dissertation copies are in typewriter face, while others may be from any type of computer printer.

The quality of this reproduction is dependent upon the quality of the copy submitted. Broken or indistinct print, colored or poor quality illustrations and photographs, print bleedthrough, substandard margins, and improper alignment can adversely affect reproduction.

In the unlikely event that the author did not send UMI a complete manuscript and there are missing pages, these will be noted. Also, if unauthorized copyright material had to be removed, a note will indicate the deletion.

Oversize materials (e.g., maps, drawings, charts) are reproduced by sectioning the original, beginning at the upper left-hand corner and continuing from left to right in equal sections with small overlaps. Each original is also photographed in one exposure and is included in reduced form at the back of the book.

Photographs included in the original manuscript have been reproduced xerographically in this copy. Higher quality 6" x 9" black and white photographic prints are available for any photographs or illustrations appearing in this copy for an additional charge. Contact UMI directly to order.

UMI

A Bell & Howell Information Company
300 North Zeeb Road, Ann Arbor MI 48106-1346 USA
313/761-4700 800/521-0600

HARVARD UNIVERSITY

THE GRADUATE SCHOOL OF ARTS AND SCIENCES

THESIS ACCEPTANCE CERTIFICATE

The undersigned, appointed by the

Division of Engineering and Applied Sciences

Department

Committee

have examined a thesis entitled

"Atomic Scale Structure and Dynamics of Amorphous-Crystal Interfaces in Silicon: Simulations with Empirical and Quantum-Mechanical Approaches"

presented by Noam Bernstein

candidate for the degree of Doctor of Philosophy and hereby certify that it is worthy of acceptance.

Signature

Typed name Professor E. Kaxiras

Signature

Typed name Professor M. Aziz

Signature 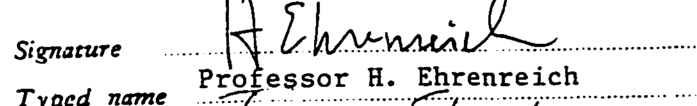

Typed name Professor H. Ehrenreich

Signature 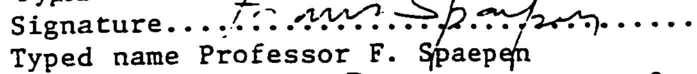

Typed name Professor F. Spaepen

Date June 2, 1998

Atomic scale structure and dynamics of amorphous-crystal interfaces in silicon: simulations with empirical and quantum-mechanical approaches

A thesis presented

by

Noam Bernstein

to

The Division of Engineering and Applied Sciences

in partial fulfillment of the requirements

for the degree of

Doctor of Philosophy

in the subject of

Applied Physics

Harvard University

Cambridge, Massachusetts

November 1998

UMI Number: 9910046

Copyright 1998 by
Bernstein, Noam

All rights reserved.

UMI Microform 9910046
Copyright 1999, by UMI Company. All rights reserved.

This microform edition is protected against unauthorized
copying under Title 17, United States Code.

UMI
300 North Zeeb Road
Ann Arbor, MI 48103

©1998 Noam Bernstein

All rights reserved

Abstract

We perform atomistic simulations to better understand solid phase epitaxy in silicon, the process by which the amorphous phase transforms into the diamond structure crystal phase at an amorphous-crystal interface. We begin by developing a quantum-mechanical nonorthogonal tight-binding (TB) model to describe the energetics of silicon atoms in bulk phases including the diamond and β-Sn structures, point defects, and activation energies. These structures are chosen to represent the range of geometries present in defective crystalline and amorphous silicon, including coordination from 4 to 6, point defects, and strained bond angles. We compare the results of this model Hamiltonian to other nonorthogonal TB models and to density functional theory calculations for several bulk crystal phases, relaxed and unrelaxed point defects, and surface energies. Using a combination of this TB model and the Stillinger-Weber empirical interatomic potential we simulate the melting and quenching of a silicon sample to create a system that is part crystal and part amorphous, with an interface between the two phases. We develop several localized measures of order to characterize the interface, and plot pictures of the atomic configurations at the interface to gain an understanding of its atomistic features. Using the environment dependent interatomic potential (EDIP), which is more reliable than the Stillinger-Weber potential, we create additional interface samples and simulate their annealing at various temperatures and pressures. We see thermally activated growth with Arrhenius behavior (log of growth rate is proportional to one over temperature) with an activation energy of 0.1 - 0.4 eV at low temperatures and 0.8 - 1.7 eV at high temperatures. In experiment only one activation energy of 2.7 eV is seen over a wide range of temperatures. We also observe an exponential dependence of the interface speed with pressure, corresponding to an activation volume for growth of about -0.7 ΩSi, compared with -0.28 Ω_{Si} in experiment.

For Karen and for my parents

Acknowledgements

First, I have to thank my parents without whom I'm unlikely to have become a scientist. I also have to thank Karen, both for her wonderful support keeping me sane and happy throughout grad school, and for her help in editing my various manuscripts. On the professional side I owe a lot to everyone I've worked with in grad school, but especially to Martin Bazant for his EDIP code, without which this thesis would be one chapter shorter and a lot less interesting. For my funding in the first couple of years in grad school I am indebted to the Division of Engineering and Applied Sciences and Dr. Kao who established a fellowship for graduate students. For the later years I received much appreciated support from NSF, through the Materials Research Science and Engineering Center at Harvard.

For my current choice of fields I owe a lot to Prof. Ehrenreich for pointing me in this direction, and Prof. Kaxiras who (besides being my thesis advisor) taught the first computational physics class I took. Through many parts of this project I also received a lot of help and grounding in experimental reality from Profs. Aziz and Spaepen, without whom this project probably wouldn't have even gotten started. And last, but certainly not least, Prof. Kaxiras, who was always a font of constructive suggestions and scientific insight and intuition, as well as support and motivation, that kept me churning along.

Citations to Previously Published Work

Chapters 3 and 4 are closely based on the following papers:

1. N. Bernstein and E. Kaxiras, in *Materials Theory, Simulations and Parallel Algorithms*, ed. by E. Kaxiras, J. Joannopoulos, P. Vashishta and R. Kalia, MRS Symposia Proceedings No. 408 (Materials Research Society, Pittsburgh, 1996).
2. N. Bernstein and E. Kaxiras, Phys. Rev. B **56**, 10488 (1997).
3. N. Bernstein, M. J. Aziz and E. Kaxiras, "The amorphous-crystal interface in silicon: a tight-binding simulation", to be published in Phys. Rev. B.
4. N. Bernstein, M. J. Aziz and E. Kaxiras, "Atomistic features of the amorphous-crystal interface in silicon", to be published in J. Comp. Aided Mat. Design.

Contents

Title Page . . . 1
Abstract . . . 3
Dedication . . . 4
Acknowledgements . . . 5
Citations to Previously Published Work . . . 6
Table of Contents . . . 7
List of Figures . . . 9
List of Tables . . . 12

1 Introduction **13**
1.1 Why Silicon? . . . 13
1.2 Structures of Covalent Materials . . . 14
1.3 Amorphous-Crystal Interfaces . . . 15
1.4 Experimental Studies of SPEG . . . 18
1.4.1 Methods . . . 18
1.4.2 Temperature Effects on SPEG Rate . . . 18
1.4.3 Pressure and Stress Effects on SPEG Rate . . . 20
1.5 Simulation of Amorphous-Crystal Interfaces and SPEG . . . 20
1.5.1 Hand Built Models . . . 20
1.5.2 Computer Generated Models . . . 21
1.6 Models for SPEG . . . 26
1.6.1 Bulk Defect Models . . . 26
1.6.2 Interface Defect Models . . . 28
1.7 Atomistic Computer Simulations Methods . . . 29

2 Simulation Algorithms **31**
2.1 Force Laws . . . 31
2.1.1 Quantum Mechanical Methods . . . 32
2.1.2 Density Functional Theory . . . 33
2.1.3 Tight Binding . . . 35
2.1.4 Empirical Potentials . . . 39
2.2 Simulation Algorithms . . . 40
2.2.1 Molecular Dynamics . . . 41

2.2.2 Energy Minimization 44
2.2.3 Low Energy Path Finding 45

3 Tight-Binding Hamiltonians for Silicon **47**
3.1 Introduction 47
3.2 Nonorthogonal Tight-Binding Models 49
3.2.1 Extended Hückel Theory Models 49
3.2.2 Density Functional Tight-Binding 51
3.3 Fitting Procedure 52
3.4 Tests 54
3.4.1 Bulk Structures 55
3.4.2 Point Defects 56
3.4.3 Surface Energies 62
3.5 Discussion and Conclusions 66

4 Amorphous-Crystal Interfaces **69**
4.1 Methods 70
4.2 Structural analysis 71
4.2.1 Bulk Properties 71
4.2.2 Localized Properties 75
4.3 Interface Energies 80
4.3.1 Defining "Crystalline" Atoms 81
4.3.2 Reference Bulk Amorphous Sample 82
4.3.3 Interfacial Energy Results 84
4.4 Summary 85

5 Solid Phase Epitaxial Growth **87**
5.1 Introduction 87
5.2 Methods 88
5.3 Annealing Results 90
5.3.1 Temperature Effects 92
5.3.2 Pressure Effects 97
5.3.3 Nonhydrostatic Stress Effects 98
5.4 Mechanism 100
5.5 Discussion 108

6 Summary and Conclusions **110**
6.1 Tight-Binding Models 111
6.2 Amorphous-Crystal Interfaces 113
6.3 Solid Phase Epitaxial Growth 115
6.4 Future Directions 117

Bibliography **119**

List of Figures

1.1 Cartoon of the epitaxial growth process at the amorphous-crystal interface in silicon. 17

2.1 Diagrams of the four possible interaction parameters for s and p orbitals in the two-center approximation. 38

3.1 Cohesive energy as a function of atomic volume curves for the diamond structure (DIA), β-Sn, body-centered-teragonal-5 (BCT5), and simple cubic (SC) lattices for four models (DFT/LDA, NO-TB, MS-TB, DF-TB). 57

3.2 Energy along the concerted-exchange diffusion pathway, without relaxation. 63

4.1 View of a sample along a [110] axis of the crystal. Atoms that were kept cool throughout the simulation (corresponding to the crystalline region) are in black, atoms in the region that was heated then cooled (corresponding to the amorphous region) are in white. Bonds are drawn between atoms closer than a distance of 2.7 Å. Periodic boundary conditions apply in all three directions. 72

4.2 Measures of order in the bulk of the crystalline and amorphous regions (as defined in the text): Pair distribution functions $g(r)$ (main panel) and bond angle distribution functions $p(\theta)$ (inset). 74

4.3 Local measures of order through the samples containing a crystal-amorphous interface, averaged over six samples. The ordinate is the z-coordinate of atoms along the [001] direction of the crystal, which is normal to the interface. (a) $\Delta\theta \equiv$ RMS deviation of the nearest neighbor bond angles from the ideal tetrahedral angle of 109.5°; (b) $|\vec{v_i}| \equiv$ Magnitude of the sum of the nearest neighbors vectors; (c) $\Omega_v \equiv$ Voronoi volume (volume of region closer to the atom than to any other atom). The letters 'a' and 'c' indicate the amorphous and crystalline regions of the samples, respectively. The vertical dashed lines correspond to the position of the interface. 77

4.4 Plan-view of an amorphous-crystal interface with the same conventions as in Fig. 4.1. One dimer defect in the crystalline region near the bottom center of the image and one near the left center are easily seen. 79

4.5 The crystalline portion of one interface sample, as defined in sec. 4.3.1. Panels (a) and (b) are views parallel to the interface, along the x and y axes, respectively. Panels (c) and (d) are views perpendicular to the interface from above and below, respectively. Black atoms were in the regions kept frozen through the simulation. Other atoms joined the crystal from the melt during the quenching process, with lighter colors indicating a larger distance from the boundary between the low and high temperature regions. 83

5.1 Pictures of a slice of an amorphous-crystal interface sample at several points during a constant temperature anneal. Sample temperature is 1000 K, and pictures at 1 ns intervals are shown. Crystalline atoms (as defined by the automated method described in sec. 5.3) are colored in black, amorphous atoms in white. 91

5.2 A scatterplot of two localized measures of order, the bond angle deviation around each atom $\Delta\theta$, panel (a), and the deviation of the bond angles from the known crystal bond directions χ, panel (b), plotted as a function of z, the position perpendicular to the interface. $\Delta\theta$ should be zero and χ should be four in the ideal crystal. 93

5.3 Number of crystal atoms vs. time for several constant temperature annealing runs. (a) is from samples created by a melt/quench simulation with some crystal atoms constrained. (b) is from a sample created by sandwiching bulk amorphous and crystal samples. Note that the axes on the two plots are different because of the different sample sizes. 94

5.4 Arrhenius fit for growth velocity as a function of temperature (linear least squares fit of $\log(v)$ vs. $1/T$). (a) an 800 atom sample created by quickly quenching a liquid adjacent to some constrained crystal atoms; (b) an 800 atom sample created by slowly quenching a liquid adjacent to some constrained crystal atoms; (c) a 2000 atom sample created by sandwiching bulk amorphous and crystal samples. Each sample is fit separately at low and high temperatures. Note that one outlier in (c) at 900 K, indicated by the arrow, has been excluded from the plot and the fit. 96

5.5 Arrhenius fit for growth velocity (left axis) as a function of pressure (linear least squares fit of $\log v$ vs. P). Concentration of five-fold coordinated atoms using a cutoff of 3 Å is also plotted (right axis). 2000 atom sample created by sandwiching amorphous and crystal bulk samples, annealed at 1000 K. Sample is fit separately at low and high pressures. 99

5.6 Arrhenius fit for growth as a function of different components of the nohydrostatic stress tensor (linear least squares fit of $\log v$ vs. σ). 2000 atom sample created by sandwiching amorphous and crystal bulk samples, annealed at 1000 K. 101

5.7 Energy along a crystallization path. Solid dots are relaxed configurations taken from time averaged snapshots, with atomic motion outside the active region frozen out. Line is a low energy path connecting these configurations, relaxing atoms along the path, but interpolating the unit cell size and shape. ΔE^f is the formation energy of the defect and ΔE^m is the migration energy. ΔN_c is the change in number of crystal atoms, and ΔE_{ac} is the energy of crystallization per atom for the amorphous phase. 104
5.8 Five relaxed atomic configurations along a crystallization path. For clarity, only atoms in a thin slice parallel to the interface are shown. Atoms of type (c) are crystalline, and the others are amorphous atoms with three-fold, four-fold, or five-fold coordination. In configuration 1, a quenched in coordination defect is present. Two coordination defects nucleate in config. 2, and hop around in configs. 3 and 4. In config. 5, the two new coordination defects have annihilated each other, and only the original quenched in defect remains. 105
5.9 Volume and unit cell shape variation along a crystallization path. Note that the unit cell size and shape were only relaxed at the solid points, and the connecting lines are simply interpolations, unlike the energy in Fig. 5.7. . . 107

List of Tables

3.1 Parameters for the NO-TB and MS-TB Hamiltonians: ϵ_s and ϵ_p are the on-site energies for the s and p orbitals, respectively. $V_{\lambda\lambda'\mu}$ are the symmetry allowed interactions between orbitals on different atoms at $r = d_0$, and α is the exponential decay rate of the interaction with distance (Eq. 3.3). K_0 and C_0 are the value of $K(r)$ at $d_{\min}$ and its curvature (Eq. 3.6). χ_0 is the magnitude of the pairwise repulsion at $r = d_0$ (Eq. 3.10). 54

3.2 Bulk properties for various lattice structures computed by DFT/LDA and three TB models. The DFT/LDA cohesive energies were uniformly shifted to agree with experimental results for the equilibrium energy. 58

3.3 Elastic constants of the diamond lattice structure. c_{44}^* is the value of the elastic constant without including the relaxation of the atomic basis. . . . 58

3.4 Band structure features for diamond structure silicon. The DFT/LDA results include a 0.6 eV scissor-operator shift of the conduction levels [1, 2]. . 58

3.5 Formation energies for ideal point defects E_f^{id} and relaxation energies $\Delta E_f = E_f^{\text{relaxed}} - E_f^{\text{id}}$. 60

3.6 Surface energies for the Si (100) and (111) surfaces. γ is the surface energy in eV per (1×1) cell; $\Delta\gamma$ is the relaxation energy relative to ideal (1×1) γ; θ is the tilt angle of dimers; d is the bond length of the dimer. 65

4.1 Coordination and ring statistics averaged over six samples. Coordination statistics are tabulated separately for the crystalline and amorphous regions. Note that the rings are too large compared to the thickness of the crystalline region to allow for such a separation, so values averaged over the entire sample are listed. 75

5.1 Activation volume scalar part ΔV^* and diagonal tensor elements $\Delta V_{\alpha\alpha}^*$ from Arrhenius fits of growth rate vs. applied stress tensor components. Simulation measurements were made on a sample created by sandwiching bulk and amorphous samples, annealed at 1000 K. Note that the experimental measurements are not self-consistent. 100

Chapter 1

Introduction

1.1 Why Silicon?

Covalent semiconducting materials, and especially silicon, are the foundation of a vast range of modern technologies. In most of these applications these materials are used to make integrated circuits (ICs), the core of computers used both as general purpose computation machines (from personal computers to massively parallel supercomputers) to specialized controllers embedded in machines that in the past were purely electro-mechanical, like automobile engines or rice-cookers. ICs are typically made to be as small as possible, since the smaller the circuit the faster the electrons can get from one component to the next, and the faster the computer runs. Production cost is also reduced if more devices can be made from each silicon wafer, making it important to make larger and larger wafers. These types of devices are dependent on our ability to make large single crystal silicon wafers with virtually no defects to impede the motion of the electrons within the circuits. However, not all silicon devices are made from single crystal. Devices that need to be physically large, like solar cells that need to collect as much light as possible or thin film displays that need to display large images, can only be mass produced from polycrystalline or amorphous silicon. None of these applications, either using single crystal, polycrystalline or amorphous silicon, would be possible without the ability to precisely tailor the electrical

properties of the silicon on very small scales to make electronic components. These components can then be combined in elaborate networks that collectively do computation, or arranged to harvest solar energy and convert it into electrical energy, or control the color or opacity of pixels in a display. The economic importance of this wide range of applications has driven the scientific investigation of silicon, making it one of the most thoroughly studied materials in history. The relative ease of obtaining exceptionally pure and defect free samples has made it a favorite prototype for the study of all covalently bonded solids.

1.2 Structures of Covalent Materials

Chemical interatomic interactions in solids can be broadly classified into three types: metallic, ionic, and covalent. Atoms that do not interact chemically, such as noble gasses, experience a fourth type of interaction, van der Waals bonding, that is very weak and rarely relevant in solid state systems. Metallic bonding has very little angular preference and maximizes the cohesive energy gain by increasing the number of neighbors, leading to close packed structures like face centered cubic or hexagonal close packed. Ionic bonding is dominated by the desire to bring oppositely charged species near each other while avoiding bringing similarly charged species together. This leads to moderately dense packings but with lower coordination than close packed systems, for example the rock salt structure. The distinguishing microscopic feature of covalent materials is a small number (2-4) of bonds with well specified preferred angles. This typically leads to low energy open network structures like diamond structure for silicon and germanium, and graphite for carbon.

Silicon atoms have 14 electrons, 10 in the core and 4 available for chemical bonding. In isolated atoms two valence electrons are in s states and two and in p states. In forming a solid, these electrons prefer to enter four sp^3 hybrids and form four covalent bonds oriented from the center of a tetrahedron to its 4 corners. These bonds are quite stiff longitudinally, and rigid with respect to variations from the ideal tetrahedral angle

of 109.5°. This makes the diamond structure, where each atom has four neighbors at the ideal tetrahedral angle, the ground state structure for silicon [3]. When many silicon atoms are brought together without the time or the kinetic energy to explore configuration space and find the ground state structure, they can instead fall into a metastable amorphous structure. This can happen through low temperature deposition, in which the atoms lack the kinetic energy to move very far from where they land. It can also happen during ion beam implantation, when the energetic ion and the atoms from which it ricochets disturb the lattice, but the kinetic energy is dissipated too quickly to allow the damage to deal. Last, it can happen during rapid quenching of the liquid, where the kinetic energy is removed too quickly to allow the disordered and six-fold coordinated liquid to find a path in configuration space to an ordered and four-fold coordinated crystal. The amorphous structures produced in these ways are are believed to be well modeled by a continuous random network. Each atom has four bonds, with nearly ideal lengths and small but non-negligible deviations in the bond angles. These deviations add up quickly, and further and further neighbors of a given atom quickly lose any correlation with its position or orientation. When only looking at one atom and its first neighbors, the resulting network looks very much like the ground state diamond structure, but lacks translational or rotational symmetry at longer distances. In practice amorphous silicon is not a perfect continuous random network, since it has over-coordination and under-coordination defects, but the main features remain.

1.3 Amorphous-Crystal Interfaces

All of the techniques used to make amorphous silicon can lead to the formation of an amorphous-crystal (a-c) interface between it and an underlying crystal lattice. Of particular technological importance is ion implantation, where dopants are implanted into a thin layer at one surface of the substrate, making it electrically active. At low temperatures, high doses (high density of implanted atoms), or high dose rates this can cause

the formation of an amorphous layer which must be converted back into crystal for the device to be functional. The other common methods of producing amorphous silicon, low temperature deposition and pulsed laser melting, also produce such an interphase interface between the newly formed amorphous layer and the crystalline silicon substrate.

When heated up above a few hundred degrees Celsius the mobility of the atoms in the amorphous phase increases enough that they can hop around and transform into the lower energy diamond structure crystal phase. The crystal grows epitaxially, with the newly crystalline atoms continuing the existing lattice, directly from the solid amorphous phase to the solid crystal phase. The process by which the interface moves as the amorphous atoms rearrange themselves to move into crystalline positions, first observed in the late 1960s [4], is called solid phase epitaxial growth or SPEG (Fig. 1.1). The lcg of the growth rate is proportional to minus one over temperature, suggesting a thermally activated process in which the atoms must wait for a fluctuation in local energy to hop over some sort of barrier.

The growth process is quite interesting from several points of view. It occurs entirely at the existing interface, without the nucleation of any new crystal grains in the middle of the amorphous phase. It produces an extremely high quality crystal, suitable for use in ICs, growing without defects from the highly disordered (and compared to the crystal highly defective) amorphous phase. It is therefore vital for the healing of dopant implantation damage in device fabrication. From a more fundamental point of view, the fact that it is thermally activated with a single activation energy over several hundred degrees and ten orders of magnitude in a-c interface speed is quite intriguing [5]. It strongly implies there is one rate limiting step with a well defined energy, or a very small range of energies. A less likely possibility is that there are several mechanisms operating in parallel with very similar activation energies.

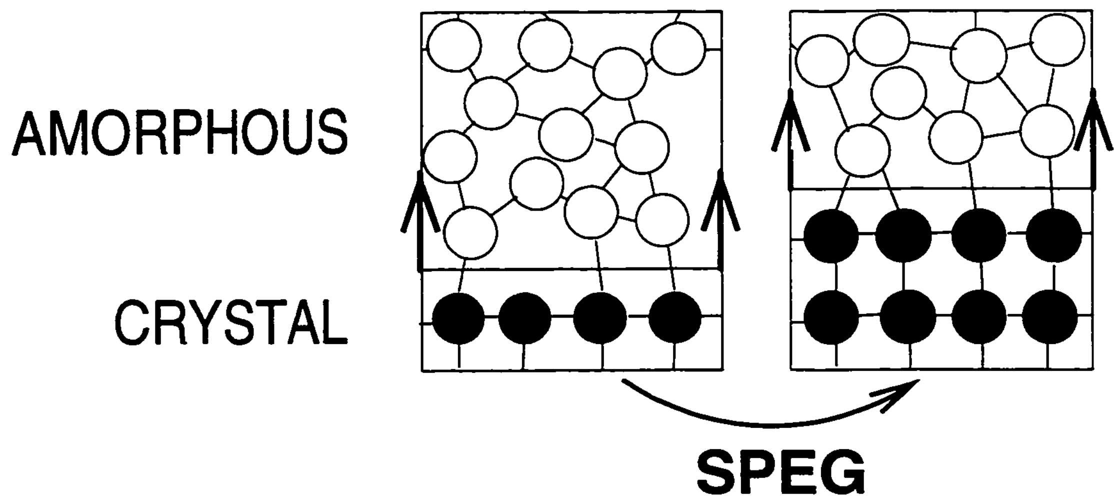

Figure 1.1: Cartoon of the epitaxial growth process at the amorphous-crystal interface in silicon.

1.4 Experimental Studies of SPEG

1.4.1 Methods

Many aspects of solid phase epitaxy have been subject of intense study. Although other characterization methods were used in the past (see references in Olson and Roth's review [5]), the modern technique of choice for measuring SPEG rates is called time resolved reflectivity, or TRR [6]. In this technique a red HeNe laser, which can penetrate to a substantial depth in amorphous silicon (an infrared laser is used for amorphous germanium), is reflected by the abrupt changes in index of refraction at the sample-air interface and at the *a*-c interface. The two coherently reflected beams interfere constructively or destructively depending on the distance between the free surface and the *a*-c interface. The resulting intensity goes through a complete cycle when the interface has moved a distance equal to half a wavelength of the laser (in the amorphous silicon) with respect to the sample surface if the beam is incident perpendicular to the surface. This technique is quite versatile, and can be performed *in-situ* throughout an experiment so long as the sample is not surrounded by an opaque material. It can therefore be done while the sample is inside a furnace with a window, or while the sample is under applied pressure in a diamond anvil cell with the laser transmitted through the diamonds. Using TRR the position of the *a*-c interface can be measured as a function of time, and the interface velocity can be easily calculated. Using a range of techniques the interface velocity has been measured as a function of a number of parameters, including thermodynamic quantities like temperature [7, 8, 5], pressure [9], and non-hydrostatic stress [10, 11, 12], as well as other characteristics of the sample such as impurity concentration, both for electrically active dopants [5] and other commonly present elements such as hydrogen [13, 14].

1.4.2 Temperature Effects on SPEG Rate

The first parameter affecting SPEG rate to be studied was temperature. According to the theory of thermally activated processes the growth rate is expected to be

described by the equation

$$v(T) = A\lambda\nu \exp\left(-\frac{\Delta G^*}{kT}\right)\left[1 - \exp\left(\frac{\Delta G^0}{kT}\right)\right]. \tag{1.1}$$

A is a geometrical factor, λ is the distance the interface moves with each atomic rearrangement, and ν is an effective frequency at which the mechanism is attempted. ΔG^* is the excess free energy of the activated state and ΔG^0 is the free energy change per rearrangement. For SPEG ΔG^0 is sufficiently large and negative that for any reasonable dependence of ΔG^0 on temperature and pressure the second factor varies by less than a factor of two over the entire experimental parameter range. It can therefore be reasonably approximated as constant compared to the first factor that varies by ten orders of magnitude. This simplifies the expression for the interface speed to

$$v(T) = A\lambda\nu \exp\left(-\frac{\Delta G^*}{kT}\right). \tag{1.2}$$

$\Delta G^* = \Delta E^* - T\Delta S^* + P\Delta V^*$ includes contributions from the internal energy, entropy, and volume of the activated state. Each of these terms has a straightforward physical interpretation: the activation internal energy is the height of the potential energy barrier; the activation entropy is the amount by which the configurational or vibrational freedom of the system is increased at the activation barrier; the activation volume (or, for non-hydrostatic stress, the activation strain ΔV) is the shape of the activated state. This form for the variation of the interface speed with temperature is called Arrhenius behavior. It is easy to see that the speed will vary exponentially with inverse temperature, with the slope of a $\log(v)$ vs. $1/T$ plot at zero applied pressure giving the activation energy ΔE^*.

Plots of the log of the interface speed as a function of inverse temperature, as shown in a number of articles including the review by Olson and Roth [5], show excellent agreement with this expression. All data points lie along one line covering ten orders of magnitude in interface speed, with a slope corresponding to an activation energy ΔE^* of 2.7 ± 0.05 eV. As noted by Lu *et al.* [9], the growth rate is independent of the history of the sample, indicating that the rate determining structure or process is a stable feature of

the system.

1.4.3 Pressure and Stress Effects on SPEG Rate

The expected variation of interface velocity with applied pressure can also be easily seen from Eq. 1.2. A plot of $-kT \log v$ as a function of applied pressure should be linear, with the slope indicating the activation volume ΔV^*. A summary of available data is plotted by Lu *et al.* [9]. The range of pressures only spans two orders of magnitude in interface speed, and the error bars both in the applied pressure and resulting speed are larger than in the speed vs. temperature plots, but the Arrhenius behavior is clear. The rate increases with applied pressure, with an activation volume $\Delta V^* = -0.28 \pm 0.03\ \Omega_{Si}$, where $\Omega_{Si} = 20.0$ Å^3 is the volume per atom of silicon in the diamond structure. When the applied stress is not hydrostatic (i.e. can not be described by a scalar pressure), the $P\Delta V^*$ term in the activation free energy is replaced with a $-\sigma\Delta V^*$. Measuring the interface speed as different elements of the applied stress are varied, for example σ_{xx} or σ_{yy} for in-plane compression or tension or σ_{zz} for out of plane compression or tension, indicates the magnitude of the corresponding element of ΔV^*. This is much harder to do in a quantitative manner, but the results of Aziz *et al.* [10, 11, 12] indicate that V_{xx} and V_{yy} are positive, while V_{zz} is negative. Therefore, applying compressive stress in the interface plane increases the SPEG rate, but applying compressive stress perpendicular to the interface slows down the crystallization rate.

1.5 Simulation of Amorphous-Crystal Interfaces and SPEG

1.5.1 Hand Built Models

The first study of the *a*-c interface in silicon was the work of Spaepen [15, 16]. He built a ball and stick model of amorphous silicon on top of a (111) surface using *ad-hoc* construction rules favoring five and seven-fold rings to make a continuous random network that merged into the existing crystal. By measuring the position of each vertex

in the model he calculated some structural properties of the system, including the pair correlation function and bond angle distributions at different distances from the interface. He also used a Keating potential [17] to relax the atomic positions and to evaluate the interfacial tension σ_{ac}, the excess energy needed to form the interface between the two phases. Using a similar hand built structure as a starting point, Spaepen and Turnbull suggested a mechanism [18] beginning with the formation of a pair of dangling bonds at a step in the interface, which then hop through the network, in the process crystallizing several atoms before being annihilated. However, they did not evaluate the energetic cost of this mechanism.

Soon after Saito and Ohdomari [19] followed a similar hand-building procedure to produce an (001) interface. They also measured the bond angle distribution (and corresponding Keating potential energy) as a function of distance from the interface, although they did not calculate the corresponding interfacial tension. Using a dangling bond mechanism similar to that suggested by Spaepen and Turnbull, Saito and Ohdomari found a path that resulted in the crystallization of several atoms at the interface [20]. At each step along the path they relaxed the atomic positions using the Keating potential, and computed the energy. This gave an estimate of the activation energy $\Delta E^* = 1.8$ eV for that path, neglecting the energy of the transition state between the metastable configurations, which they estimate to be between 1.0 and 2.8 eV.

1.5.2 Computer Generated Models

Simulations of the A-C Interface

Several approaches have been used to create *a*-c silicon interfaces with computer simulations. Wooten and Weaire [21] used a geometrically motivated algorithm originally used by Wooten *et al.* [22] to make bulk amorphous silicon samples. A particular localized bond switching move is used to disorder an initially perfect crystal. This rearrangement preserves the four-fold coordination of each atom, but changes the connectivity of the

lattice and introduces five and seven-fold rings. Each move is accepted or rejected with a standard Metropolis Monte Carlo scheme [23], starting at a high temperature to "melt" the sample, and then reducing the temperature to quench in the disorder. By applying the moves to only part of a bulk sample, an interface between the amorphous and crystal silicon is formed. The only characterization of the interface structure discussed by Wooten and Weaire is the decay of the structure factor with respect to position perpendicular to the interface. They see a change from the crystal value of 1.0 to the amorphous value of 0.0 over less than 3 Å. They also observe crystallization over 10^6 steps when the Monte Carlo procedure is carried out on an interface sample at half the melting point of the crystal. However, since their rearrangement procedure does not necessarily correspond to the physical motion of the atoms, the details of the crystallization process are not meaningful.

Erkoç *et al.* [24] used an empirical potential molecular dynamics (MD) simulation to create an *a*-c interface by simulating a melting and quenching process. Starting with a silicon slab with a free surface, they melted a layer on one side by heating it up above the melting point $T_m = 1950$ K with their potential, while keeping several layers of crystal atoms rigidly fixed to their perfect lattice positions. They then quenched the sample by rescaling the particle velocities to reduce the temperature by 1 K every 500 MD time steps. Using this method they created several thicknesses of samples with (001) interfaces and one (111) interface. To characterize the films Erkoç *et al.* plot the density of the sample averaged along slabs parallel to the interface. Their main observation is a low density layer in the amorphous adjacent to the crystal, followed by a high density layer. This effect is particularly striking in the (111) interface sample. Erkoç *et al.* attribute this to the high surface atom density in this orientation, higher than the density of atoms per unit area the amorphous structure can achieve.

In their study of the effects of the incident atom energy on the Si deposit morphology in MBE simulations Gilmer and Roland [25] included a range of temperatures

and energies that formed an amorphous film. Depositing onto both (001) and (111) interfaces with 0.17 eV and 5.0 eV atoms onto substrates between 0 K and 1000 K, Gilmer and Roland created films with a range of morphologies. At low temperatures the films were amorphous, and at high temperatures crystalline. To distinguish the two phases the authors used a criterion proposed by Grabow *et al.* [26] based on the coordinations of the atoms. The transition temperature depended on the orientation of the surface and on the incident atom energy. Films deposited onto the (111) surface tended to form stacking faults (a defect with zero energy in the Stillinger-Weber potential they used), and nucleate amorphous regions at the partial dislocations bounding the stacking faulted regions. The transition from crystal to amorphous deposit occured at about 400 K for the high energy incident atoms and at about 800 K for the low energy incident atoms. In contrast films deposited onto the (001) surface, where the geometry does not allow for the formation of low energy defects like stacking faults, grew as crystals at lower temperatures than on the (111) surface. The defects responsible for the nucleation of the amorphous phase on this surface are dimers from the (2×1) reconstruction on the (001) surface that sometimes remain unbroken. The transitions in this geometry occured at about 200 K for the high energy incident atoms and at about 500 K for the low energy incident atoms. The high energy incident atoms aid the crystallization process by giving substantially more kinetic energy to the substrate atoms, enhancing their mobility. Nevertheless the impinging atom does not diffuse very far from the point of impact, usually less than 2 to 3 Å. This is why despite the very rapid deposition rate in the simulation (10^{10} layers/s as compared with 1 layer/s in experiment) the growth is crystalline, since the atoms do not need the time to diffuse very far. Except for their observation of what defects typically cause amorphous growth to nucleate, Gilmer and Roland do not further characterize the details of the interface.

Simulations of SPEG

Caturla *et al.* studied the evolution of a planar (001) *a*-c silicon interface [27] under ion beam irradiation. Using an MD simulation with the Stillinger-Weber interatomic potential [28] the authors simulated the melting of about half of a silicon slab with periodic boundary conditions parallel to the surface. The liquid was then quenched with a quasidynamic algorithm, where all atoms that are moving antiparallel to the calculated forces (i.e. atoms moving up the potential gradient) are stopped at each time step. The resulting amorphous sample is quite defective, with an average coordination of 4.3, and many atoms at intermediate distances between the first and second neighbor peaks in the pair correlation function. The authors state that this structure is consistent with a rapid quench of the liquid as would occur in the amorphous zone resulting from 5 keV Si recoils. With this amorphous sample Caturla *et al.* simulate the effect of ion implantation by assuming that one atom in the crystal recoils off each incoming ion, rather than simulating the details of the ion-crystal interactions.

Caturla *et al.* subject the samples to a sequence of up to 400 recoils at two energies, 15 and 20 eV, from either the amorphous or crystal side of the interface. In all cases the recoil atoms are within two atomic planes of the *a*-c interface, and are initially moving towards it. If the 20 eV recoils are started at the amorphous side of the interface, the sample crystallizes. After 300 recoils almost all of the amorphous portion is gone, as seen in a side view of the sample. This rate corresponds to about 0.67 atoms crystallized per recoil event. If the recoils are started on the crystal side of the *a*-c interface the sample is disordered and defects accumulate in the crystal, although it is not amorphized. The increase in potential energy per recoil in this case is about 10 times smaller than the reduction in energy for the recoils generated on the amorphous side of the interface. Therefore the authors expect a net reduction in the energy if the recoils were simultaneously being generated on both sides of the interface. The sample also crystallizes when 15 eV recoils are generated at the amorphous side of the interface, at about the same rate as for

the 20 eV recoils. When generated on the crystal side of the interface however, no lasting damage is produced, and the sample neither crystallizes nor amorphizes.

Marqués *et al.* studied the evolution of small spherical crystallites in an amorphous matrix [29] using the Stillinger-Weber interatomic potential [28]. They generated bulk amorphous samples and replaced small spherical regions with crystal. To distinguish crystal and amorphous atoms, they monitored the bond angle deviation around each atom averaged over 1 ps. Although the instantaneous deviation for both types of atoms was comparable, the average distribution was much smaller for the crystal atoms where the bonds were mainly being distorted by thermal fluctuation. In the amorphous phase where the distortions are quenched into the network the average deviation remains large.

First Marqués *et al.* anneal the samples above the amorphous melting point using MD. Under these conditions crystallization of a few atoms releases enough energy to melt a nearby region in the amorphous phase. They study the rate of crystallization at different temperatures and see a good fit to a model for the crystallization from the melt originally presented by Grabow *et al.* [26]. The activation energy value for the best fit is substantially higher than the activation energy for diffusion in the melt, in contrast to the earlier work by Grabow *et al.* for planar interfaces. Marqués *et al.* state that the additional barrier is caused by the spherical interface geometry reducing the number of bonds available for crystallization to occur. However, they do not explain why the curved geometry should not be bounded by the (001) and (111) interface results calculated by Grabow *et al.*, or why the difference should manifest itself as a higher activation energy, rather than as a lower prefactor for the exponential dependence of the interface speed on temperature.

Using the same samples in a situation more relevant to solid-phase epitaxy, Marqués *et al.* also simulate the evolution of the system below the amorphous melting point under ion beam irradiation. At the beginning of each stage of the simulation they set up 20 recoils in the amorphous phase around the crystallite, all moving towards the crystallite with a kinetic energy that is below the threshold for forming defects in the crys-

tal. They allowed the system to evolve and reach thermal equilibrium, and then repeated the process. They performed this simulation at 773 K, and observed a steady growth as long as the irradiation continued. In contrast, samples that were not irradiated show no measurable growth at this temperature after a transient relaxation. Marqués *et al.* describe the crystallization process as a collective motion of the atoms. The recoil produces large displacements in the atoms near the interface. Several of these atoms move around and fall into energy minima corresponding to additional crystal lattice positions. The authors were not able to discern a more specific mechanism, or determine whether any specific defect types, such as dangling bonds or vacancies, contribute to the mobility of the amorphous atoms.

1.6 Models for SPEG

A number of models for the crystallization mechanism in solid phase epitaxy have been proposed in the literature [7, 18, 30, 31, 32, 33, 34]. In all cases the crystallization is assumed to be defect mediated, since the atoms in the rigid network would not be sufficiently mobile otherwise. Some models [7, 31, 32, 33, 34] assign the rate limiting step to the formation and diffusion of some defect species from the bulk region of either phase to the interface. Others [18, 30] suggest that the rate limiting step is some localized reaction at the interface. Many of these models were reviewed and analyzed by Lu *et al.* in Ref. [9].

1.6.1 Bulk Defect Models

Csepregi *et al.* [7] suggest a mechanism limited by the rate of generation of vacancies in the crystal. They note that the formation energy of a vacancy in crystalline silicon is quite close to the activation energy for SPEG, and that the migration energy of the vacancy is small compared to the formation energy. In their analysis, Lu *et al.* note that applied pressure will reduce the migration free energy of the vacancy, and that if the pressure is high enough the free energy will become negative. This would allow the

vacancies to migrate without a barrier, and will most likely lead to a dramatic change in the system, one which is not observed up to 5.0 GPa. This leads to an upper limit on the formation volume of the vacancy of less than +0.44 Ω_{Si}, lower than any calculation for this quantity known at the time. More recent results by Tang *et al.* [35] using an orthogonal TB model indicate a formation volume for the vacancy of only +0.03 Ω_{Si}, indicating that perhaps the vacany mechanism is at least consistent with the lack of any pathology in the pressure effects. Since the formation volume of the vacancy is almost certainly positive, to explain the overall enhancement of SPEG rate with pressure the migration of the vacancy would have to be strongly enhanced by pressure. It is currently unknown if this is the case.

Lu *et al.* also calculate the number of atoms that must be crystallized by each vacancy. The concentration and mobility of the defects are estimated from the self-diffusion coefficient in silicon (approximated by the Ge tracer diffusivity for diffusion in amorphous silicon). This analysis shows that each vacancy (or any defect in the bulk crystal) would have to crystallize more than 3×10^8 atoms, which is unlikely because the defect densities in the amorphous phase (and therefore at the interface) are greater than 1 in 10^4 atoms and these defects would probably interrupt the crystallization. A similar analysis indicates the formation and diffusion of defects in the bulk amorphous phase, including dangling bonds [31], floating bonds [36], or other defects [33, 34], is still plausible as the rate limiting step for SPEG according to this analysis. For the vacancy or interstitial like mechanisms the number of atoms crystallized would have to be greater than 7, and greater than 2 for the dangling or floating bond mechanisms. The motion of the vacancy or interstitial like defects contributes fully to the bulk diffusivity, while each dangling/floating bond would contribute about $\frac{1}{3}$ as much mass transport to the diffusivity. Therefore there would have to be more of the dangling/floating bond defects to explain the measured diffusivity, and so each one would have to crystallize fewer atoms to account for the observed interface speed.

Lu *et al.* rule out the relevance to SPEG of any defects in the bulk amorphous

phase for two reasons. The first is that there is a strong relaxation effect on the diffusivity of amorphous silicon: a low temperature pre-anneal significantly reduces the measured diffusivity of Ge in Si [37] and Au in Si [38]. However, the relaxation effect on SPEG rates is much smaller, so diffusion of defects from the bulk amorphous can not be responsible for a large part of the crystallization. The second reason is that non-hydrostatic stress significantly changes measured SPEG rates, despite the fact in the amorphous phase the stress is almost fully relaxed [39, 40] by plastic flow. Mechanisms where the rate limiting step occurs in either bulk phases are also inconsistent with the effect of interface orientation on the growth rate. The interface speed is observed to be approximately proportional to $\sin(\theta)$, where θ is the angle away from the (111) plane [41]. Since diffusion in both phases is approximately isotropic, bulk mechanisms can not explain the factor of twenty in observed interface speeds between growth on the (001) and (111) interfaces.

1.6.2 Interface Defect Models

The second type of crystallization mechanism proposed to explain SPEG is the action of a defect at the interface. Specifically suggesting dangling bonds as the relevant defect, Spaepen and Turnbull [18] first suggested this mechanism for solid phase epitaxy. Williams and Elliman [30] suggested a very similar mechanism based on charged kink sites at the interface to explain the effects of doping on interface speed. Lu *et al.* analyzed both of these models in great detail in Ref. [9], and I will briefly summarize that analysis here. The dangling bonds (or kink sites) are thermally generated as predicted by transition state theory, hop some number of times in a thermally activated manner, and are finally annihilated or trapped. They note that for the expressions to result in an Arrhenius form for the crystallization rates with an activation energy $\Delta G^* = \Delta G_f + \Delta G_m$, the sum of a formation and migration parts, the defects must be annihilated with unimolecular kinetics. They must either be trapped at a number of sites that does not vary with temperature, or annihilate with other thermally created defects so long as the defects are created in pairs

(as expected for dangling bonds or kinks along a straight step) and move sufficiently little so as to always annihilate with each other. Bimolecular annihilation kinetics, if the defects have time to diffuse throughout the system and annihilate with each other, would result in an activation energy $\Delta G^* = \frac{1}{2}\Delta G_f + \Delta G_m$. The prefactors from a fit of the model to the experimental data are consistent with the very rough estimates available for the formation and migration entropy parts of the free energy, bounded between zero and the entropy of fusion. If these entropies are small the number of atoms that each defect must crystallize rises to about 200 atoms. This is still a more plausible number than 10^8 atoms estimated for a bulk crystal defect mechanism, the only other type that is consistent with the observed nonhydrostatic stress effect. Because of the density and structure of steps on the interface where dangling bonds or kinks can be generated the interface defect models are also consistent with the orientation dependence of growth.

The formation energy for these defects can be estimated as half the cohesive energy of the system, i.e. $\Delta E_f = 2.246$ eV. The rest of the activation energy of 2.7 eV is the migration term $\Delta E_m = 0.43$ eV, in reasonable agreement with the activation energy for ion-beam assisted SPEG where the defects are assumed to be created athermally by the bombarding ions. The negative activation volumes also seem plausible. The defects are very localized, and their formation volume should be positive but small, at most half the formation volume of a vacancy for a dangling bond pair. The migration volume is likely to be strongly negative as the unpaired electron reaches across a ring to attack another bond. Thus the dangling bond model agrees with all of the calculations available to Lu *et al.* at the time.

1.7 Atomistic Computer Simulations Methods

Despite the wealth of experimental work, the mechanism for SPEG is still unclear [7, 31, 33, 34, 18, 30, 9]. Continuous refinement of both sample preparation procedure and measurement techniques have helped measure many macroscopic properties of

the growth process. These include the activation energy, volume, and strain, as well as the effects of other species in the sample. Microscopic information, on the other hand, is nearly impossible to obtain. The interface, where the growth is occuring, is buried within the sample. The most direct experimental atomic resolution probes, scanning probe microscopes such as scanning tunneling microscopes (STM) and atomic force microscopes (AFM), can only be used at an exposed surface. Other tools, such as high-resolution transmission electron microscopy (HRTEM), can only be used on very thin sections, and are hard to use for atomic resolution on amorphous materials where large, periodic structures to diffract the electrons are non-existent. Without such microscopic information it is hard to distinguish among the mechanisms suggested in the literature. Quantitative information about the prediction of the various models could perhaps be used to settle the issue, but only qualitative or semi-quantitative estimates of important numbers such as the activation energy or mobility of specific defects have been available so far. Unfortunately, several of the models proposed in the literature are quite similar within the resolution of these estimates. Atomistic simulations offer the possibility of seeing the entire process with perfect atomic resolution, although with some inevitable compromises. The size and time scales accessible, even with the fastest methods and most powerful computers, are still many orders of magnitude below the experimental work. The methods used to simulate the atomic motion are all approximate, with the fastest methods using the crudest and least accurate approximations.

Chapter 2

Simulation Algorithms

2.1 Force Laws

The underlying physics in virtually all computer simulations of solid state systems comes from the energy and force laws used. These are the equations used to calculate the energy of the system for a given configuration of the atoms. Derivatives of this energy function with respect to atomic positions give the forces on the atoms, and derivatives with respect to uniform deformation of the entire sample give the stresses on the sample. These energies and forces can be applied in a variety of different algorithms. They can be used to calculate the forces in Newton's equations of motion, which can then be integrated with respect to time to give the atomic configuration at any later time given an atomic configuration at the beginning of the simulation. They can also be used with various algorithms to minimize the energy of the system with respect to atomic positions and to find a local or global energy minimum corresponding to a metastable or globally stable configuration, respectively. Given several metastable configurations, a saddle-point finding algorithm can be used to find low energy pathways between these configurations.

2.1.1 Quantum Mechanical Methods

In its full form, quantum mechanics, the theory which describes the interactions of all things, can be reduced to one equation, the Schrödinger equation:

$$\mathbf{H}\Psi = -i\hbar\frac{d\Psi}{dt} \tag{2.1}$$

where $\mathbf{H}$ is the Hamiltonian operator whose expectation value is the total energy of the system, and Ψ, a complex valued function of all the particle coordinates, is the wavefunction for the system. Several approximations are typically made to apply quantum mechanics to solid state systems. In systems made of atoms where the nuclei are much heavier than the electrons, the quantum mechanical nature of the nuclei is neglected, leaving only the electrons in the quantum mechanical problem. The nuclei are then treated as a collection of classical particles interacting through the Coulomb repulsion and through an effective potential exerted by the electrons. If the energies in the system are lower than the typical electronic excitation energy (as is the case for the vast majority of solid state simulations. with some exceptions such as interactions with high intensity laser pulses), the Born-Oppenheimer approximation [42] is used: since they are so much lighter and move much more quickly than the nuclei, the electrons are assumed to always be in their ground state, determined by the potential that the nuclei provide and the interactions between the electrons. With these approximations the Schrödinger equation is reduced to its time independent form,

$$\mathbf{H}\Psi' = E\Psi' \tag{2.2}$$

an eigenvalue equation for the all electron wavefunction Ψ', a complex valued function of all the electronic coordinates. This equation must be solved for each atomic configuration, and the electronic energy E added to the classical Coulomb repulsion for the nuclei to compute the system's total energy. However, this is nearly impossible for more than a few electrons. The wavefunction Ψ depends on all the electronic coordinates in a non-separable way, and no practical method to compute it is known. Therefore, a series of approximations

are used to make the problem tractable.

2.1.2 Density Functional Theory

The most accurate method for computing atomic energies and forces routinely used for solid state simulations is density functional theory (DFT), usually within the local density approximation (LDA). DFT, originally developed by Kohn and Sham [43, 44], is based on a theorem that states that the ground state total energy of a quantum mechanical system is a functional of the density of the particles in the system at each point in space

$$E = F[n(\boldsymbol{r})] \tag{2.3}$$

rather than of the many particle wavefunction

$$E = F[\Psi(\boldsymbol{r}_1, \boldsymbol{r}_2 \ldots \boldsymbol{r}_n)] \tag{2.4}$$

as might be expected from the Schrödinger equation. This reduces the problem from finding a function of all the particle positions (the wavefunction of all the electrons) to a function of one position (the total electron density at each point in space). However, the theorem does not state what the density functional is, merely that it exists. The breakthrough development that made DFT a useful computational tool was the re-introduction of wavefunctions. The total electronic density can be written as a sum of single particle densities, each of which is the magnitude of a wavefunction of one particle. Taking functional derivatives of Eq. 2.3 with respect to the single particle wavefunctions gives an eigenvalue equation, where each particle is coupled to the others via a potential applied by the total density. To solve this equation, one guesses a total density at each point in space. Using this density to generate a potential, the eigenvalue equation is solved, and the resulting single particle wavefunctions are used to generate a new density, and the process is repeated to convergence.

Unfortunately, even with this formulation of DFT, the Hamiltonian used in the single-particle eigenvalue equation is not known. It can be separated into several parts, in-

cluding a single particle kinetic energy, the potential applied by the nuclei, an inter-electron Coulomb repulsion, and the remaining electronic interaction part called the exchange-correlation functional. No exact form is known for the last part, but several approximations are used, the most common of which for solid state systems is the local density approximation (LDA). The potential which is applied to each wavefunction at each point in space is assumed to depend only on the electron density at that point (rather than the more general case of being a functional of the charge density everywhere), and is assumed to be the same as for a uniform electron gas of the same density. This approximation works quite well for determining the ground state properties of bulk systems. It does have several well known systematic errors, including an underestimate of the band gap for semiconducting and insulating systems. This is not surprising since there is no reason to expect density functional theory to say anything meaningful about the empty conduction band, which does not contribute to the ground state energy. The other fault, an overestimate of the cohesive energy of solids (the energy difference between the solid and the gas), is caused mainly by the inaccuracy of LDA in computing the energy of isolated atoms in the gas. Energy differences between different solid systems are quite accurate. This method is free of empirical parameters, since all the necessary functions, however approximate, do not depend on the system in question. To reduce the number of degrees of freedom in the calculations, electrons in the core of the atoms, which do not react to the neighboring atoms and are therefore irrelevant in computing the energy of the system for different atomic configurations, are often removed using the pseudopotential approximation. The core electrons and the nucleus of the atom are lumped together, and only their combined effects on the valence electrons participating in the interatomic bonding are computed. This also helps smooth out the potential near the core, easing the need for high resolution representation of the rapidly varying, nearly singular potential near the nucleus. Some empirical input can be used to develop these pseudopotentials, particularly to optimize this smoothing, but it is not necessary, and the method can be used without any fitting

parameters.

This combination of methods and approximations, DFT/LDA with pseudopotentials, is the state of the art technique for calculating the energies and forces on atoms for bulk systems with more than a few atoms. It is not computationally cheap, requiring considerable resources to get accurate results. The eigenvalue equations for the single particle wavefunctions are typically solved using a basis, most often a Gaussian orbital basis or a plane wave basis, where the interactions between different basis elements $|\phi_i\rangle$ are stored in a matrix

$$H_{ij}[n(r)] = \langle\phi_i|H[n(r)]|\phi_j\rangle. \tag{2.5}$$

A large number of basis elements are needed to describe the wavefunctions, and solving the resulting eigenvalue equation requires finding the eigenvalues and eigenvectors of the correspondingly large matrix $\boldsymbol{H}$. The matrix form for the eigenvalue equation is

$$H_{ij}\psi_j^n = E^n\psi_j^n, \tag{2.6}$$

if the basis elements are orthogonal, as is the case for a plane wave basis. The charge density, which affects the matrix elements, must also be determined self-consistently through an iterative procedure of guess and refinement. Implementations of this method can typically compute the energies of a few tens or hundreds of configurations of a few hundred atoms on a desktop workstation in one day. They also take a time that scales as the number of atoms cubed and storage that scales as the number of atoms squared, making simulation of larger systems prohibitively expensive if more than a few configurations need to be considered.

2.1.3 Tight Binding

A more simplified quantum mechanical method for treating solid state systems is known as tight-binding (TB). The first simplifying approximation is that the electrons are non-interacting. This reduces the problem to finding the eigenvalue spectrum of a single

particle Hamiltonian

$$\mathbf{H}|\psi^n\rangle = E^n|\psi^n\rangle, \tag{2.7}$$

which gives a spectrum of eigenvalues E^n and eigenvectors ψ^n. The total energy of the electronic part of the problem, the band structure sum, is

$$E_{bs} = \sum_{\text{occ}\,n} E^n. \tag{2.8}$$

The sum starts at the lowest eigenvalue, and includes as many eigenstates as are necessary to place two electrons in each state following the Pauli exclusion principle.

In the TB method the basis used for representing the Hamiltonian matrix is that of localized atomic orbitals, i.e. orbitals with the angular symmetry of eigenstates of a spherical potential. For silicon, these typically comprise one spherically symmetric s orbital, and three p orbitals aligned along three perpendicular axes centered around each atom, all localized in space to lie near the atom about which they are centered. If the interaction between orbitals on different atoms is assumed to be independent of the position of all other atoms, known as the two-center approximation, the angular variation of the orbitals completely determines the angular variation of the corresponding Hamiltonian matrix elements. This gives the well known Slater-Koster form [45] for the angular part of the matrix elements. Relaxing the two-center approximation makes the dependence of the matrix elements on atomic positions much more complex, and is only rarely used in these semi-empirical models. For an sp^3 basis only four types of interactions are allowed by the angular symmetry (Fig. 2.1): $V_{ss\sigma}$ for the interaction of two s orbitals; $V_{sp\sigma}$ for the interaction of an s orbital along the axis of a p orbital; $V_{pp\sigma}$ for the interaction of two coaxial p orbitals; $V_{pp\pi}$ for the interaction of two p orbitals with parallel axes that are connected by a line perpendicular to their axis. The magnitudes of these four interactions and their variation with distance is not restricted by symmetry. In modern tight-binding models they are adjusted to optimize the results of the model in fitting various calculations, for example DFT/LDA energies or band structures, or experimentally measured energies or

band structure features. Some attempts have been made to compute these matrix elements without fitting but so far these have not been entirely successful (see Chapter 3).

One simplifying assumption often made in constructing TB models is that the orbitals on different atoms are orthogonal to one another. For a given structure, it can be shown that neglecting the nonorthogonality is equivalent to a shift in the total energy of the system [46]. A pair repulsion term is used to compensate for this omission. However, there is no reason to expect that the form of the repulsive interaction will be the same for different structures, and that a model where the interaction was fit for a particular set of configurations will be transferable to other configurations. Nonorthogonal tight-binding models explicitly include the nonorthogonality, rather than approximating it as a pairwise repulsion. This complicates the functional form somewhat, since the overlaps of different orbitals must now be parameterized and fit. It also complicates the matrix problem that must be solved by introducing an overlap matrix $\boldsymbol{S}$ whose elements are

$$S_{ij} = \langle \phi_i | \phi_j \rangle \tag{2.9}$$

and gives a new generalized eigenvalue equation

$$H_{ij}\psi_j^n = E^n S_{ij}\psi_j^n. \tag{2.10}$$

In both orthogonal and nonorthogonal TB models the total energy of the system includes the band structure sum E_{bs} (Eq. 2.8 and an additional contribution from a pairwise repulsive interaction

$$E_{rep} = \sum_{\langle ij \rangle} V_{\text{rep}}(r_{ij}) \tag{2.11}$$

where the sum includes all pairs of atoms in the system. For orthogonal models the pairwise repulsion includes the effects of the nonorthogonality as well as the screened Coulomb repulsion between the nuclei of the atoms. For nonorthogonal models only the screened Coulomb repulsion contributes to the repulsive term.

TB methods have several advantages over DFT/LDA based methods, but also some important disadvantages. TB methods are much faster, since they use a minimal

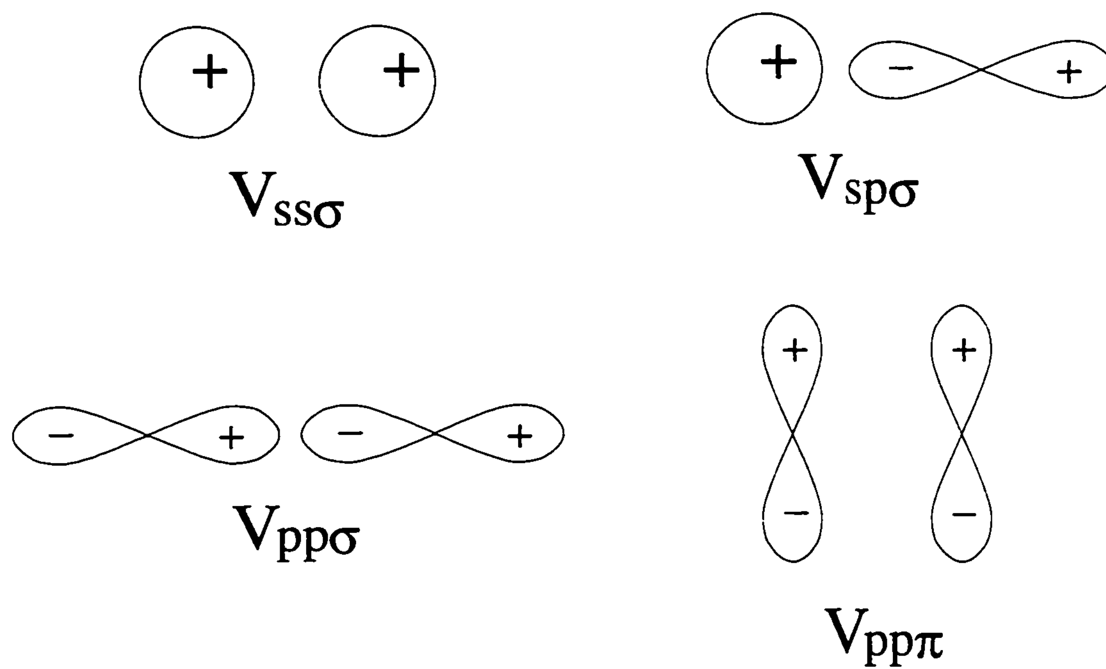

Figure 2.1: Diagrams of the four possible interaction parameters for s and p orbitals in the two-center approximation.

basis with only four basis elements per atom. Evaluating the Hamiltonian is very fast, and there is no need for a self-consistency iteration to compute the electronic charge density. Calculating the energy still requires computing the eigenvalues and eigenvectors of large matrices, which scales as poorly as for DFT/LDA, although with a smaller prefactor. A typical desktop workstation can compute the energy and forces for about 1000 configuration with 300 atoms in one day, about 100 times faster than a DFT/LDA calculation. Since the matrix elements are localized, the interactions between them are limited in range, and the the interaction matrices become sparse when the system size is larger than this distance. This can lead to faster methods for computing the energy than the exact diagonalization methods that scale as the number of particles cubed. In fact, within some approximations, methods that scale linearly with the number of particles are possible [47, 48, 49, 50, 51].

TB methods have two main disadvantages compared with *ab-initio* methods such as DFT/LDA. The first is that the approximations used are quite severe. Ignoring electronic interactions, using a minimal basis and ignoring three-center and higher order effects are all potential sources of error. The other disadvantage is that the magnitude and distance variation of the matrix elements must be determined empirically. This makes the development of TB models for different elements time-consuming, particularly in multi-component systems where the number of different interactions goes up as the square of the number of atomic species present. There is also the issue of transferability, since it is difficult to prove that just because a particular model with a particular set of parameters reproduced the fitting database accurately it will do so for other configurations.

2.1.4 Empirical Potentials

A completely different approach, neglecting the quantum mechanical nature of the electrons that mediate the interatomic bonds, leads to a very different formulation for the atomic interactions. Empirical potentials try to encapsulate the physics of the system by directly expressing the energy as a function of the interatomic positions. In covalent

solids this expression typically include pairwise terms that represent the strength of the interatomic bonds, and three-body terms that include the angular character of the bonds. The development of interatomic potentials for silicon is an old topic, starting with Keating type models [17, 52] that assume quadratic variation of the energy with bond stretching and bending but are only valid for small distortions from the ideal geometry. A range of functional forms and parameters presented in the modern literature, designed to be applicable to a wide rang of geometries, is reviewed by Balamane *et al.* [53].

The advantages and disadvantages of TB methods are further intensified in empirical interatomic potentials. Rather than just approximating the quantum mechanical effects, these potentials at worst ignore them altogether, or at best abstract them into effective interactions. This makes their accuracy suspect, and their validity away from the configurations to which they were fit quite unreliable. They are, however, much faster than any quantum mechanical method. Using a desktop workstation, 10^6 configurations with 1000 atoms each can be calculated in one day, 10^4 times faster than with TB methods. Moreover, because the interactions in covalent materials are localized and calculating the energy simply involves summing over pairs and triplets of atoms (no matrix eigenvalue equations are solved), the energy can easily be computed using computer storage and time that scales linearly with the number of particles.

2.2 Simulation Algorithms

Any method to compute the energy and forces of a configuration of atoms can be used in a number of ways. The forces can be used to integrate Newton's equations of motion forward in time in molecular dynamics (MD). In energy minimization (sometimes called lattice statics), the atoms are moved down the energy gradient to a minimum of energy. More elaborate algorithms are also available to find pathways between energy minima.

2.2.1 Molecular Dynamics

The most straightforward way of using the atomic energies and forces to simulate the time evolution of the system is by integrating Newton's equations of motion

$$\boldsymbol{F} = m\ddot{\boldsymbol{r}}. \tag{2.12}$$

Given an initial configuration the atomic positions and velocities are calculated by stepping forward in time by discrete steps. Since Newton's equations of motion conserve energy, the system (if the time step is small enough for accurate integration) evolves at constant energy. A number of algorithms can be used for this integration.

One is the Verlet or leap-frog algorithm [54]. It is very stable and simple to implement, but because the values for the velocity are always half a time step off from the position values it can not compute the velocity at the same time as the positions. Thus it is very hard to use with algorithms that simulate systems at constant temperature, pressure, or stress, all of which depend on contributions to the forces that depend both on the atomic positions (as in constant energy MD) and velocities. The other common algorithm used is the Gear predictor-corrector [55]. In this method the program keeps track of several high order time derivatives of the atomic position in addition to the acceleration, which is the second derivative. These can then be used to more accurately predict the positions of the atoms in the next time step. Because the positions, velocities and accelerations are available at the same time, the predictor-corrector method is often used with constant temperature, pressure or stress algorithms.

Constant Temperature Algorithms

One well known method for simulating a system at constant temperature is called the Nosé thermostat [56]. As discussed by Allen and Tildesley [57], the temperature can be defined in atomistic terms using the virial theorem. It is proportional to the kinetic energy of the system

$$\mathcal{T} = 2\mathcal{K}/3Nk_{\mathrm{B}} \tag{2.13}$$

where $\mathcal{K}$ is the kinetic energy of the system and N is the number of atoms. To keep the temperature constant an additional degree of freedom s is added to the system which scales all of the atomic velocities

$$\boldsymbol{v}_i = s\dot{\boldsymbol{r}}_i \tag{2.14}$$

and the kinetic energy

$$\mathcal{K} = \sum_i \frac{1}{2} m_i (s\dot{r}_i)^2. \tag{2.15}$$

An extended system Lagrangian with an additional kinetic energy term

$$\mathcal{K}_s = \frac{1}{2} Q_s \dot{s}^2 \tag{2.16}$$

and potential energy term

$$\mathcal{V}_s = (3N - 3) k_{\rm B} T \log s, \tag{2.17}$$

where T is the applied temperature, is used to generate the equations of motion for the atoms and the velocity scaling degree of freedom, which are then integrated in time. The resulting equations are

$$\ddot{\boldsymbol{r}}_i = \boldsymbol{F}_i / m s^2 - 2\dot{s}\dot{\boldsymbol{r}}_i / s \tag{2.18}$$

and

$$\ddot{s} = \sum_i m_i \dot{r}_i^2 s / Q_s - (3N - 3) k_{\rm B} T / s Q_s. \tag{2.19}$$

It can be shown that the resulting system is sampling the canonical ensemble [56]. One adjustable parameter Q_s is used, setting the rate at which the system reacts to fluctuations in temperature. Unfortunately, it is difficult to determine a good value for this parameter (one that minimizes the fluctuations without causing numerical instability), particularly when two different phases with different thermal properties are present. A more *ad-hoc* approach, but one that is still quite useful, is velocity rescaling. One can either randomly select a small fraction of the atoms every time step and randomize their velocities from a Boltzmann distribution corresponding to the correct temperature, or rescale all of the atomic velocities uniformly to reach the correct average temperature. Both of these actions

disturb the atomic motions and introduce discontinuities that confuse the time integration, and should be done as rarely as possible during the simulation.

Constant Pressure Algorithms

One issue in the field of atomistic simulations is how to deal with the edges of the finite samples that are being simulated. The conventional solution is to use three vectors, $\boldsymbol{a}_1$, $\boldsymbol{a}_2$, and $\boldsymbol{a}_3$ to define a unit cell which is repeated in all space. The periodic images of each atom in position $\boldsymbol{r}_i$ are

$$\boldsymbol{r}'_i = \boldsymbol{r}_i + l\boldsymbol{a}_1 + m\boldsymbol{a}_2 + n\boldsymbol{a}_3 \tag{2.20}$$

where l, m, and n are integers. The volume of the unit cell is determined by the three vectors, and is fixed as long as those vectors are fixed. An definition of pressure useful for atomistic simulations is

$$\mathcal{P} = \rho k_{\rm B} T + \mathcal{W}/V \tag{2.21}$$

where ρ is the number density and V is the volume of the system. The quantity $\mathcal{W}$ is called the internal virial, and equals the derivative of the energy of the system with respect to uniform dilation

$$\mathcal{W} = \left. \frac{\partial E\left[\{a^{1/3}\boldsymbol{r}_i\}\right]}{\partial a} \right|_{a=1} . \tag{2.22}$$

One algorithm for maintaining a constant pressure was developed by Andersen [58]. In a manner analogous to the Nosé thermostat, an additional degree of freedom is used to scale the unit cell vectors and atomic positions uniformly. A corresponding term is added to the extended system Lagrangian, and the equations of motion are integrated as before. An extension of this method to more general deformation of the unit cell was developed by Parinello and Rahman [59, 60, 61], where the entries in the matrix of unit cell column vectors

$$\boldsymbol{H} = [\boldsymbol{a}_1 \boldsymbol{a}_2 \boldsymbol{a}_3] \tag{2.23}$$

are used as dynamical variables. The real atomic positions are defined in term of scaled atomic positions $\boldsymbol{s}$ (not the same as the scalar factor s in the Nosé constant temperature algorithm) via

$$\boldsymbol{r} = \boldsymbol{H}\boldsymbol{s}. \tag{2.24}$$

The kinetic energy term associated with $\boldsymbol{H}$ is

$$\mathcal{K}_V = \frac{1}{2} Q_V \sum_{\alpha} \sum_{\beta} \dot{H}^2_{\alpha\beta} \tag{2.25}$$

where α and β are x, y, or z, and the potential energy term is

$$\mathcal{V}_V = PV \tag{2.26}$$

where P is the applied pressure, and V, the system volume, is

$$V = \det H. \tag{2.27}$$

The corresponding equations of motion are

$$\ddot{\boldsymbol{s}} = \boldsymbol{H}^{-1}\boldsymbol{F}/m - \boldsymbol{G}^{-1}\dot{\boldsymbol{G}}\dot{\boldsymbol{s}}, \tag{2.28}$$

where $\boldsymbol{G} = \boldsymbol{H}^T\boldsymbol{H}$, and

$$\ddot{\boldsymbol{H}} = (\boldsymbol{\mathcal{P}} - 1P)V(\boldsymbol{H}^{-1})^T/Q_V. \tag{2.29}$$

The matrix $\boldsymbol{\mathcal{P}}$ is an extension of the expression in Eq. 2.21

$$\mathcal{P}_{\alpha\beta} = \frac{1}{V} \sum_i m_i (\boldsymbol{H}\dot{\boldsymbol{s}}_i)^T_\alpha (\boldsymbol{H}\dot{\boldsymbol{s}}_i)_\beta) + \frac{\partial E\left[\{\boldsymbol{a}\boldsymbol{r}\}\right]}{\partial a_{\alpha\beta}}. \tag{2.30}$$

2.2.2 Energy Minimization

It is useful to be able find a local energy minimum nearby to a given an atomic configuration. It is then possible to find the lowest energy structures near a configuration obtained in an MD simulation, or to introduce some feature, such as a defect, by hand and see how the system relaxes to accommodate the change. A number of algorithms can be used for this purpose. The simplest one, when only a local minimum is needed, is known

as steepest descent. At each step the atoms are displaced parallel to the atomic forces by an amount proportional to the magnitude of the force. This algorithm can be inefficient, for example in the case of a long narrow valley in the potential energy surface [62]. It usually takes many steps almost perpendicular to the long axis of the valley, rather than taking one long step parallel to that axis to the vicinity of the energy minimum. An alternative method, the conjugate-gradient algorithm, generates a sequence of directions that are optimal in the case of a perfectly quadratic potential energy surface. This, of course, is rarely the case, but the algorithm is still quite efficient, particularly near energy minima where the potential is often almost quadratic. More elaborate methods can be used to compute a global energy minimum. In one such approach, simulated annealing [63], the system is perturbed randomly in configuration space, but the move is rejected with some probability if the energy of the system is higher than in the previous configuration. Thus the system can move up and over energy barriers in order to find lower energy configurations.

2.2.3 Low Energy Path Finding

A wide variety of important phenomena in materials science, including SPEG, are thermally activated. The rates of these processes are controlled by the probability that the system will experience a local energy fluctuation that will carry it over an energy barrier, which depends on the size of the barrier. It is therefore very useful to be able to find the lowest energy pathway for the system between two different locally stable states, since the maximum energy along this path will control the rate at which the system can transform from one to the other. One way to find this path is to connect the initial and final states with a line in configuration space called the reaction coordinate. The system is then moved along this line, and allowed to relax perpendicular to it. This is easy to implement with conjugate-gradient relaxation of the atomic positions, constrained not to move along the line. However, if the lowest energy path is perpendicular to the reaction coordinate, or worse yet backtracks along the reaction coordinate, the procedure will fail.

At some point moving the system infinitesimally along the line will cause it to relax to a completely different configuration.

A more robust algorithm, originally developed by Karplus [64], is to make a chain of configurations connecting the initial and final states, and constrain subsequent configurations along the chain to stay within some distance from one another. like beads on a string. The total energy of all the configurations along the path is then minimized, either with a sophisticated algorithm like simulated annealing, or a less computationally demanding one like conjugate-gradient.

Chapter 3

Tight-Binding Hamiltonians for Silicon

3.1 Introduction

Tight-binding (TB) Hamiltonians have been used for many years to describe the electronic structure and energetics of many materials (For a comprehensive text see Ref. [65], and for more recent reviews see Refs. [66, 67]. Using a minimal basis of atomic-like orbitals centered around each atom, with parameters usually fit to the band structure of specific crystal structures at high symmetry points, these models are fairly successful. The electronic contribution to the energy comes from the sum over the occupied part of the band structure. Another term, accounting for some combination of the ignored nonorthogonality of the orbitals and the Coulomb repulsion of the nuclei is then added via a two-body potential. All of these models for silicon use a minimal sp^3 basis centered around each atom. The vast majority of these models use the two-center approximation, assuming that the interaction between two orbitals on different atoms depends only on the positions of the two atoms. One modern model [68] attempts to approximately include some of the neglected interactions, but no useful methods for parameterizing the three-

center terms in general form have been used.

In all but one TB model for silicon [69] elements centered on each atom are orthogonal to each other, and do not interact. In addition, in most older models [70, 71, 72, 69, 73], matrix elements on different atoms are assumed to be orthogonal to each other. The effects of the neglected nonorthogonality can be shown to be equivalent to a pairwise repulsive interaction between the atoms [46], but the form of the interaction is not necessarily the same for different structures. The effects of transforming from a nonorthogonal basis to an orthogonal one can be included by replacing the Hamiltonian matrix $\boldsymbol{H}$ with the matrix product

$$\boldsymbol{H}' = \boldsymbol{S}^{-1/2}\boldsymbol{H}\boldsymbol{S}^{-1/2} \tag{3.1}$$

where S is the matrix of overlaps between basis orbitals $|phi_i\rangle$

$$S_{ij} = \langle\phi_i|\phi_j\rangle\,. \tag{3.2}$$

This orthogonalization makes the effective range of interactions in the orthogonal basis longer, since the range of the overlaps is added to the range of the original Hamiltonian matrix. Since each element $\boldsymbol{S}^{-1/2}$ is a function of many elements of $\boldsymbol{S}$, the orthogonalization also makes each elements of the orthogonal basis Hamiltonian $\boldsymbol{H}'$ dependent on the positions of many atoms, introducing more non-two-center terms.

A number of more recent TB models [74, 75, 76, 77, 78] have therefore explicitly used nonorthogonal bases. This increases the number of parameters needed for the model since the overlap matrix elements need to be described, but removes the need for some potentially troublesome approximations. In the following sections I will describe a nonorthogonal TB model [79, 80] we developed for calculating the total energy of bulk silicon systems. I will also discuss the results of this model, two other nonorthogonal TB models, those of Menon and Subbaswamy [74, 75] and Frauenheim *et al.* [77, 78], and DFT/LDA calculations, for the energetics of bulk structures, point defects and surfaces. Since we have not yet had time to test the most recent revision of Menon and Subbaswamy's

model (presented in Ref. [76]) I will not present results for that variant of the model.

3.2 Nonorthogonal Tight-Binding Models

3.2.1 Extended Hückel Theory Models

Our model is based on the conventional nonorthogonal TB formulation in the two-center approximation. We assume that orbitals on the same atom are orthogonal and non-interacting, but orbitals on different atoms are not orthogonal, and do interact. In all cases the interactions between two orbitals only depend on the positions of those two atoms. The minimal basis consists of one s and three p orbitals centered around each atom. In the following discussion I will denote our model as NO-TB. This model is based on the model of Menon and Subbaswamy, which I will denote as MS-TB. Both use extended Hückel theory [81] to reduce the number of parameters necessary to describe the matrix elements for overlaps and interactions. Traditionally, extended Hückel theory was used to derive the Hamiltonian matrix elements from the overlap matrix elements that were calculated explicitly from atomic orbitals. In our work and that of Menon and Subbaswamy, the order is reversed. From hypothetical orthogonal Hamiltonian matrix elements that are assumed to have a simple functional form, we derive overlap matrix elements, and a corresponding nonorthogonal Hamiltonian. To calculate the total energy we then solve the generalized eigenvalue problem, add the eigenvalues of the occupied states, and a pairwise repulsive interaction. Since it does not have to account for the nonorthogonality this repulsion is quite weak.

The hypothetical orthogonal TB Hamiltonian matrix elements are of the form

$$V_{\lambda\lambda'\mu}(r) = V_{\lambda\lambda'\mu} \exp(-\alpha(r - d_0))C(r) \tag{3.3}$$

where $V_{\lambda\lambda'\mu}$ is the interaction for orbitals of type λ and λ' (s or p), and μ is the type of overlap configuration (σ or π). d_0 is the ideal bond length in the diamond structure, so that $V_{\lambda\lambda'\mu}$ is the interaction strength at the diamond structure equilibrium volume. The

distance dependence is a simple exponential multiplied by a cutoff function

$$C(r) = \begin{cases} 1.0 & r < R_c \\ \frac{1}{2}\left[1 + \cos\left(\frac{\pi(r-R_c)}{W_c}\right)\right] & R_c < r < R_c + W_c \\ 0.0 & r > R_c \end{cases} \quad (3.4)$$

which smoothly restricts the interaction to a finite range by interpolating from 1.0 to 0.0 between $r = R_c$ and $r = R_c + W_c$. Extended Hückel theory then gives the following expression for the overlap matrix elements

$$S_{\lambda\lambda'\mu} = \frac{2V_{\lambda\lambda'\mu}}{K(r)(\epsilon_\lambda + \epsilon_{\lambda'})}, \quad (3.5)$$

where ϵ_λ is the on-site Hamiltonian matrix element for an orbital of type λ, and $K(r)$ is the Hückel nonorthogonality coefficient which varies with distance as

$$K(r) = K_0 + C_0(r - d_{\text{min}})^2. \quad (3.6)$$

The four symmetry allowed interactions, $ss\sigma$, $sp\sigma$, $pp\sigma$ and $pp\pi$ are then combined to give the overlap matrix elements and hypothetical orthogonal Hamiltonian matrix elements for atoms in arbitrary geometries using the angular functions, as discussed in Harrison [82]. The nonorthogonal matrix element H_{ij} for the interactions between orbitals i and j on atoms i' and j' are then given by

$$H_{ij} = \left(1 + \frac{1}{K_{i'j'}} - S_{2_{i'j'}}^2\right) V_{ij}. \quad (3.7)$$

The function

$$S_2(r) = \frac{S_{ss\sigma}(r) - 2\sqrt{3}S_{sp\sigma}(r) - 3S_{pp\sigma}(r)}{4} \quad (3.8)$$

is the overlap between two sp^3 hybrids pointed at each other. In some versions of their model Menon and Subbaswamy [75] erroneously add a $V_{pp\pi}$ term to $S_2(r)$, but we use the correct expression as given by Harrison [83].

The band-structure energy is given by the sum over the occupied single particle states generated by the generalized eigensystem

$$H_{ij}\psi_j^n = E^n S_{ij}\psi_j^n. \quad (3.9)$$

The remaining contribution to the total energy comes from the pairwise repulsion

$$V_{\text{rep}} = \chi_0 \exp(-4\alpha(r - d_0)). \tag{3.10}$$

This repulsion accounts for the screened Coulomb repulsion between the nuclei, and is quite small in both our work and that of Menon and Subbaswamy. The total energy is then

$$\sum_{\text{occn}} E^n + \sum_{\langle ij \rangle} V_{\text{rep}}(r_{ij}), \tag{3.11}$$

where i and j are indices over the atoms. The corresponding force on an atom is proportional to the derivative of the total energy with respect to the atomic position. Using the Hellmann-Feynman theorem [84, 85] to take the derivative of the band-structure energy, the force is

$$\vec{F}_i = -\sum_{\text{occn}} \left\langle \psi_n \left| \frac{\partial H}{\partial \vec{r}_i} - E_n \frac{\partial S}{\partial \vec{r}_i} \right| \psi_n \right\rangle - \sum_j \frac{\partial V_{\text{rep}}(r_{ij})}{\partial \vec{r}_{ij}} \tag{3.12}$$

There are a number of parameters in this formulation. There are two on-site energies ϵ_s and ϵ_p, four interaction strengths $V_{ss\sigma}$, $V_{sp\sigma}$, $V_{pp\sigma}$, and $V_{pp\pi}$, the decay rate for the interaction α, the three constants controlling the variation of the Hückel nonorthogonality coefficient, K_0, C_0 and d_{min}, and the magnitude of the pairwise repulsion χ_0. Menon and Subbaswamy take the on-site energies and interaction strengths *a-priori* from Harrison's parameter free model [86]. With no justification they also fix C_0 to equal α, and d_{min} to equal d_0. They then fit the remaining three parameters, α, K_0 and χ_0 to the bond lengths and vibration frequencies in bulk diamond structure silicon and the silicon dimer. Rather than fix most of these parameters, we allow them to vary in the fitting, which will be discussed in sec. 3.3.

3.2.2 Density Functional Tight-Binding

Frauenheim *et al.* [77, 78] developed a completely different methodology for generating the elements necessary for a nonorthogonal TB Hamiltonian in the two-center approximation, which I will denote in the following as DF-TB. They start with an isolated

silicon atom in a confining potential that they simulate using DFT/LDA. The eigenfunctions they generate, $|\phi_i\rangle$ are atomic-like wavefunctions with the expected symmetry, compressed by the confining potential with respect to the free atom eigenfunctions. They then explicitly compute the TB matrix elements

$$H_{ij} = \langle \phi_i | H | \phi_j \rangle \tag{3.13}$$

and

$$S_{ij} = \langle \phi_i | \phi_j \rangle \,. \tag{3.14}$$

The total energy is in the same form as Eq. 3.11, with a band-structure term and pair repulsion term. The pair repulsion term is obtained by fitting the total energy vs. volume curve of bulk diamond structure silicon and the energy vs. bond length curve of the silicon dimer to DFT/LDA calculations.

This procedure for calculating the TB matrix elements is very appealing. It is straightforward, and fitting is only needed to compute a scalar function of one variable. It can also be easily used for any number of elements, where the increased number of parameters for all the combinations makes exhaustive fitting prohibitive. However appealing this formulation might be, it must also be accurate to be useful. As I will discuss in the next section, this model has some shortcomings revealed in our calculations for several test systems.

3.3 Fitting Procedure

As I mentioned in the previous section, we fit most of the parameters in our TB model. The only one which was fixed was d_0, since it can be changed arbitrarily by rescaling all of the interaction strengths. The other parameters were fit to a database of DFT/LDA calculation and experimental results, including many total energy calculations and a few band structure features. To represent the properties of experimentally relevant bulk phases we included the experimental cohesive energies, volumes and bulk moduli of

the diamond structure and β-Sn structure phases, two lowest energy experimentally observed structures for silicon. We also included the valence band width (from DFT/LDA) and minimum band-gap (from experiment) in the diamond structure. To represent the energetics of point defects we included the ideal vacancy and the ideal tetrahedral and hexagonal interstitials. Both the vacancy and the interstitials are very important for the behavior of silicon, since they control many solid-state processes such as bulk diffusion [87]. We also considered one activation energy, the saddle-point of the concerted-exchange diffusion pathway. Concerted-exchange is a theoretically proposed mechanism for diffusion in silicon that does not rely on any point defects [88]. At the saddle-point the two atoms exchanging sites are breaking old bonds and forming new ones in an otherwise undistorted environment. This is qualitatively different from the activated states of defects like the interstitials, where the bonds being broken and formed are highly strained by the presence of the defect.

These structures were chosen to represent the range of geometries expected in experimentally relevant situations, such as defective diamond structure silicon, perhaps slightly over-coordinated because of a high applied pressure, or amorphous silicon. The two bulk phases include information about a perfect covalent four-fold coordinated network and a low energy metallic structure. The defects include information about over and under-coordination defects, present not only in the crystal, but also in amorphous systems as dangling or floating [36, 89] bonds. The hexagonal interstitial is also the activation barrier to the diffusion of an atom between two tetrahedral interstitial sites, and gives information about bond breaking and formation in the presence of defects. The concerted-exchange saddle-point is the activation barrier to the exchange of two atoms, and gives information about bond breaking in an otherwise perfect crystal.

Using a simulated-annealing algorithm [63], we minimized the RMS deviation of the quantities being fit by varying the model parameters. We assigned a weight to each quantity in evaluating the goodness of fit by trial and error. If a fit converged to a region

	NO-TB	MS-TB
ϵ_s (eV)	-13.10	-13.55
ϵ_p (eV)	-5.85	-6.52
$V_{ss\sigma}$ (eV)	-1.82	-2.37
$V_{sp\sigma}$ (eV)	1.66	2.52
$V_{pp\sigma}$ (eV)	3.09	3.32
$V_{pp\pi}$ (eV)	-0.58	-1.07
α (Å^{-1})	1.726	1.6
$d_{\rm min}$ (Å)	2.255	2.36
K_0	1.420	1.7
C_0	1.965	1.6
χ_0 (eV)	0.00822	0.05

Table 3.1: Parameters for the NO-TB and MS-TB Hamiltonians: ϵ_s and ϵ_p are the on-site energies for the s and p orbitals, respectively. $V_{\lambda\lambda'\mu}$ are the symmetry allowed interactions between orbitals on different atoms at $r = d_0$, and α is the exponential decay rate of the interaction with distance (Eq. 3.3). K_0 and C_0 are the value of $K(r)$ at $d_{\rm min}$ and its curvature (Eq. 3.6). χ_0 is the magnitude of the pairwise repulsion at $r = d_0$ (Eq. 3.10).

where the value of some quantity being fit was unacceptably bad, we increased the weight of that quantity. The annealing temperature, also an important part of any simulated-annealing procedure, was also varied by trial and error to give a substantial number of up-hill moves but not enough to turn the search into a random walk in parameter space. The parameters resulting from the fitting are listed in table 3.1. I emphasize that these parameters are not necessarily the optimal set for our fitting database. The space available is too large, and evaluating the energies too expensive, for an exhaustive search. These parameters should only be considered a reasonable compromise given the computer power and time constraints.

3.4 Tests

As well as evaluating the fitting database for each of the three TB Hamiltonians we considered, we also calculated the energies of several additional structures as tests of the models. In the following sections I will discuss these results, comparing our tight-binding

Hamiltonian (NO-TB), the work of Menon and Subbaswamy (MS-TB) and Frauenheim *et al.* (DF-TB), and DFT/LDA calculations or experiment. The configurations we considered include several bulk structures in addition to those in the fitting database, the formation and relaxation energies of the point defects in the fitting database, and the surface energies and relaxation energies of the (100) and (111) surfaces.

3.4.1 Bulk Structures

The results for the total energy as a function of atomic volume are plotted in Fig. 3.1. The diamond structure is the lowest energy bulk phases of silicon, with perfect four-fold coordination and sp^3 bonding. β-Sn is a relatively low energy six-fold coordinated structure that is experimentally observed in silicon at high pressure [90, 91]. It has also been extensively studied with *ab-initio* methods [92, 93, 94]. These two structures were in the fitting database, and as expected the NO-TB model reproduces the DFT/LDA results for the cohesive energy (corrected for the DFT/LDA overbinding) and equilibrium volume. The other two models considered do not do as well in describing these structures. The DF-TB model does well for the diamond structure, but significantly overestimates the equilibrium volume and the energy difference from the diamond structure. The MS-TB model reproduces both volumes accurately, but greatly overestimates the energy difference between the two structures. We also considered two other bulk phases that were not in the fitting database, the body-centered-tetragonal-5 structure (BCT5) and the simple cubic structure (SC). The first is a five-fold coordinated structure proposed by Boyer [93]. The second has six-fold coordination. Both are relatively low energy metallic structures for silicon that have been studied theoretically. None of the TB Hamiltonians describe these structures well, although in all cases the diamond structure is the lowest in energy. The NO-TB model shows all three structures to be almost degenerate in energy. The MS-TB model still overestimates the energy differences between the structures, but incorrectly shows BCT5 and SC to be lower in energy than β-Sn. The DF-TB model also gets the

wrong energy ordering in the over-coordinated structures, and predicts equilibrium volumes that are much too high.

We also computed the bulk modulus for each of these structures by fitting the energy vs. volume curve to the Birch-Murnaghan equation of state [95]. Those results are listed in Table 3.2. As expected, the NO-TB model reproduces the DFT/LDA values for the diamond and β-Sn structures quite well. The MS-TB model overestimates all of the bulk moduli by about half, and the DF-TB, except for the diamond structure bulk modulus to which it was fit, overestimates them by almost a factor of two. As a more sensitive test of our TB model we calculated the three elastic constants, tabulated in Table 3.3. Our model reproduces the elastic constants with errors of 12% – 33%, a substantial improvement over the MS-TB model which errs by up to 90%. The DF-TB model does substantially better than either of other TB models, including correctly predicting the Cauchy discrepancy $c_{12} - c_{44} < 0$.

Since our emphasis was on the energetics of the systems, we did not put very much weight on the band-structure during the fitting. We did ensure that the valence band width and the minimum band gap remained reasonable. A comparison of various band-structure features is given in Table 3.4. The NO-TB model has a very good valence band width, and the smallest minimum band gap (although it is still too large). The other two TB models overestimate the minimum gap even more, and none of the three place it at the right point in the Brillouin-zone.

3.4.2 Point Defects

Point defects are present in even the best silicon samples, and are believed to be responsible for important processes such as diffusion. We therefore expect that accurately reproducing their energetics will be important for realistic simulation of imperfect crystals and the amorphous phase. As representative geometries we used the Si self-interstitial in the tetrahedral and hexagonal configurations, and the vacancy. All of the TB calculations

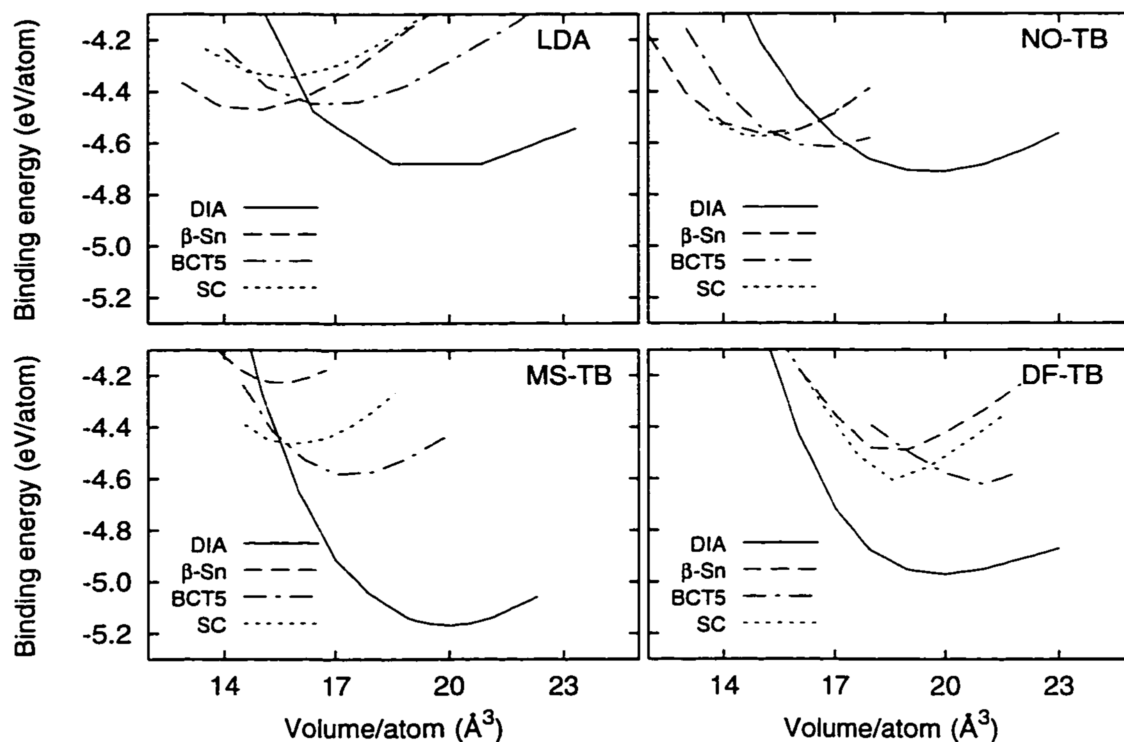

Figure 3.1: Cohesive energy as a function of atomic volume curves for the diamond structure (DIA), β-Sn, body-centered-teragonal-5 (BCT5), and simple cubic (SC) lattices for four models (DFT/LDA, NO-TB, MS-TB, DF-TB).

Structure	DFT/LDA	NO-TB	MS-TB	DF-TB
Binding Energy (eV/atom)				
diamond	-4.70	-4.71	-5.19	-4.97
β-Sn	-4.47	-4.57	-4.27	-4.48
BCT5	-4.45	-4.62	-4.64	-4.62
SC	-4.35	-4.58	-4.50	-4.58
Equilibrium Volume (Å^3/atom)				
diamond	19.67	19.67	19.98	19.87
β-Sn	14.63	15.16	15.70	18.67
BCT5	16.77	16.67	17.17	20.98
SC	15.44	15.02	15.63	18.99
Bulk Modulus (GPa)				
diamond	98.0	104.8	153.5	115.1
β-Sn	129.1	138.1	164.7	190.5
BCT5	111.4	134.6	163.3	265.5
SC	117.3	147.5	182.0	244.7

Table 3.2: Bulk properties for various lattice structures computed by DFT/LDA and three TB models. The DFT/LDA cohesive energies were uniformly shifted to agree with experimental results for the equilibrium energy.

	DFT/LDA[a]	NO-TB	MS-TB	DF-TB
c_{11} (GPa)	166	145	218	185
c_{12} (GPa)	63.3	84.5	121	80.1
c_{44}^{*} (GPa)		135	162	135
c_{44} (GPa)	79.3	53.4	81.6	89.5

[a]From Ref. [96]

Table 3.3: Elastic constants of the diamond lattice structure. c_{44}^{*} is the value of the elastic constant without including the relaxation of the atomic basis.

	DFT/LDA	NO-TB	MS-TB	DF-TB
Valence band width	11.92	11.75	13.83	10.69
Band gap at Γ	3.15	1.68	3.07	3.20
Minimum band gap	1.14	1.51	2.72	3.20
Minimum band and gap location	3/4 X	L	L	Γ

Table 3.4: Band structure features for diamond structure silicon. The DFT/LDA results include a 0.6 eV scissor-operator shift of the conduction levels [1, 2].

were done with a cube shaped 216 atom unit cell with one atom added or removed, and periodic boundary conditions. To sample the Brillouin zone we used only the Γ point, because of the large size of the unit cell. The DFT/LDA calculations found in the literature [97, 98, 99] that are used for comparison in the following discussion used a wide range of parameters.

Ideal Defects

The lowest energy interstitial configuration in silicon is believed to be the [110] split interstitial. However, we instead chose to simulate two simpler configurations, which may also be important metastable configurations in the path of a diffusing interstitial atom [100]. Our goal in choosing these was to be sure our model reproduces the energetics of some plausible configurations. The tetrahedral interstitial is one such high-symmetry, low energy configuration. The added atom has four neighbors at the corners of a tetrahedron, to which it can make four sp^3 bonds. Each of those four atoms end up with five neighbors, one of which is the interstitial. In the amorphous phase, which consists of a continuous random network of four-fold coordinated atoms with some defects, it is harder to define an interstitial position. However, an analogous over-coordinated defect which is easy to define is the floating bond [36, 89], i.e. the extra bond of an atom with five neighbors. The other interstitial configuration we considered is the hexagonal geometry, where the added atom is inserted in the middle of a six-fold ring of atoms. In this geometry the interstitial atom has six neighbors, each of which has five neighbors. This configuration is unstable, and a small perturbation perpendicular to the ring will cause the atom to relax to one of the two adjacent tetrahedral sites. This makes the hexagonal site the saddle-point configuration for diffusion between tetrahedral sites, and the energy difference between the two types of sites controls the rate of diffusion along the path.

Results for the ideal formation and relaxation energies of both types of interstitials are listed in Table 3.5. The NO-TB model, which was fit to the ideal formation energies of

	DFT/LDA[a]		NO-TB		MS-TB		DF-TB	
	$E_f^{\rm id}$	ΔE_f	$E_f^{\rm id}$	ΔE_f	$E_f^{\rm id}$	ΔE_f	$E_f^{\rm id}$	ΔE_f
Tetrahedral Interstitial	3.7 - 4.8	0.1 - 0.2	4.5	0.5	9.6	1.2	11.7	3.8
Hexagonal Interstitial	4.3 - 5.0	0.6 - 1.1	6.3	1.3	9.7	1.2	12.9	5.2
Vacancy	3.3 - 4.3	0.4 - 0.6	4.4	1.2	6.0	0.4	3.9	0.6

[a]Refs. [97, 98, 99]

Table 3.5: Formation energies for ideal point defects $E_f^{\rm id}$ and relaxation energies $\Delta E_f = E_f^{\rm relaxed} - E_f^{\rm id}$.

the interstitials, reproduces the results of DFT/LDA calculations well. The other two TB models overestimate the formation energies of the ideal defects by about a factor of two. This indicates a potential problem in using these Hamiltonians for simulations of either crystal or amorphous silicon where over-coordinated structures regularly occur. It also demonstrates the importance of fitting semi-empirical models to the range of geometries that are important for the application.

The vacancy, an example of a low energy under-coordinated defect, was also included in the NO-TB fitting database. Related under-coordination defects in amorphous silicon, or dangling bonds [36] are also observed in amorphous silicon [89]. The formation energies of the ideal vacancy calculated using DFT/LDA and the three TB models is listed in Table 3.5. The NO-TB model again accurately reproduces the energetics of this defect, and so does the DF-TB model. This indicates a qualitative difference between under and over-coordinated defects, where the DF-TB model did quite poorly, and emphasizes the importance of testing TB models in many geometries. The MS-TB model, as in the case of the interstitials, overestimates the formation energy by about a factor of two.

Relaxed Defects

As more challenging test of the TB Hamiltonians, each was used to relax the atomic configuration of each defect. A conjugate-gradient energy minimization algorithm was used [62] to relax the atomic positions. The results are listed in the second part of

Table 3.5. The vacancy and the hexagonal interstitial were stable for all the TB models. In the DF-TB model the tetrahedral interstitial relaxes into a split interstitial. To prevent the transformation we constrained the positions of the outer shell of atoms centered around the interstitial in the periodic cell. The difference in the way the constraint was applied accounts for the difference between out results and those of Frauenheim *et al.* [78]. The NO-TB model overestimates the formation energies, particularly for the tetrahedral interstitial and the vacancy. The MS-TB model only significantly overestimates the formation energy of the tetrahedral interstitial, but since its ideal formation energies are too high this also leads to high relaxed formation energies. The DF-TB model does well in reproducing the relaxation of the vacancy, but overestimates the relaxation energies of the interstitials by factors of 5 to 20. This leads to plausible relaxed formation energies (as reported in Ref. [78]) through the cancelation of errors in the ideal formation energies and the relaxation energies. In fact, both the MS-TB model and the DF-TB model predict *relaxed* formation energies for the interstitials that are higher than the DFT/LDA *ideal* formation energies.

The geometries of the relaxed defects and symmetry breaking during relaxation are subjects of current interest. Although we did not systematically test the symmetry breaking by perturbing the system, in many cases numerical noise caused the atomic relaxation program to break the symmetry spontaneously. All three TB models show an outward relaxation of the six-fold ring around the hexagonal interstitial, with no symmetry breaking. This is in qualitative agreement with DFT/LDA calculations of Kelly *et al.* [98]. The tetrahedral interstitial exhibits more interesting behavior. With the MS-TB Hamiltonian some of the neighbors relax in (toward the interstitial atom), some relax out (away from the interstitial atom), and the tetrahedral symmetry is completely broken. The DF-TB model also predicts a complete breaking of the symmetry, but all the neighbors relax outward. This may be an indication of the desire of the system to relax to a split interstitial configuration, a transition which is blocked by the constraint we applied. The

NO-TB model predicts that all the neighbors relax outward, with the interstitial moving toward one pair of atoms, breaking the tetrahedral symmetry. In contrast, DFT/LDA calculations [98] predict a relaxed configuration with the same symmetry as the ideal configuration, but do not specify in which directions the atoms move.

In agreement with DFT/LDA calculations [98, 99] all TB models predict an inward relaxation around the vacancy, although the relaxed structures vary considerably. The MS-TB and DF-TB model show very low symmetry structures. The NO-TB model shows a tetragonal symmetry structure, with two non-adjacent edges of the surrounding tetrahedron contracting by equal amounts. This is the only TB model which is even in qualitative agreement with the DFT/LDA calculations.

We have also calculated the diffusion energy for various defects. For the vacancy, there is a diffusion barrier of 0.3 eV (plus an additional 3.2 eV to form the vacancy). For the tetrahedral interstitial the diffusion barrier configuration is simply the hexagonal site, which is 1 eV higher than the relaxed tetrahedral formation energy of 4 eV. We also considered another activation energy, the concerted-exchange saddle-point [88]. The saddle-point energy (without allowing for relaxation) is 5.4 eV according to DFT/LDA calculations, and the NO-TB model, which includes this configuration in the fitting database, reproduces this value exactly. The other TB models overestimate this energy by 2–3 eV. The energy along the path is plotted in Fig. 3.2. Relaxing the saddle-point configuration while constraining the atoms from moving along the path gives the real energy barrier for diffusion along the pathway. All three TB model accurately reproduce the DFT/LDA results [88] that the two diffusing atoms move together by about 0.15 Å. However, all of them overestimate the relaxation energy of 0.9 eV by about a factor of 2.

3.4.3 Surface Energies

Surface energies and reconstruction provide an interesting test for the TB models. They involve geometries that are quite different from the region in which the NO-TB model

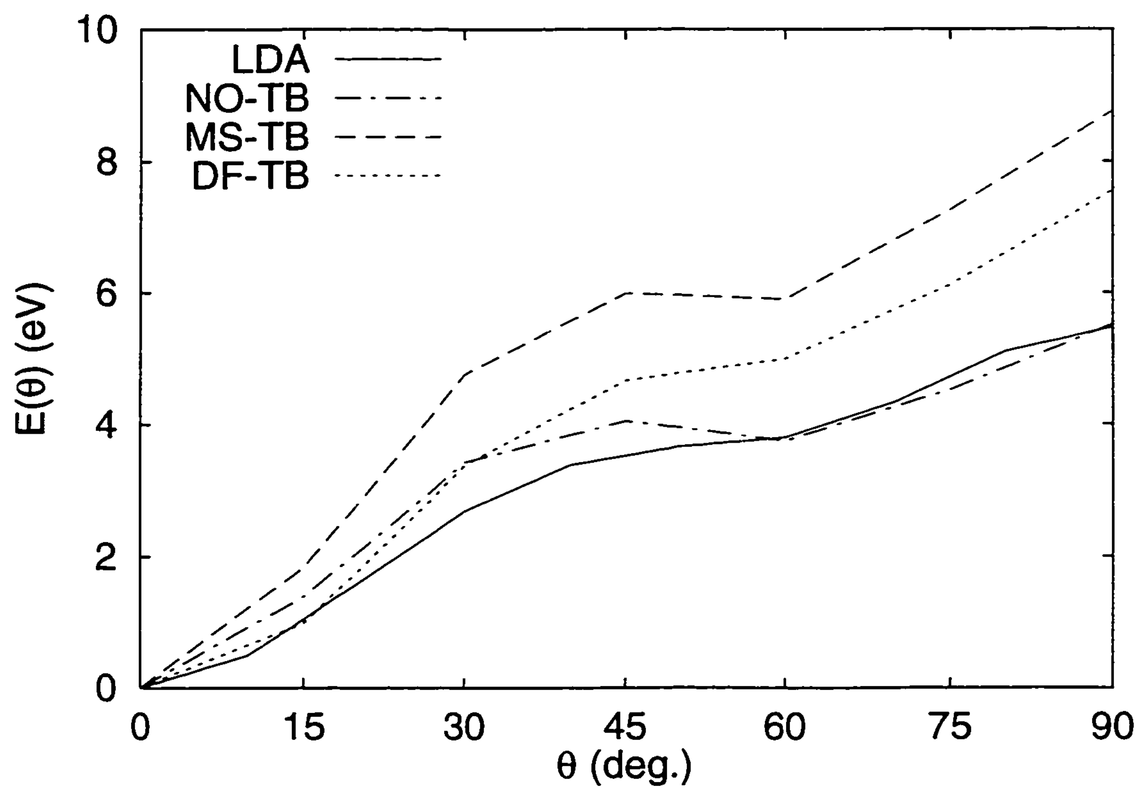

Figure 3.2: Energy along the concerted-exchange diffusion pathway, without relaxation.

was fit. To test the models we calculated the surface energies and some reconstruction energies of the (100) and (111) surfaces. These are two of the lowest energy surfaces in silicon, and most experimental and technological work is done on one of the two.

(100) **Surface**

The ideal (100) surface is dominated by chains running along [110] and [$1\bar{1}0$] directions. The simplest low energy reconstruction for this surface is the (2×1), where pairs of atoms in adjacent chains dimerize, and the dimers then tilt. Results for the ideal surface energy, relaxation energy for a surface with a (1×1) periodicity, and relaxation energy for the (2×1) reconstruction where the tilted dimers form spontaneously are listed in Table 3.6. All of the TB models give qualitatively correct results, with a stable tilted dimer at approximately the correct tilt angle. The MS-TB is the only one that gets the right surface energy and relaxation energy, with the other two TB models underestimating both. All the models also overestimate the distance between the dimerized atoms. This distance is fixed by the balance of forces on the greatly stretched bond between the dimer atoms and on the bonds to the substrate that are strongly tilted when the dimer is formed. Therefore it is not surprising that small changes in those energetics can lead to large changes in the dimer bond length.

(111) **Surface**

The (111) surface is the lowest energy surface of silicon, reconstructed in a (7×7) pattern. This reconstruction has been studied extensively both experimentally and theoretically [103, 104, 105]. Its dominant features are dimer bridges, adatoms on the surface, and a stacking fault beneath half of the reconstruction cell. The surface atoms in both halves are adatoms with a (2×2) periodicity. These adatoms in and of themselves have been hard to reproduce with empirical potentials, since they introduce a large strain in the substrate [106]. For simplicity we will simulate two high symmetry positions for these

		DFT/LDA[a]	NO-TB	MS-TB	DF-TB
Si(100)					
Ideal (1×1)	γ	2.5	1.5	2.4	1.9
Relaxed (1×1)	$\Delta\gamma$	-0.03	-0.03	-0.01	-0.01
Buckled dimer (2×1)	$\Delta\gamma$	-0.83	-0.53	-0.83	-0.62
	θ	15°	14°	12°	15°
	d (Å)	2.23	2.41	2.38	2.61
Si(111)					
Ideal (1×1)	γ	1.56	1.19	1.67	1.24
Relaxed (1×1)	$\Delta\gamma$		-0.020	-0.003	-0.007
(2×2) T_4	$\Delta\gamma$	-0.30	-0.26	-0.17	-0.07
(2×2) H_3	$\Delta\gamma$	-0.25	-0.26	-0.17	-0.15

[a]Refs. [101] and [102].

Table 3.6: Surface energies for the Si (100) and (111) surfaces. γ is the surface energy in eV per (1×1) cell; $\Delta\gamma$ is the relaxation energy relative to ideal (1×1) γ; θ is the tilt angle of dimers; d is the bond length of the dimer.

atoms, the T_4 and H_3 configurations. The T_4 adatom is stable according to DFT/LDA calculations, sitting in the center of a surface atom triangle directly above an atom in the second surface layer. In this configuration the adatom partially saturates three surface dangling bonds, and can make one partial bond to the atom underneath it, but introduces one more dangling bond. In the H_3 configuration the atom is in the middle of a surface atom hexagon, partially saturating three dangling bonds but introducing one more dangling bond. This configuration is metastable, but higher in energy than the T_4 configuration according to DFT/LDA calculations.

In Table 3.6 we list the ideal surface energies, and the relaxation energies for the unreconstructed (1×1) surface, and the T_4 and H_3 adatom (2×2) reconstructions. The ideal surface energies are reproduced fairly well by all of the TB models, again underestimated by the NO-TB and DF-TB models. All of the TB models underestimate the binding energies of the two types of adatoms, although the NO-TB model comes closest to reproducing the DFT/LDA values. However, none of the TB models gets the correct energy ordering, with the T_4 adatom lower in energy. This is still better than an empirical interatomic potentials [53], which do not predict stable adatom reconstructions at all.

3.5 Discussion and Conclusions

We compared three TB models for silicon to DFT/LDA calculations. All three are nonorthogonal models with sp^3 bases and use the two-center approximation. They vary greatly in how their parameters were derived. The DF-TB model uses contracted DFT/LDA atomic wavefunctions to explicitly calculate the appropriate integrals needed for the TB model. The MS-TB model, on the other hand, assumes very simple functional forms for all of the distance variations, and takes most of its parameters from Harrison's parameter free model. Our NO-TB model takes a third approach - we also use very simple functional forms, the same as in the MS-TB model, but we fit the values of the parameters to optimize the reproduction of energies for a database of relevant structures.

The range of behaviors among the models is large. All three reproduce the energetics of bulk diamond structure silicon quite well, and none does uniformly well for the higher coordination metallic phases. The NO-TB model reproduces the β-Sn structure well. since it was in the fitting database. The two models which were not fit to defect energies overestimate both their formation and relaxation energies by up to a factor of two. All the models reproduce qualitative features of the (100) and (111) surfaces. The MS-TB model does particularly well for the (100) surface, but none of the models accurately predict the small energy differences between different adatom positions on the (111) surface.

One observation that we made while fitting the NO-TB model is that there is a correlation between the band gap and the defect formation energies. Generally. when one increases, so does the other. This is consistent with the results for the MS-TB and DF-TB models, which have large band gaps and large formation energies for the defects. as well as somewhat larger surface energies. It is also consistent with a naive picture of the electronic aspects of the defects: they introduce dangling or floating bond states in the middle of the gap, so that a higher gap leads to a higher formation energy. The defect formation energies in the NO-TB model are too high, despite the fact that they are in the fitting database. To improve the fit we would have had to relax the restriction on the size of the band gap, but this would cause it to become unphysically small. We have chosen a compromise between these two features.

Developing TB models to describe the energetics of bulk silicon structures is a challenging task. The semi-empirical nature of these models makes it hard to use theoretical input to guide the functional forms and parameter values. Attempts to do this without fitting, such as the work of Frauenheim *et al.* [77, 78], have some shortcomings. Their current models do not reproduce the energetics of even simple point defects in crystalline silicon. Other approaches, like assuming a very simple functional form and taking the parameters *a-priori* from simple models, as in the work of Menon and Subbaswamy [74, 75], work reasonably well considering how little fitting is involved, but still do not adequately

reproduce the systems we are interested in. For the moment, we see no alternative to fitting the parameter values to a database of relevant information that encompass the range of systems that are of interest, in our case the energetics of plausible geometries like low energy bulk structures and point defects. Even with a precisely tailored database, the model must still be extensively tested to reduce the possibility of pathological behavior in some other regime.

The NO-TB model we have developed does quite well in reproducing the energetics of the bulk silicon systems we have tested, despite its simple functional form. Since we have tested a wide range of geometries that should include the configurations we expect in both crystal and amorphous silicon, we expect that it will be reliable in the simulation of such systems. In the next chapter I will discuss its application to the generation and analysis of realistic amorphous-crystal interfaces in silicon.

Chapter 4

Amorphous-Crystal Interfaces

The first step towards a microscopic understanding of SPEG is an understanding of the amorphous-crystal (a-c) interface. While a lot is known about both the crystal and amorphous phases individually, much less is known about the interface between the two. Experimental information is scarce because the region of interest is deep inside a solid, where no atomic resolution probes are available. Despite a number of computer simulation studies [22, 24, 25, 27, 29], there has been no detailed analysis of microscopic properties of the interface published so far. Pictures of the interface generated with hand-built models [15, 19] have been presented, but the samples are very small and it is hard to tell if the features present are representative of the real system.

Both the length and time scales needed to simulate an a-c interface samples are substantial. A large system is needed to allow the amorphous phase to exist without the periodic boundary conditions affecting the character of the amorphous phase, and to separate the two interfaces that must exist because of the periodicity. The simulation must explore phase space extensively to make sure that the system is not trapped in some small part of configuration space. While a simulation using *ab-initio* methods would be ideal, our computer power limitations would cause it to fall short on both size and time scales. Instead, we use a combination of empirical potentials and the nonorthogonal TB model

described in the previous chapter. We could also use the resulting structures as a starting point for more elaborate *ab-initio* simulations, but we expect that the essential features will remain unchanged.

4.1 Methods

To make the amorphous regions in our samples we simulate the melting and quenching of a portion of the system using constant temperature, constant stress MD. In this stage we use the Stillinger-Weber interatomic potential to describe the interatomic interactions. Many time steps of MD are needed, and an empirical potential is the only practical way of doing this simulation. Since the system is so far from equilibrium throughout most of this process we do not expect that the details of the interatomic forces will make a significant difference to the resulting structure. When the system has been brought relatively close to equilibrium we switch to forces from the TB model, and relax the atomic positions and unit cell size and shape. For the MD simulation we use a Gear predictor-corrector algorithm [55] to integrate the equations of motion with a 1 fs time step. To maintain constant temperature we rescale the atomic velocities uniformly once every 500 time steps so that the kinetic energy is appropriate for the temperature. To maintain zero stress we use an extended system Parrinello-Rahman method [59, 60, 61] with a mass of 200.0 in reduced Stillinger-Weber units.

We simulate a system with 320 atoms with periodic boundary conditions in all three directions. The interface is in the (001) plane, perpendicular to [001] direction which I will refer to as the z-axis. The simulation cell is a $[220] \times [2\bar{2}0] \times [005]$ box. To create the interface we melt and quench a part of the sample while keeping the rest crystalline by maintaining it below the melting point. The crystalline region consists of 128 atoms in 8 monolayers, kept at 100 K. The remaining 192 atoms, forming 12 monolayers, are in the amorphous region produced by quenching them from a 5000 K liquid state to 100 K. The 5000 K liquid was equilibrated for 2×10^4 time steps, and then cooled to 2000 K

over 2×10^4 time steps. Several samples were equilibrated at this temperature for varying amounts of time, and each was processed with the following procedure to produce a distinct *a*-c interface sample. To force the system to quench into a four-fold coordinated amorphous phase, rather than a higher coordination glassy phase, we use the technique suggested by Luedtke and Landman [107] and increase the bond angle forces by 50%. We then equilibrate the samples for 2×10^4 time steps, and then cool to 1000 K over 10^5 time steps. Then angular forces are reduced to the standard value over 10^4 time steps, and the samples are equilibrated for an additional 10^5 time steps and rapidly quenched to 100 K.

Six samples were produced with the Stillinger-Weber MD simulation. These samples were then relaxed using conjugate-gradient energy minimization [62] with forces from the nonorthogonal TB model. The changes during the relaxation were substantial, with over 10% of the atoms moving more than 0.25 Å, over 10% of the bond length, and a few atoms moving more than 1 Å. A typical relaxed sample is shown in Fig. 4.1. The six TB relaxed samples are used for all of the structural and energetic characterization in the following analysis.

4.2 Structural analysis

4.2.1 Bulk Properties

To characterize bulk properties of our samples we calculated two correlation functions, the radial pair distribution and the bond angle distribution. Results of averaging these two quantities over the six samples are plotted in Fig. 4.2. To compute the distributions for the amorphous regions (those that were thermally cycled) we simply removed the atoms in the crystalline regions, and kept the same periodic boundary conditions. For the crystalline regions we removed the atoms in the amorphous regions. The missing neighbors at the edges of each region change the normalization of the curves, but not the overall shape. The pair distribution function for the crystal portions shows tall, sharp peaks at all ranges allowed by the size of the simulation cell. In the amorphous portions a sharp first

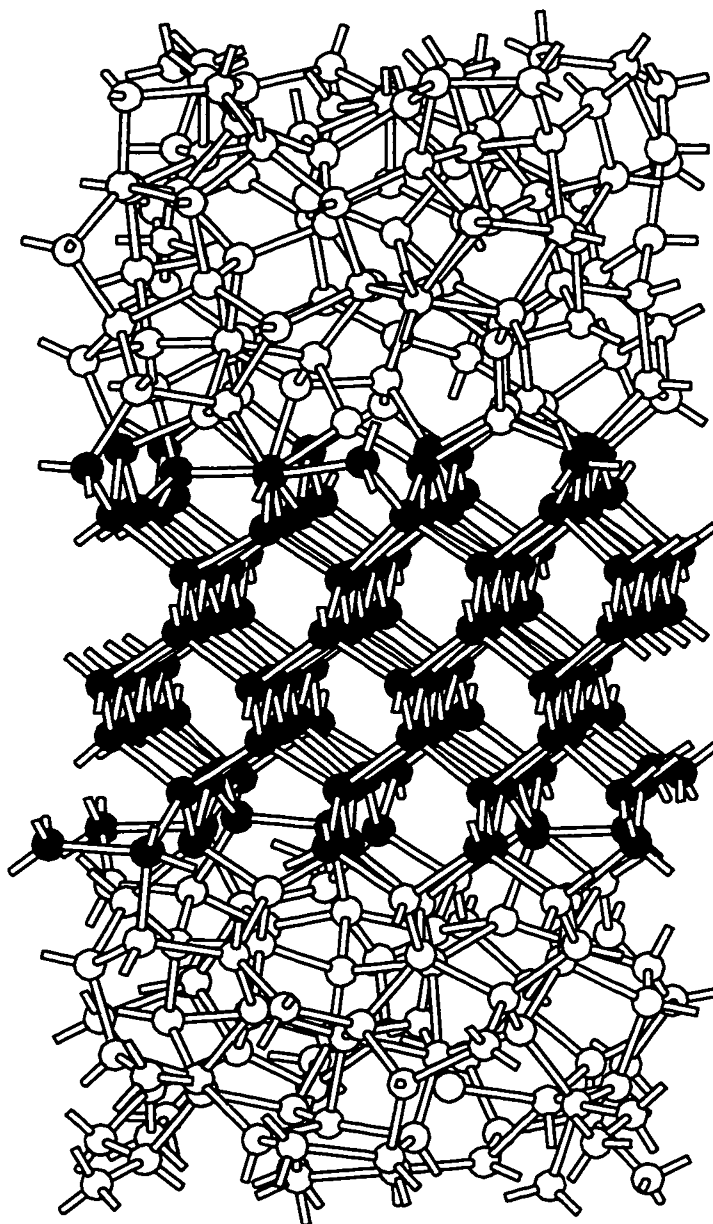

Figure 4.1: View of a sample along a [110] axis of the crystal. Atoms that were kept cool throughout the simulation (corresponding to the crystalline region) are in black, atoms in the region that was heated then cooled (corresponding to the amorphous region) are in white. Bonds are drawn between atoms closer than a distance of 2.7 Å. Periodic boundary conditions apply in all three directions.

neighbor peak and broader second peak are seen, but the third neighbor peak is missing. This pattern has also been observed in DFT/LDA simulations [108] and experiment [109]. Using the position of the minimum in the amorphous radial pair distribution function, at $r = 2.7$ Å, as a geometrical criterion to define bonds between atoms, we calculated the bond angle deviations for the crystal and amorphous portions of our samples. The mean bond angles are $108.9 \pm 6°$ and $108.4 \pm 14°$ in the crystalline and amorphous regions, respectively. These values are quite close to the ideal tetrahedral bonding angle of 109.5°. For the amorphous phase the width of the distribution is a bit smaller than seen in DFT/LDA simulation of a much faster quench, where Stich *et al.* measured deviations of 15.5°, but larger than the value of about 10° seen in experiment [110].

Using the same geometrical criterion to define the neighbors of an atom we calculated the coordination statistics of our samples, listed in table 4.1. The coordination of the atoms in the crystalline regions is essentially perfect, with only a handful of defects. In the amorphous regions about 5% of the atoms have coordination other than four, with over-coordinated defects predominating. Both the total ring statistics and the minimal ring statistics, calculated using shortest path analysis [111], are listed in table 4.1. Each minimal ring is the shortest path starting from some atom along one of its bonds, and coming back to it along another bond. Since the rings are almost as large as the entire crystalline portion of the samples we could not separate the ring statistics of the two regions. While in the crystal we would expect only six-fold minimal rings, in our samples we observe a substantial number of five and seven-fold rings, as well as a few that are smaller or larger. In agreement with the qualitative results of DFT/LDA simulations by Stich *et al.* [108], we see more five than seven-fold rings. However, in the total ring statistics we see more even-membered rings and fewer odd-membered rings than the random bond switching model of Wooten *et al.* [22, 112]. Experimental information about the rings statistics is difficult to obtain. As Mousseau and Lewis [113] showed, even differences between models with many odd-membered rings (as would be appropriate for *a*-Si) and with only even-

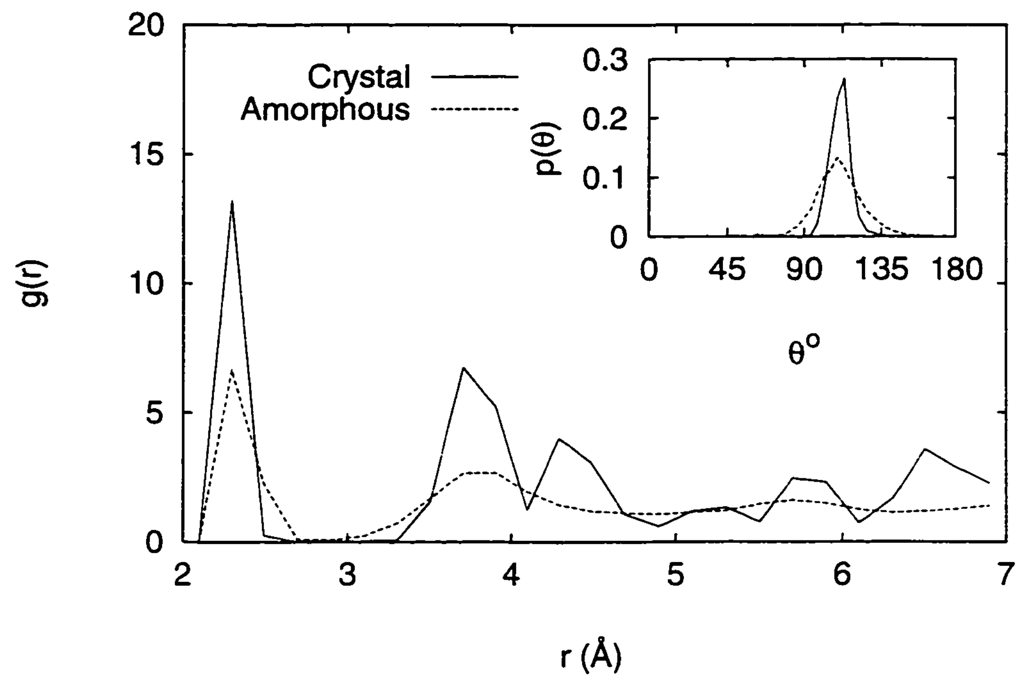

Figure 4.2: Measures of order in the bulk of the crystalline and amorphous regions (as defined in the text): Pair distribution functions $g(r)$ (main panel) and bond angle distribution functions $p(\theta)$ (inset).

Table 4.1: Coordination and ring statistics averaged over six samples. Coordination statistics are tabulated separately for the crystalline and amorphous regions. Note that the rings are too large compared to the thickness of the crystalline region to allow for such a separation, so values averaged over the entire sample are listed.

Coordination Statistics						
Neighbor Num.	2	3	4	5		
crystal	0.1%	0.4%	98.6%	0.9%		
amorphous	0.1%	3.2%	91.7%	4.9%		
Rings per Atom						
Ring Size	3	4	5	6	7	8
all rings	0.01	0.04	0.36	1.11	0.86	2.59
minimal rings	0.01	0.04	0.36	0.99	0.25	0.01

membered rings (as would be appropriate for *a*-GaAs because of chemical ordering) make only very small changes to structural quantities such as the pair distribution function and dihedral angle distribution function.

4.2.2 Localized Properties

Characterizing the *a*-c interface requires different tools than characterizing the adjacent bulk phases. Correlation functions like the radial distribution function and the bond angle distribution are inherently non-local, resulting from averages over large numbers of atoms. Instead, we developed three localized measures of order and computed them for each atom, then averaged over all 6 samples and over 1 Åslabs parallel to the interface. This allows us to see how these measures of order vary as a function of z, the direction perpendicular to the interface.

The first of these measures of order is the RMS deviation $\Delta\theta$ of the bond angles centered at each atom from the ideal tetrahedral angle of 109.5°, plotted in Fig. 4.3 (a). Since the angular forces are strong in a covalent material such as silicon the bond angle deviations are small in both the crystalline and amorphous phases, but the difference between the two is clear. The deviation changes with position perpendicular to the interface, going from the crystalline value to the amorphous value over about 7 Å, in the regions

between $z = 5$ Å and $z = 7$ Å and between $z = 17$ Å and $z = 24$ Å in the figure. The interpolation between the two bulk values differs from the result of Spaepen [15] for a hand built (111) interface relaxed with a Keating potential that showed a larger deviation in the interface region than at either of the adjacent phases.

The second localized measure of order we define to characterize the interface is $\boldsymbol{v}_t$, the sum of the vectors pointing from one atom to its nearest neighbors. This is the simplest measure of the asymmetry of the environment of the atom. If an atom is in perfect sp^3 bonding with four neighbors at 109.5° bond angles, or perfect sp^2 bonding with three neighbors at 120° bond angles, then this vector will be zero. However, if one of those neighbors is missing, it will point directly away from the missing neighbor. Because it is difficult to plot vector quantities, we plot the magnitude of $\boldsymbol{v}_t$ as a function of z position in Fig. 4.3 (b), averaged over all samples and in the x and y directions as described for $\Delta\theta$. The difference between the crystalline and amorphous phases is again small but distinct. The width of the interface as defined by the region over which $\boldsymbol{v}_t$ changes its value is nearly the same as that defined by $\Delta\theta$. While the magnitude of the vector $\boldsymbol{v}_t$ does not add much more information than $\Delta\theta$ did, the vector quantity itself may be helpful in indicating the direction and distance an atom's neighbors would have to move to create a more symmetrical environment, closer to the crystal phase.

The third local quantity we measured is the volume of the Voronoi polyhedron Ω_v associated with each atom, plotted in Fig. 4.3 (c), averaged as described earlier. The Voronoi polyhedron associated with an atom is the region in space that is closer to that atom than to any other. This definition associates a volume with each atom, and each point in space is associated with exactly one atom. This quantity gives a local measure of the space around the atom, inversely proportional to the density. Ω_v is about 19.0 Å^3 in the crystal, corresponding to a 3.5% compression of the unstrained crystal volume per atom of 19.67 Å^3 in our TB model. In the amorphous region Ω_v is between 20.0 and 20.5 Å^3, a few percent less dense than the bulk crystal. This is consistent with the

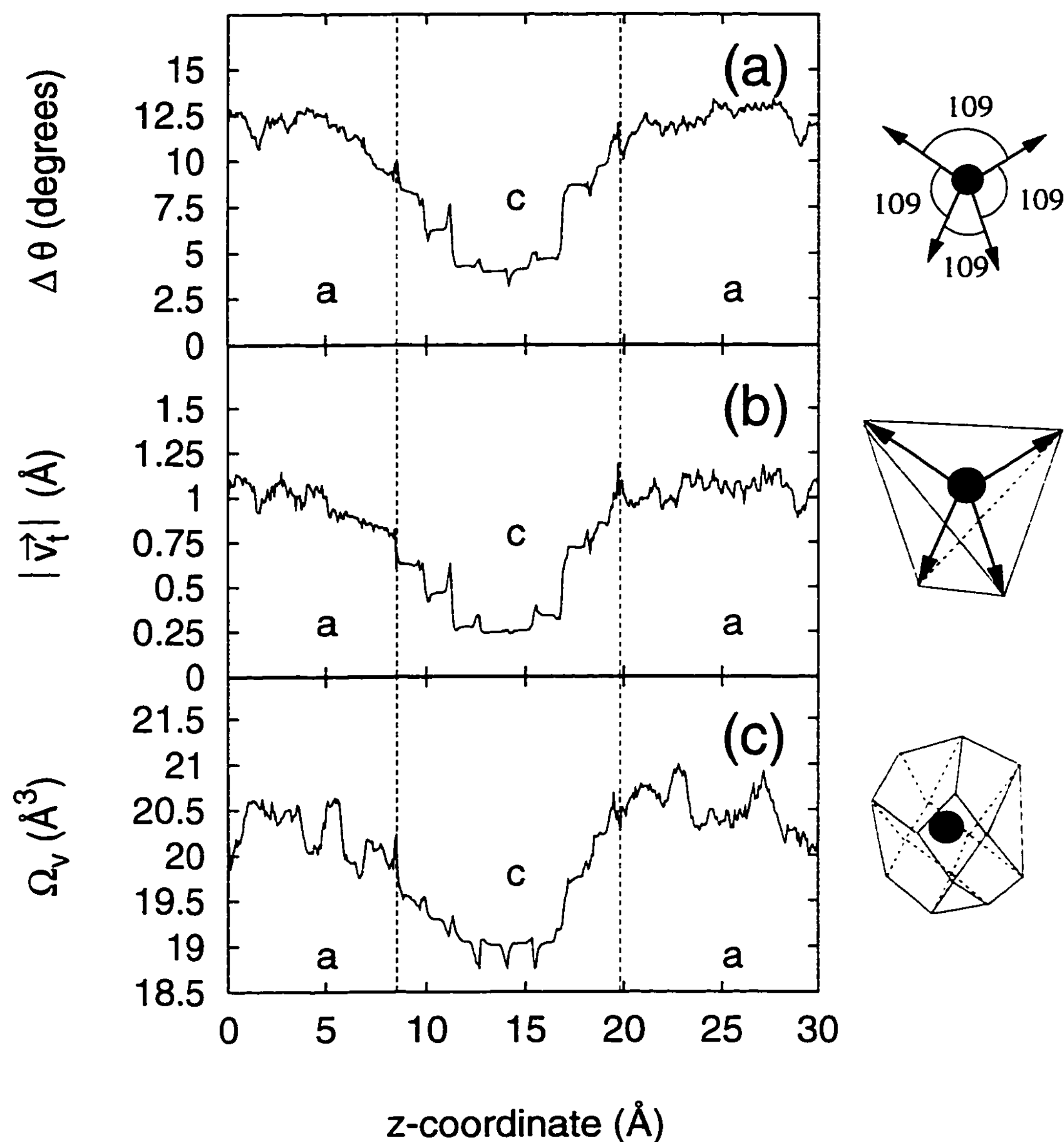

Figure 4.3: Local measures of order through the samples containing a crystal-amorphous interface, averaged over six samples. The ordinate is the z-coordinate of atoms along the [001] direction of the crystal, which is normal to the interface. (a) $\Delta\theta \equiv$ RMS deviation of the nearest neighbor bond angles from the ideal tetrahedral angle of 109.5°; (b) $|\vec{v_t}| \equiv$ Magnitude of the sum of the nearest neighbors vectors; (c) $\Omega_v \equiv$ Voronoi volume (volume of region closer to the atom than to any other atom). The letters 'a' and 'c' indicate the amorphous and crystalline regions of the samples, respectively. The vertical dashed lines correspond to the position of the interface.

experimental measurements of Custer *et al.* [114] who observed that the amorphous phase is 1.8% less dense than the crystal. To resolve the strain on the two phases in more detail, we measured the nearest neighbor spacing projected along the in-plane axes, x and y, and the perpendicular axis z. The crystalline phase is under biaxial compression, with the in-plane spacings about 7% smaller than the spacings along the perpendicular direction. The amorphous phase is under biaxial tension, with the in-plane spacing about 3% larger than along the perpendicular direction. Since the two adjacent phases are under strains of opposite signs it is impossible to conclude anything about the interfacial stress. Had they been strained in the same way, the interfacial stress would have to be of the opposite sign to bring the overall sample to mechanical equilibrium.

To gain insight into the structural details of the a-c interface we visualized slices of the samples parallel to the interface. The picture in Fig. 4.4 reveals some interesting features. The atoms in the crystalline region are arranged in chains along [110] directions, with very few defects. A few dimers appear, where atoms on adjacent chains come together and form a bond, a feature also seen in the hand built model of Saito and Ohdomari [19, 20]. One example is seen in Fig. 4.4 on the left side of the image, between two vertical chains. These dimers are similar to the well known Si(001) 2×1 reconstruction on the free surface, although in this case the dimer atoms are fully bonded, with two neighbors deeper in the crystal, one neighbor in the amorphous, and the other dimer atom forming the fourth bond. The atoms on the amorphous side are much more disordered, although some line up to form [110] chains in configurations that extend the underlying crystal lattice, leading to a question as to whether they should properly be considered amorphous, a matter that I will discuss in the next section.

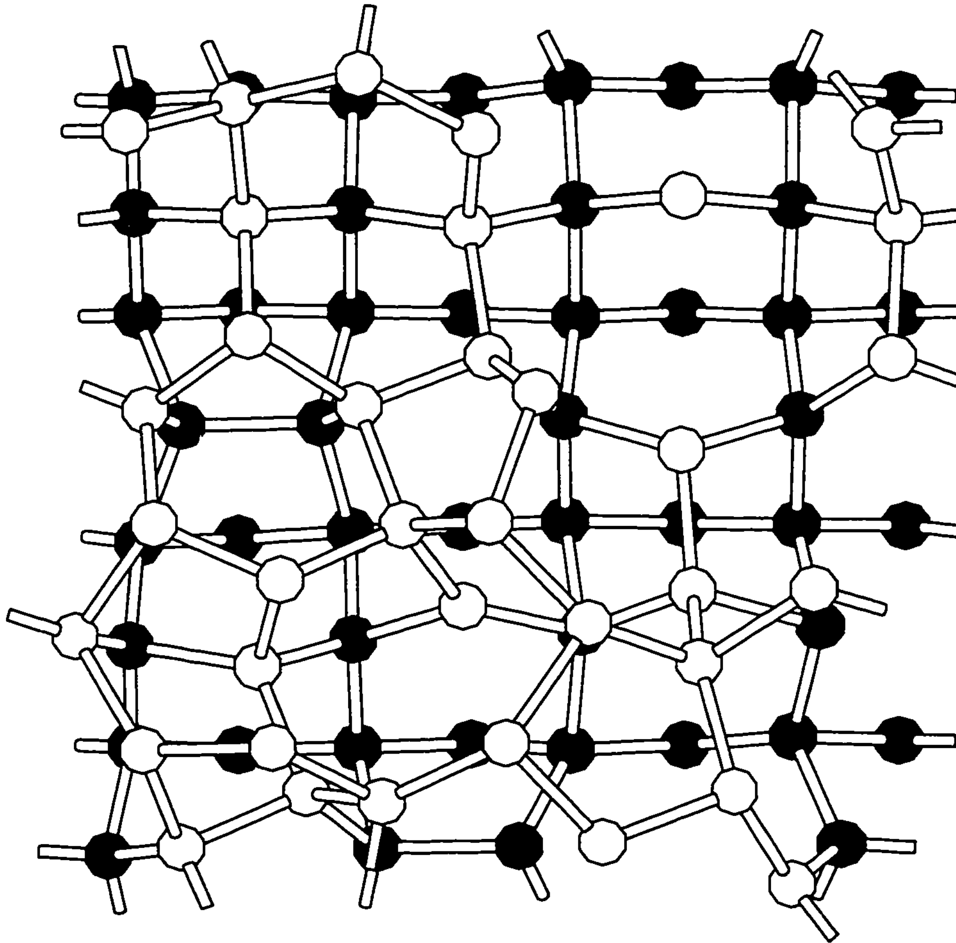

Figure 4.4: Plan-view of an amorphous-crystal interface with the same conventions as in Fig. 4.1. One dimer defect in the crystalline region near the bottom center of the image and one near the left center are easily seen.

4.3 Interface Energies

A completely different quantity characterizing the interface is the interfacial tension

$$\sigma_{ac} = \varepsilon_{ac} + Pv_{ac} - Ts_{ac}, \tag{4.1}$$

where ε_{ac} is the excess interfacial energy per unit area, P is the applied pressure, v_{ac} is the excess volume per unit area, T is the applied temperature, and s_{ac} is the excess entropy per unit area. For a single-component system it is the excess free energy per unit area of a sample with an interface compared with bulk samples of the two adjacent phases.

$$\sigma_{ac} = (G - N_c g_c - N_a g_a)/A, \tag{4.2}$$

where G is the total free energy of a sample with an interface, N_c and N_a are the number of crystal and amorphous atoms, respectively, g_c and g_a are the free energies per atom of the crystal and amorphous phases, respectively, and A is the total area of the interface. This excess energy is the barrier to the nucleation of the crystal in the middle of the amorphous phase. It can be deduced experimentally from nucleation rate measurements under conditions where heterogeneous nucleation, where an impurity or inhomogeneity reduces the nucleation barrier, is insignificant. Because heterogeneous nucleation is hard to eliminate, experimental measurements such as those of Tsao and Peercy [115] or Yang [116] are only a lower limit on the true interfacial tension. The excess free energy includes an internal energy contribution, an excess volume contribution that can be neglected at room pressure, and an entropy contribution that is proportional to temperature. At sufficiently low temperatures the latter can be neglected, and σ_{ac} can be approximated by the excess interfacial energy per unit area ε_{ac}, which is much easier to compute theoretically. This quantity is defined mathematically as the excess energy of a system with an interface compared with a weighted sum of the two constituent phases

$$\varepsilon_{ac} = (E - N_c\varepsilon_c - N_a\varepsilon_a)/A, \tag{4.3}$$

where E is the total cohesive energy of a sample with an interface and ε_c and ε_a are the cohesive energies per atom of the crystal and amorphous phases. When the system is in equilibrium determining N_c and N_a, i.e. assigning atoms to the individual phases, is unnecessary when calculating the true interfacial tension σ_{ac} because the free energies of the component systems are equal. For the silicon a-c interfaces the two phases are not in equilibrium, and we must therefore determine which atoms should be considered "crystalline" and which should be considered "amorphous."

4.3.1 Defining "Crystalline" Atoms

To classify the atoms into the two phases we first need a definition of a "crystalline" atom or an "amorphous" one. All atoms that were kept frozen and were not displaced from their original lattice positions, as well as any atoms that are bonded to two crystal atoms that should share a neighbor, are considered crystalline. All of these atoms are guaranteed to have a nearly ideal crystal bonding environment on at least one side, and all are members of six-fold rings contained in the crystal. The calculated interfacial energy is a small excess energy computed by subtracting two much larger and nearly identical quantities, the energy of the system with an interface and the energy of the constituent phases. This makes it quite sensitive to the precise number of crystal and amorphous atoms, so we must use a more rigorous definition for the bond between two atoms than the geometrical one used earlier that just required the atoms to be closer than 2.7 Å. We calculate the TB charge density half way between each pair of neighboring atoms using representative s and p orbitals centered around each atom, and only consider the two atoms bonded if the charge density is above a threshold value. This definition of a bond typically excludes about 10–20 pairs of atoms that are closer than 2.7Å out of about 650 pairs in each sample. Using this method to partition the atoms between the two phases about 150 atoms in each sample are considered crystalline. Pictures of the crystal atoms of one sample are shown in Fig. 4.5. Almost all of the atoms in the crystal part of the sample

were kept frozen throughout the simulation. Several atoms crystallized during the melting and quenching process, forming additional [110] chains in the layer adjacent to the frozen region. A few additional atoms crystallized on top of these chains, forming the beginning of a second layer.

4.3.2 Reference Bulk Amorphous Sample

The second quantity we need in order to use our TB model to calculate the interfacial energy are the precise values of ε_c and ε_a, the cohesive energies per atom of the reference crystal and amorphous phases. It is trivial to generate the reference crystal phase, an uncompressed diamond lattice (the compression energy is negligible, about 0.015 eV/atom), and easy to compute its energy very accurately. To create the reference amorphous phase from which ε_a can be calculated we use a procedure analogous to the one we used to create the amorphous of the interface samples, but keeping a 4.75 Å slab centered in the middle of the amorphous region frozen while melting and quenching the rest of the sample. This turns the entire sample amorphous, including the crystal part as well as the transition regions between the two phases. Each amorphous sample is then relaxed with the TB model, and used as the reference amorphous phase for the interface sample from which it was created. This way any defects that were quenched into the middle of the amorphous portion of the interface sample are preserved, and their excess energy is partially cancelled out when the amorphous reference energy is subtracted from the interface sample energy. The bulk amorphous samples have cohesive energies between 4.519 and 4.536 eV/atom, corresponding to excess energies for the amorphous phase $\varepsilon_a - \varepsilon_c$ between 0.17 and 0.19 eV/atom. These values are about a factor of two higher than the experimental measurements of Donovan *et al.* [8] of 0.097 eV/atom, measured at 960 K and extrapolated to 0 K using the specific heat reported in that work.

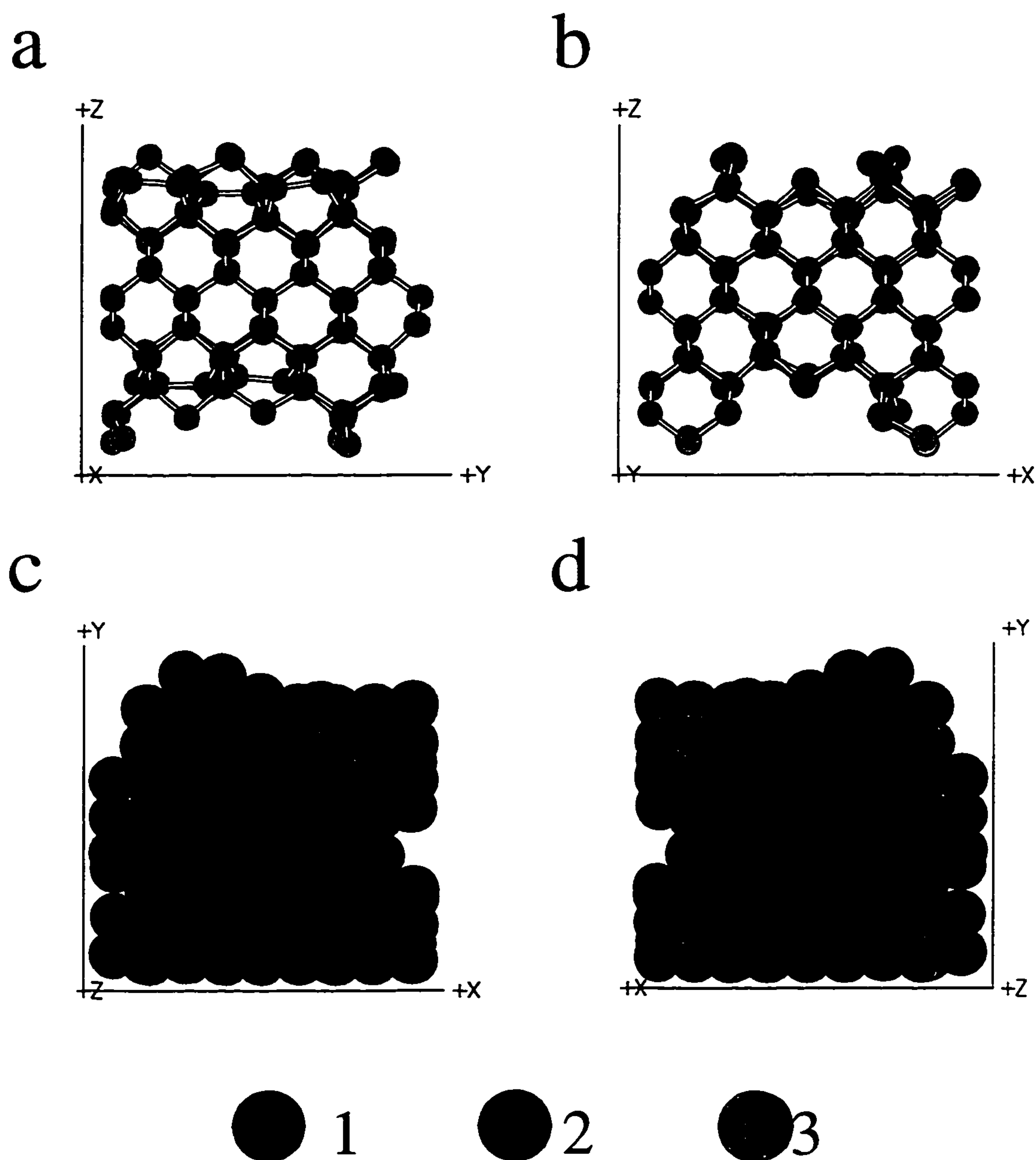

Figure 4.5: The crystalline portion of one interface sample, as defined in sec. 4.3.1. Panels (a) and (b) are views parallel to the interface, along the x and y axes, respectively. Panels (c) and (d) are views perpendicular to the interface from above and below, respectively. Black atoms were in the regions kept frozen through the simulation. Other atoms joined the crystal from the melt during the quenching process, with lighter colors indicating a larger distance from the boundary between the low and high temperature regions.

4.3.3 Interfacial Energy Results

The interfacial energy ε_{ac} as defined by Eq. 4.3 ranges from 0.39 to 0.54 J/m^2 for the six different samples, with a mean of 0.49 J/m^2 and a standard deviation of 0.05 J/m^2. Several factors contribute to the scatter among the interfacial energies for the six samples. The total interfacial energy for the whole sample is a small quantity, about 15 eV, computed by subtracting two much larger quantities, the total energies of the interface sample and the reference phases, each about 1500 eV. Even scatter as small as 0.3% in the larger energies, inevitable due to the disordered nature of the amorphous phase and small size of the systems we can simulate, leads to a 30% scatter in the interfacial energy. Partitioning the atoms into amorphous and crystal portions also contributes to the scatter in the interfacial energies. Since the partitioning process is manual there is the possibility for human error in the application of the definition. The charge density threshold used to define a bond is potentially arbitrary, and can also cause small variations in the number of crystal atoms. A more fundamental issue is the nature of the definition of what constitutes a "crystal" atom. While we feel that the topological definition we used is an intuitively appealing one, other definitions are certainly possible. Several other criteria we considered using to distinguish between the two phases, based on the measures of order we defined in section 4.2.2, led to values for N_c that differed by tens of atoms from the criterion we used, corresponding to a 30% change in the interfacial energy.

We are only aware of one other attempt to compute the interfacial energy theoretically, by Spaepen [15] using a Keating potential to relax a hand built model of a (111) interface and evaluate the energy of each of the atoms. By plotting the energy as a function of position perpendicular to the interface and defining all of the atoms that were added to the underlying crystal lattice as amorphous, Spaepen computed an interfacial energy of 0.31 J/m^2. Saito and Ohdomari [19, 20] also computed the energy as a function of position using a Keating potential for their hand built model of an (001) interface, but did not explicitly compute the corresponding interfacial energy. Using their published data and

considering the "original surface" as part of the crystal we compute an interfacial energy of 0.23 J/m^2. These values are within a factor of two of our simulation results, a reasonable discrepancy considering the difference in interfacial geometry and simulation methods.

Yang fit results from his recent experimental study of the nucleation rate of crystallites in the bulk amorphous phase during ion-beam enhanced crystallization to a physically motivated kinetic model [116]. This fit yielded an interfacial tension of 0.48 J/m^2, in excellent although probably fortuitous agreement with our calculation considering the sources of potentially large errors in our work. The only other experimental result we are aware of is the work by Tsao and Peercy [115] who deduced an interfacial tension of 0.04 J/m^2 from the earlier work of Köster [117]. Köster studied the nucleation rate of crystals in amorphous thin films where nucleation is unlikely to be homogeneous, and so this value should be considered a lower limit rather than an accurate measure of the interfacial tension.

4.4 Summary

Using a combination of interatomic potentials and the NO-TB model we have created *a*-c interfaces in silicon by performing simulations of melt-quench experiments. To better understand the structure of the interface we have analyzed the samples in some detail. To characterize the amorphous character of each atom we calculated several local measures of order, including the deviation of the bond angles from the tetrahedral angle, the sum of the nearest neighbor vectors, and the Voronoi volume. Averaged over planes parallel to the interface and over seven samples, these measures of order show a distinct difference between the amorphous and crystal phases. The transition regions between the two, or the interface regions, are about 7 Å thick, and all measures of order we examined interpolated smoothly between the two bulk phase values.

Slices of the sample along the interface reveal features analogous to dimers on the Si(001) surface and short crystal-like chains in the amorphous layer adjacent to the

crystal. By examining these pictures and using an intuitive criterion of what makes an atom "crystalline" we can separate each sample into an amorphous and a crystal portion. Using reference energies for the amorphous and crystal phases and the definition of each atom as amorphous or crystalline, we compute an interfacial energy of 0.49 J/m^2, in good agreement with experimental evidence and other theoretical work.

Now that we understand the microscopic features of the interface, we can simulate the annealing of interface samples to observe the growth of the crystal in SPEG, and extract microscopic mechanisms for the transformation.

Chapter 5

Solid Phase Epitaxial Growth

5.1 Introduction

Now that we have studied static properties of the *a*-c interface in silicon, we can go on to simulate the time evolution of the interface. Experimentally, the highest observed speed of the interface is about 1 cm/s [5], for (100) interface growth at 1600 K and zero pressure. In units that are more relevant to computer simulations, Å and fs, that equals 10^{-7} Å/fs. One atomic layer in the (100) direction is 1.36 Åthick, so one would need to simulate over 10^7 1 fs time steps to see one monolayer of growth. Since the smallest system that can adequately represent both the amorphous and crystal phases must include at least a few hundred atoms, this is a challenging computational task.

With the latest single CPU workstations we have available, computing the energy and forces on 320 atoms (the size of the interface samples discussed in chap. 4) using TB takes about 3 min of CPU time. This corresponds to about 60 years of CPU time to see one monolayer of growth, far longer than we can afford to wait. Even with large parallel computers, where under idealized circumstances we might hope to get a factor of 100 speedup, the runtime would be about 1 year. Clearly, we can not observe a significant amount of growth in SPEG using TB MD simulation. Two other options are available: using an empirical potential to do MD simulation, or using a TB model with another

simulation technique. The first requires a reliable interatomic potential whose predictions we trust. The second requires some way of guiding the simulation towards the crystallization process, preferably in an unbiased manner. If we had some information about the mechanism, perhaps we could force the system through it and use a program to optimize the path. However, without prior knowledge this is very difficult to do. It may even be difficult to predict which particular sites at an *a*-c interface will crystallize next. One general approach to speed up the dynamics of systems with high energy barriers, developed by Voter [118, 119], is called hyper-MD. In this method a bias potential is applied that is large at the energy minima but zero at the saddle points between metastable states. This speeds up the dynamics without changing the transition rates between metastable states. Unfortunately, the bias potential must be lower than the lowest barrier in the system, and in an amorphous solid with defects those could be quite low. With a low bias potential, the effective speedup of the dynamics is also low.

Since we are unable to use TB to simulate SPEG, we instead decided to use a new empirical potential called the environment dependent interatomic potential (EDIP) [120]. Using this potential we can run 3×10^6 time steps in one CPU day for 800 atom systems. If the energetics of the simulated systems are such that SPEG occurs as fast or faster than observed in experiment, we could see significant amounts of growth within a few days of runtime. Hopefully, if the potential is accurate, we can learn what the mechanism is from these simulations. We can then try to walk through the same mechanisms with a TB simulation method.

5.2 Methods

To do the MD simulation, we use the same algorithms as described in section 4.1. However, instead of using the Stillinger-Weber interatomic potential, we use EDIP. This gives us a better description of both crystalline silicon, including defects, and of amorphous silicon. It is also the only interatomic potential we are aware of that will quench from the

liquid to a four-fold coordinated continuous random network without any special tricks like the increase of the bond-angle forces needed with Stillinger-Weber. Since we are using an empirical potential, we can simulate somewhat larger samples than before to further reduce the chances of the system size affecting the results. However, making interfaces by keeping part of the sample hot and part cold did not work as well as in the smaller samples. The thermal gradients were harder to control, leading to rough interfaces and poor control over the amount of crystallization during the quench. Instead, we used a harmonic potential to tie a few layers of atoms in the crystalline region to their lattice sites. Many layers of atoms still crystallized during the quench, and quenching too slowly led to a complete crystallization of the liquid, rather than the formation of an amorphous phase. This limited the quality of the amorphous phase we could create, since faster quenches lead to more defective samples.

We also used another method for creating *a*-c interfaces, taking a bulk amorphous sample and joining it to a crystal sample. Since the amorphous phase is created by itself, there is no crystal region to act as a seed for the crystallization of the liquid during the quench. This lets us quench more slowly, and anneal the sample to achieve lower defect densities. The interface created by cutting the sample and inserting a crystal slab is very high in potential energy, but a short anneal is sufficient to relax it. We expect that the crystallization of a few layers of amorphous atoms (at most the thickness of the interface we observed in the previous chapter) will bring the *a*-c interface to the structure it has during steady state growth.

With interface samples created in these two ways, we can simulate the annealing of the system under various conditions using MD. Using periodic velocity rescaling, we can run at constant temperature to extract the activation energy for growth. Using Parinello-Rahman dynamics we can keep constant stress, and apply hydrostatic pressure or nonhydrostatic stress to extract the activation volume and strain. Once we have the results of MD simulations, we can also try to extract simple microscopic mechanisms. We

plot the positions of the atoms, averaged over a few hundred time steps to smooth out the thermal motion, and watch as they crystallize. We then pick out a localized region where the crystallization is occuring, and freeze out all other motion. We can then take the steps in the process as it occured in the MD simulation, and plug them into a program that can find a low energy path between atomic configurations. We relax each time averaged snapshot from the MD simulation, giving us a sequence of metastable states along the crystallization path. Adding some number of intermediate configurations between each pair of snapshots, we minimize the energy of each intermediate configuration while keeping the maximum distance in configuration space between subsequent configurations fixed. This gives us a low energy path between the metastable configurations, with a resolution determined by how many intermediate configurations we use.

5.3 Annealing Results

We can get a qualitative idea of the growth rate simply by making pictures of the sample viewed parallel to the interface along high symmetry directions of the crystal, where the difference between the crystal and amorphous phases is readily apparent. Several snapshots from the time evolution of one sample are shown in fig. 5.1, where it is easy to see that growth is occuring. However, growth does not necessarily equal solid-phase epitaxy. To make sure that the amorphous portion is not melting (and that the growth is not actually liquid phase epitaxy), we monitor the average coordination of the atoms in the sample, which undergoes a discontinuous change upon melting of the amorphous. This does not happen during this annealing run, so we can conclude that what we observe is in fact SPEG.

To determine the growth rate of the crystal we plot the number of crystal atoms as a function of time, and fit to a line. To automatically determine the number of crystal atoms we need a localized measure that can distinguish between the crystal and amorphous phases unambiguously. The measures of order discussed in the previous chapter, plotted

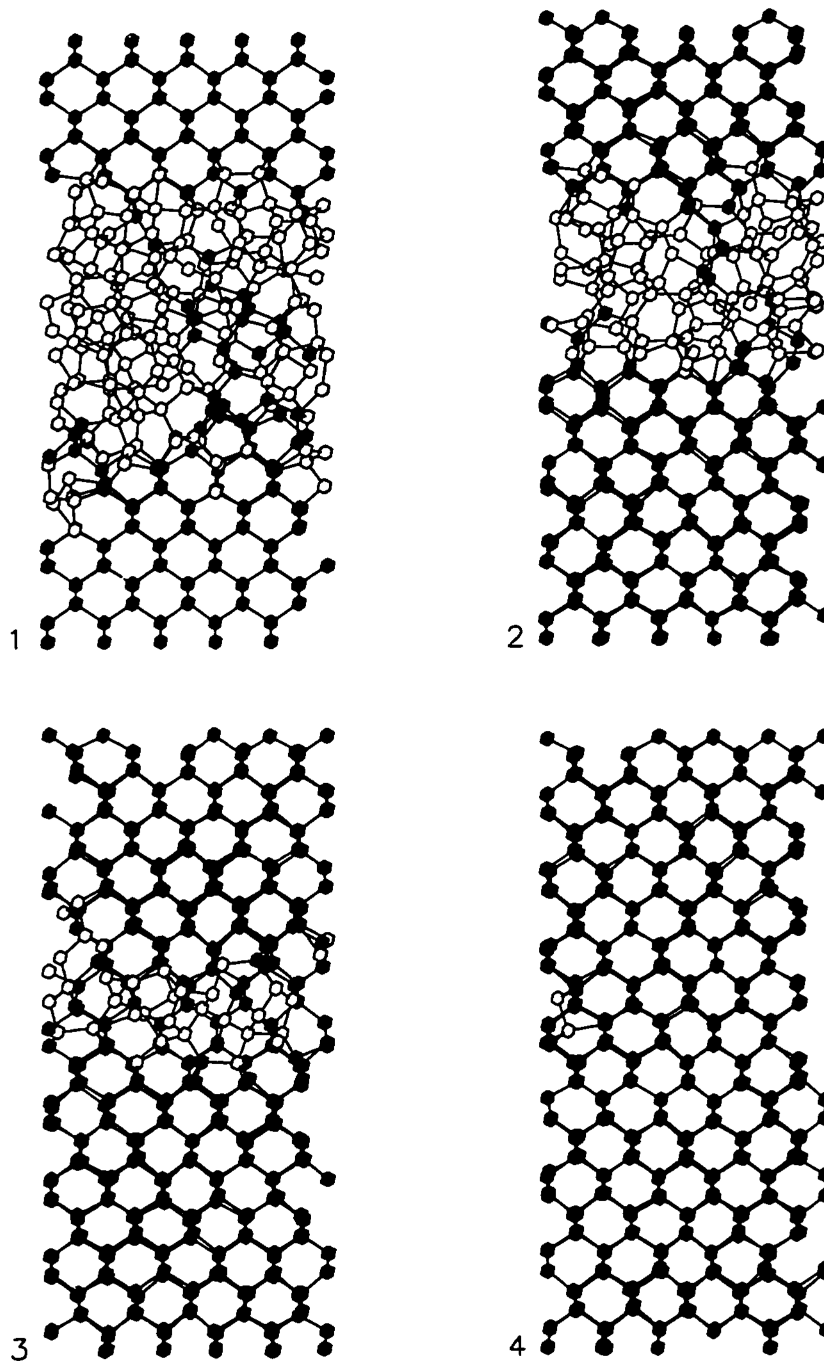

Figure 5.1: Pictures of a slice of an amorphous-crystal interface sample at several points during a constant temperature anneal. Sample temperature is 1000 K, and pictures at 1 ns intervals are shown. Crystalline atoms (as defined by the automated method described in sec. 5.3) are colored in black, amorphous atoms in white.

in Fig. 4.3, are not satisfactory for this purpose. Although when averaged over six samples and in 1 Å thick slabs along z the difference between the crystal and amorphous phases is clear, it is clear from the scatterplot of $\Delta\theta$ in Fig. 5.2 (a) that this is not the case when looking at individual atoms. There is a wide range of values for this measure of order, as well as for the other two discussed in section 4.2.2 that are not shown in the scatterplot, that occur both in the crystal and in the amorphous. Instead we use information about the existing crystal lattice to compute a quantity χ that indicates how well the observed bond directions for each atom are aligned with the known bond directions in the crystal. It is apparent from the scatterplot of χ in Fig. 5.2 (b) that this quantity is much more sensitive to the difference between the two phases. All atoms that are well aligned with the crystal bond directions and are contiguous with the crystalline part of the sample are considered crystalline. In Fig. 5.3 I plot N_c defined in this way as a function time for two particular samples. The growth is clearly evident although the rate fluctuates, particularly for the sample created by doing a melt/quench simulation constraining some of the atoms. In the sample created by sandwiching a bulk amorphous sample with a bulk crystal sample growth is more steady.

5.3.1 Temperature Effects

In Fig. 5.4 I plot the interface speed as a function of inverse temperature for three samples. Two were produced by quenching a liquid at different rates while keeping some atoms constrained to crystal positions, and the third by sandwiching bulk samples of the two phases. Different points for each sample were created by initializing the velocities with distributions corresponding to different temperatures and annealing at that temperature. To improve the statistics we ran each sample several times at each temperature, each time re-initializing the velocities with a different seed for the random number generator. The strongly nonlinear interactions between the atoms leads to chaotic motion that causes these different runs to diverge quickly, and ultimately lead to different samples of the

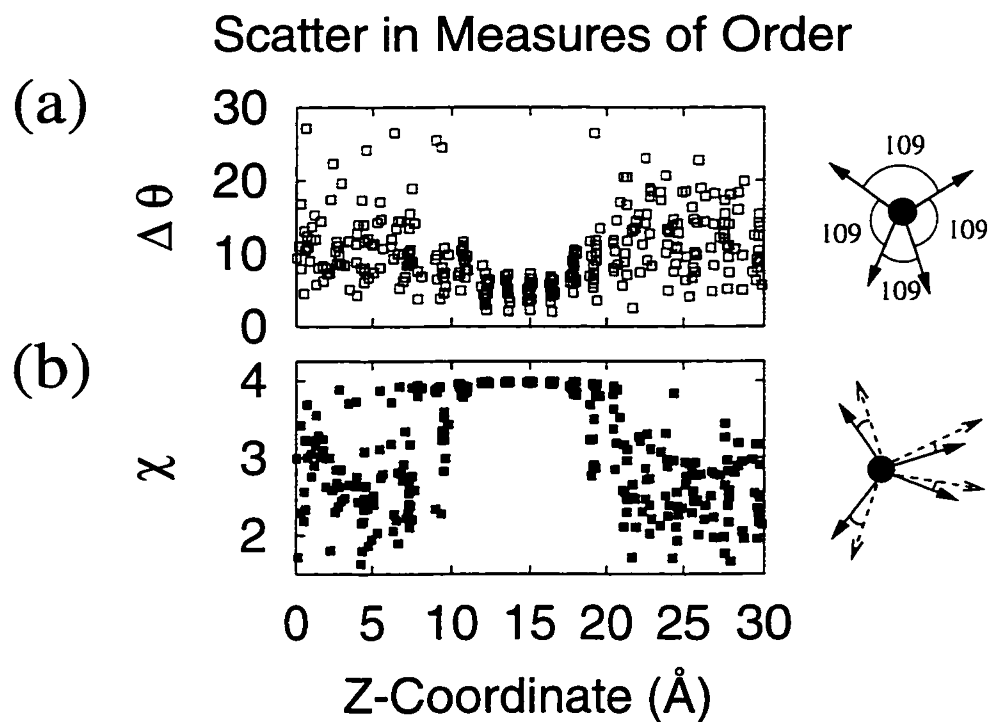

Figure 5.2: A scatterplot of two localized measures of order, the bond angle deviation around each atom $\Delta\theta$, panel (a), and the deviation of the bond angles from the known crystal bond directions χ, panel (b), plotted as a function of z, the position perpendicular to the interface. $\Delta\theta$ should be zero and χ should be four in the ideal crystal.

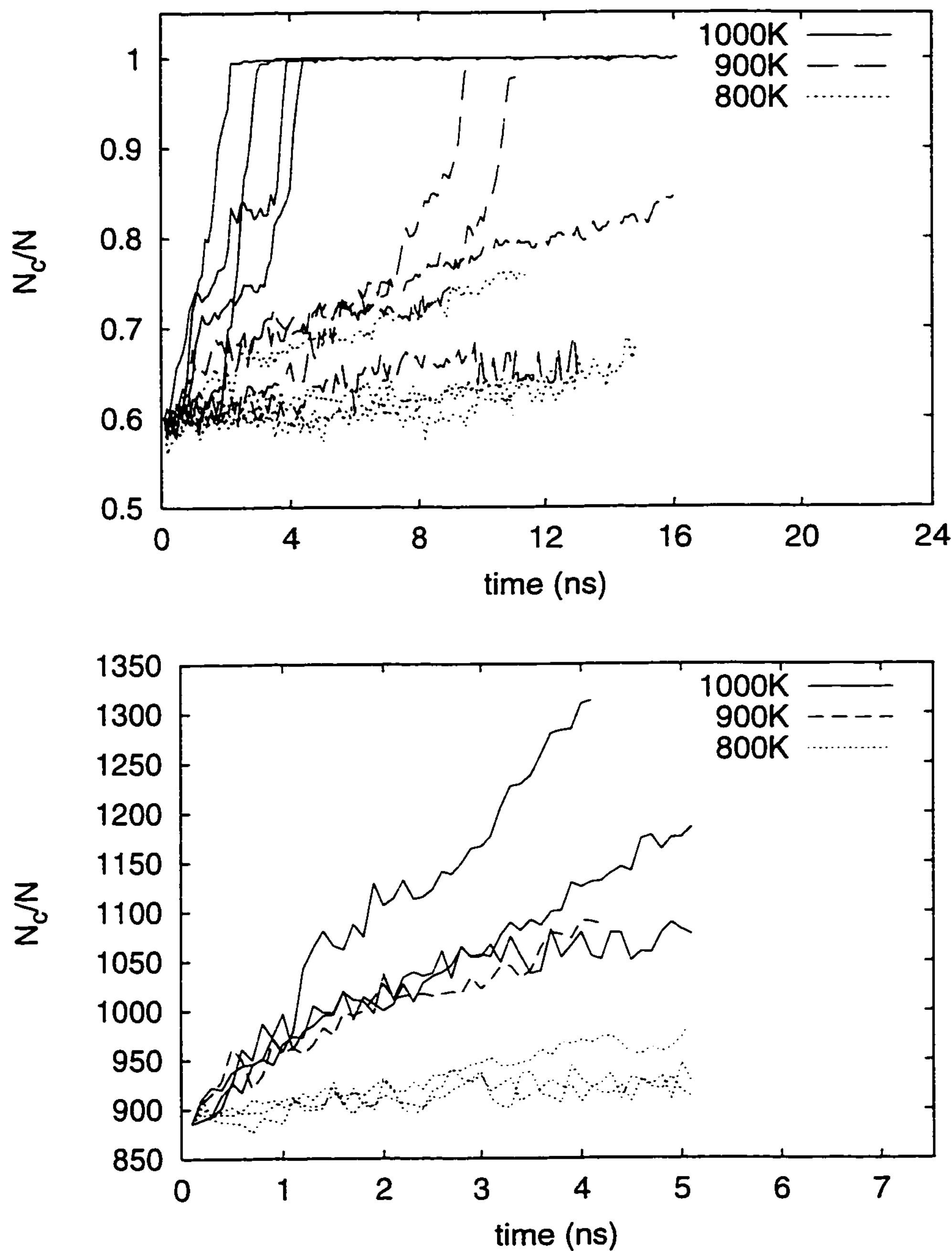

Figure 5.3: Number of crystal atoms vs. time for several constant temperature annealing runs. (a) is from samples created by a melt/quench simulation with some crystal atoms constrained. (b) is from a sample created by sandwiching bulk amorphous and crystal samples. Note that the axes on the two plots are different because of the different sample sizes.

same constant temperature, constant stress ensemble. There is a lot of scatter in the data, particularly for the samples that were created with the constrained quench of the liquid. There is also one outlier for the sample created by sandwiching the bulk phases that lies just below the bottom of the graph, which was neither plotted nor used in the fit. This scatter makes it hard to conclude whether only one mechanism operates in these simulations, as in experiment, but it appears that this is not the case. Particularly evident in the case of the sandwich sample, the slope of the fit is higher at higher temperatures. indicating a higher activation energy.

For the low temperature fits (below 950 K), the activation energies range from 0.1 to 0.4 eV, and for the high temperature fits (above 850 K) they range from 0.8 to 1.7 eV. In contrast the experimental results show only one activation energy, 2.7 eV, over a much wider range of interface speeds. The results from the low temperature fits are an order of magnitude below this value, while the high temperature fits are off by about a factor of two, perhaps reasonable considering the accuracy of EDIP. In any case, it is clear that in our simulations Arrhenius kinetics with one activation mechanism are not valid. One possible explanation for this behavior is that some defect is responsible for the growth. At low temperatures the existing defects that were quenched in during the preparation of the samples dominate, and the activation energy seen is just the migration barrier for these defects. At high temperatures the new defects are created thermally, and the activation energy we observe is the sum of the formation and migration energies for the defects. This would explain the qualitative conflict between our simulation results and experiment: in our samples, defect densities (for example atoms with coordination other than 4) are a few percent, much higher than the densities of 10^{-4} seen in some experiment [121]. The difference in actual defect densities between our simulation and experiment may be smaller than the difference between the measured defect densities implies. The experimental probes used, electron paramagnetic resonance and infrared absorption spectroscopy, since they directly measure unpaired electrons rather than coordination, are insensitive to some types

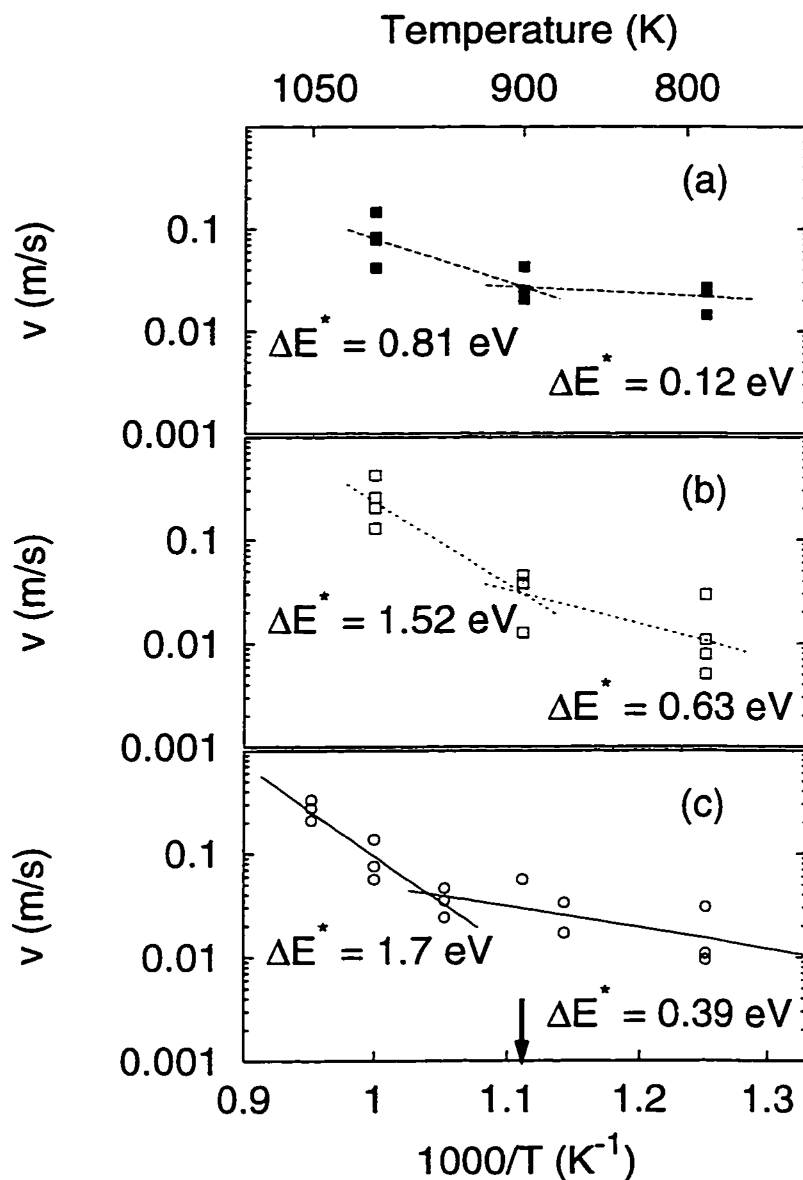

Figure 5.4: Arrhenius fit for growth velocity as a function of temperature (linear least squares fit of $\log(v)$ vs. $1/T$). (a) an 800 atom sample created by quickly quenching a liquid adjacent to some constrained crystal atoms; (b) an 800 atom sample created by slowly quenching a liquid adjacent to some constrained crystal atoms; (c) a 2000 atom sample created by sandwiching bulk amorphous and crystal samples. Each sample is fit separately at low and high temperatures. Note that one outlier in (c) at 900 K, indicated by the arrow, has been excluded from the plot and the fit.

of defects. More accurate simulations [108] using DFT/LDA also indicate somewhat lower defect densities than we observe, but not as low as inferred from experiment. While the quantitative difference may be difficult to measure, it seems likely that the concentration of quenched in defects in experiment is substantially smaller than in our simulations, perhaps too small to ever observe the migration energy dominated temperature range. In ion-beam enhanced crystallization, where it is believed that a large number of defects are created by energetic ions and the activation energy consists solely of a migration energy, ΔE^* is 0.32 eV [122]. This activation energy is much closer to the value we observe in the low temperature simulations, consistent with our explanation for the low activation energy. Another possible explanation, one that, if true, would indicate a more serious problem with our simulation, is that two completely different mechanisms occur at low and high temperatures in the simulations.

5.3.2 Pressure Effects

Using Parinello-Rahman extended system dynamics we can vary the applied stress on the system. By varying the applied hydrostatic pressure and seeing how the growth rate changes, we have measured the activation volume. In Fig. 5.5 we plot the log of the growth rate against the applied pressure at 1000 K for the sample produced by sandwiching bulk amorphous and crystal samples. This is the highest quality sample, and the one which showed an activation energy closest to that seen in experiment. It is also important to note that we performed the pressure variation at a temperature well within range exhibiting the high activation energy. Variable pressure simulations at lower temperatures, where the activation energy is lower, would give the activation volume of the low activation energy mechanism. Except for the three data points at zero pressure (that are the three data points at 1000 K in Fig. 5.4) each data point is generated by simulating the anneal of a sample with the same initial particle positions and velocities. Up to 1.5 GPa, the growth rate increases exponentially with applied pressure, with a corresponding activation volume

$\Delta V^* = -0.71 \pm 0.1\ \Omega_{Si}$. At 2 GPa the rate increases discontinuously, and then resumes increasing exponentially, but with an activation volume $\Delta V^* = -0.26 \pm 0.03\ \Omega_{Si}$. We believe that the low-pressure behavior represents the actual activation volume of SPEG in our simulations. The discontinuity of the growth rate and activation volume at 2 GPa probably indicates a qualitative change in growth, such as the melting of the amorphous phase and the transition to liquid phase epitaxy. It is hard to confirm this hypothesis, since the liquid in EDIP simulations has very low coordination when the trough in the pair correlation function at 2.7 Å is used to define the number of neighbors. However, when a larger cutoff of 3 Å is used, the number of five-fold coordinated atoms is substantially higher in the liquid than in the amorphous phase. From the peak concentration of five-fold defects in each run plotted in Fig. 5.5 it is apparent that a portion of the sample does melt at pressures above 1.5 GPa. The diffusivity in the liquid is also probably quite different, but it is quite difficult to calculate when the number of atoms in the relevant phase is changing rapidly, as is the case for the high pressure, high crystallization rate anneals. The low pressure activation volume, $-0.71\ \Omega_{Si}$ is about double the experimental value of $-0.28 \pm 0.03\ \Omega_{Si}$. While not quantitatively accurate, the activation volume has the right sign and order of magnitude, perhaps as much as we can hope for with an empirical potential simulation.

5.3.3 Nonhydrostatic Stress Effects

Using Parrinello-Rahman dynamics and applying nonhydrostatic stress we probed the shape of the activated state. By applying uniaxial compression perpendicular to the interface, varying σ_{zz}, and biaxial compression parallel to the interface, varying σ_{xx} and σ_{yy}, we extracted the corresponding elements of the activation volume tensor ΔV_{zz}, ΔV_{xx} and ΔV_{yy}. Results of annealing runs at a range of stresses in hydrostatic, uniaxial, and biaxial geometries are plotted in Fig. 5.6. Fitting these results to Arrhenius form results

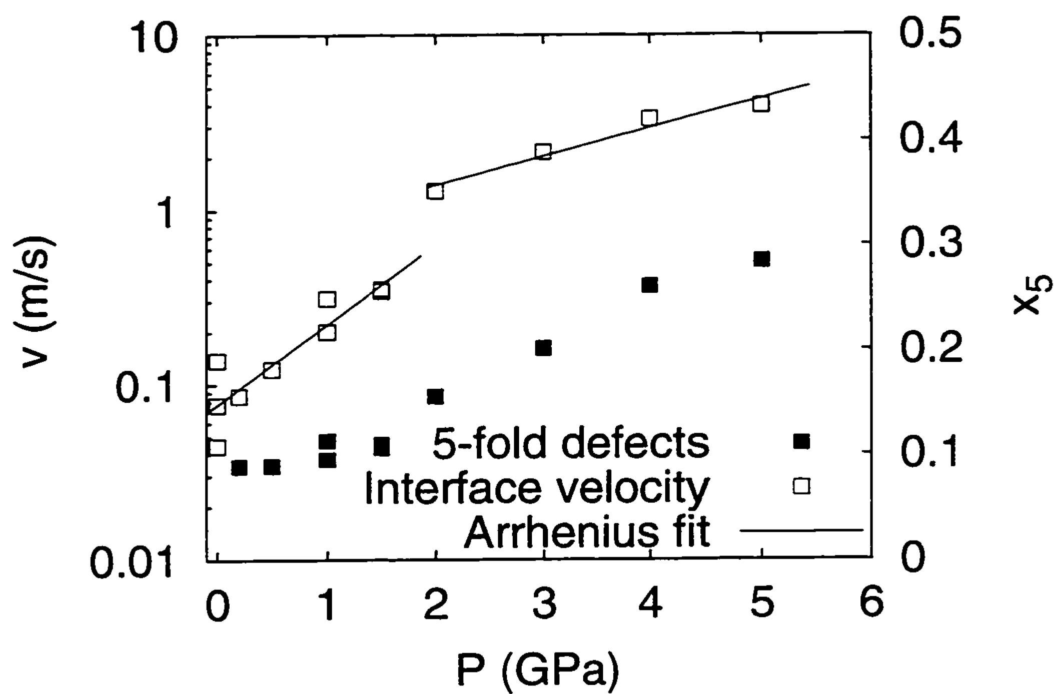

Figure 5.5: Arrhenius fit for growth velocity (left axis) as a function of pressure (linear least squares fit of $\log v$ vs. P). Concentration of five-fold coordinated atoms using a cutoff of 3 Å is also plotted (right axis). 2000 atom sample created by sandwiching amorphous and crystal bulk samples, annealed at 1000 K. Sample is fit separately at low and high pressures.

	ΔV^*	ΔV^*_{zz}	$\Delta V^*_{xx} + \Delta V^*_{yy}$
Simulation (Ω_{Si})	-0.71 ± 0.1	-0.74 ± 0.15	-0.08 ± 0.12
Experiment[a] (Ω_{Si})	-0.28 ± 0.03	-0.35 ± 0.04	+0.28 ± 0.08

[a] V^* from Ref. [9], ΔV^*_{zz} from Ref. [11, 12], $\Delta V^*_{xx} + \Delta V^*_{yy}$ from Ref. [12].

Table 5.1: Activation volume scalar part ΔV^* and diagonal tensor elements $\Delta V^*_{\alpha\alpha}$ from Arrhenius fits of growth rate vs. applied stress tensor components. Simulation measurements were made on a sample created by sandwiching bulk and amorphous samples, annealed at 1000 K. Note that the experimental measurements are not self-consistent.

in activation volume tensor components listed in table 5.1. For consistency, the equation

$$\Delta V^* = \Delta V^*_{xx} + \Delta V^*_{yy} + \Delta V^*_{zz} \tag{5.1}$$

must be satisfied. Within the margins of error detemined by the scatter in the results our strain tensor elements are indeed consistent. In contrast the experimental measurements, also listed in table 5.1, do not satisfy Eq. 5.1, a fact that Carter and Aziz ascribe to a number of experimental difficulties [11, 12]. Both our simulations and experiment deduced an activation state that is "short and fat," although the in-plane components we measure are nearly zero, rather than positive.

5.4 Mechanism

To zoom in on the microscopic mechanism or mechanisms operating in the MD simulation we focused our attention of a limited region in space and time. By looking at the plot of number of crystal atoms as a function of time, we could determine a relatively brief interval where some crystallization appears to be occuring. We then made a movie of the time averaged atomic positions throughout this time interval, and picked out by eye a region where some atoms appear to crystallize, centered around a particular active atom. We then freeze out the motion of all atoms except the active atom and its nearest and next nearest neighbors. These time averaged position snapshots with action only in one localized region are then used as an input to our path-finding program. It relaxes each

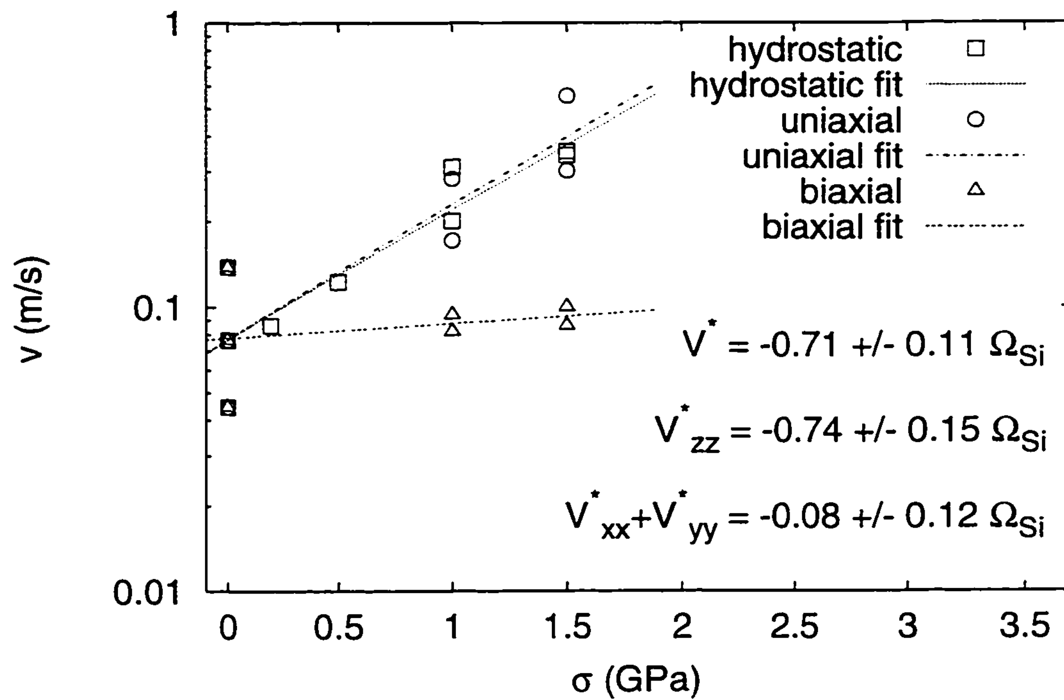

Figure 5.6: Arrhenius fit for growth as a function of different components of the nohydrostatic stress tensor (linear least squares fit of $\log v$ vs. σ). 2000 atom sample created by sandwiching amorphous and crystal bulk samples, annealed at 1000 K.

configuration completely, including the atomic positions and the unit cell size and shape, and then finds low energy pathways between the relaxed configurations. One caution is that the unit cell size and shape are not relaxed through the path, simply interpolated between relaxed values at each metastable configuration.

Using the procedure just described we attempted to extract mechanisms from several runs of several samples. Because the procedure is quite time consuming we were only able to do this a total of four times so far. In three cases the results were uninterpretable. The energy after the hypothetical crystallization effect was not significantly lower than before, and the energies of the relaxed configurations taken from the time averaged snapshots showed no sign of an orderly crystallization process. Instead the energy jumped up and down from one configuration to the next. This may be because what appears to be crystallization to the eye does not necessarily correspond to an immediate lowering of the energy - perhaps some additional strain relief in necessary. It may also be caused by the crude way we attempted to isolate the region participating in the mechanism from the rest of the sample – perhaps choosing the atom and its two nearest neighbor shells is excluding some important atoms, or including part of another, unrelated, mechanism. The four attempts to extract a microscopic mechanism used data from 900 K annealing simulations, a temperature at the crossover between the low and high activation energy regimes. At the time we did not realize that there was such a significant change in growth as a function of temperature, but in retrospect it would have been more useful to focus our attentions on the high temperature anneals where the activation energy is closer to that measured in experiment.

In one of the four attempts, a series of configurations taken from a simulation of the sample with the lowest activation energies, a clear mechainsm emerged. The energy along the path is plotted in Fig. 5.7. The energy plot suggests a simple interpretation: some defect is created, increasing the energy of the sample by about 0.6 eV; the defect hops twice, lowering the energy at each step; the defect is annihilated, reducing the energy of the sample

to below the initial value. Pictures of the atomic configuration at each metastable point generated from a relaxed average position snapshot are shown in Fig. 5.8. Initially, all of the atoms near the active region are four-fold coordinated except for one overcoordinated atom. In the first step of the mechanism one atom moves to a crystal lattice position creating an overcoordinated and undercoordinated atom pair (or a dangling and floating bond pair). The two defects hop around twice, moving more atoms towards crystal lattice positions. However, until the last step only one atom has actually been incorporated into a (110) chain on the crystal side of the interface. Then, the two defects come together, annihilating each other, and add two more atoms to an existing (110) crystal chain. This step corresponds to the final lowering of the energy, after which the system has gained approximately two times the crystallization energy $\Delta\varepsilon_{ac} \approx 0.18\ eV$ (see section 4.3).

While the energetics of this mechanism are at least in qualitative agreement with experiment, the volume changes are not. In Fig. 5.9 we plot the volume changes at the relaxed configurations used to generate the path, as well as the diagonal components of the strain tensor ΔV^*. While the lines in Fig. 5.9 are simply the interpolated values, relaxing the periodic unit cell of the configuration with the highest potential energy only increases its volume by 0.01 Ω_{Si}. The difference between the volume of this configuration and the initial configuration, the activation volume, is clearly positive, while in experiment the activation volume inferred from the variation of the interface speed with applied pressure is negative [9]. In addition, the activated state is longer perpendicular to the interface (along z) and shorter parallel to it, again the opposite of what is seen in experiment [9]. One possible explanation for the inconsistency is that since we are in the low activation energy regime, we are only seeing the effects of defect migration. This would imply that we are missing the formation volume (or strain) of the defect. Another possibility is that the unit cell size and shape should not be interpolated between the metastable configurations, and that had we relaxed the unit cell size and shape all along the path we would have found a very different volume change at the highest energy configuration along the path. A third

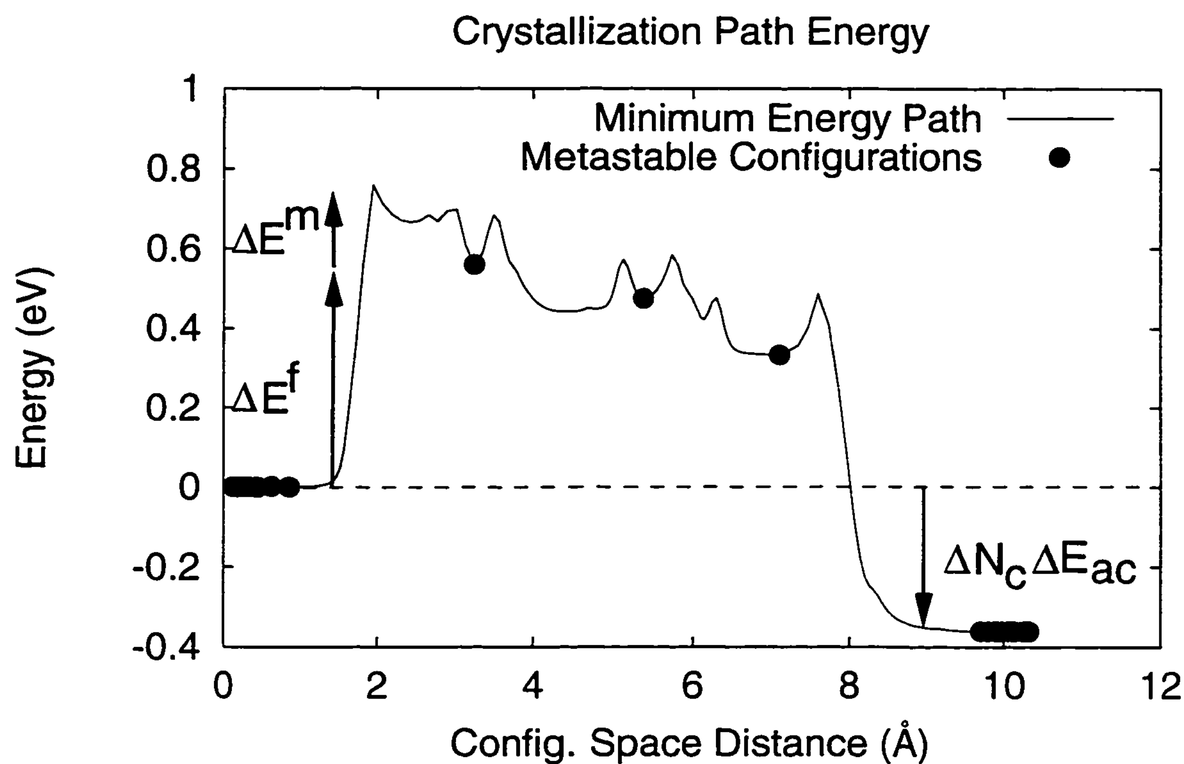

Figure 5.7: Energy along a crystallization path. Solid dots are relaxed configurations taken from time averaged snapshots, with atomic motion outside the active region frozen out. Line is a low energy path connecting these configurations, relaxing atoms along the path, but interpolating the unit cell size and shape. ΔE^f is the formation energy of the defect and ΔE^m is the migration energy. ΔN_c is the change in number of crystal atoms, and ΔE_{ac} is the energy of crystallization per atom for the amorphous phase.

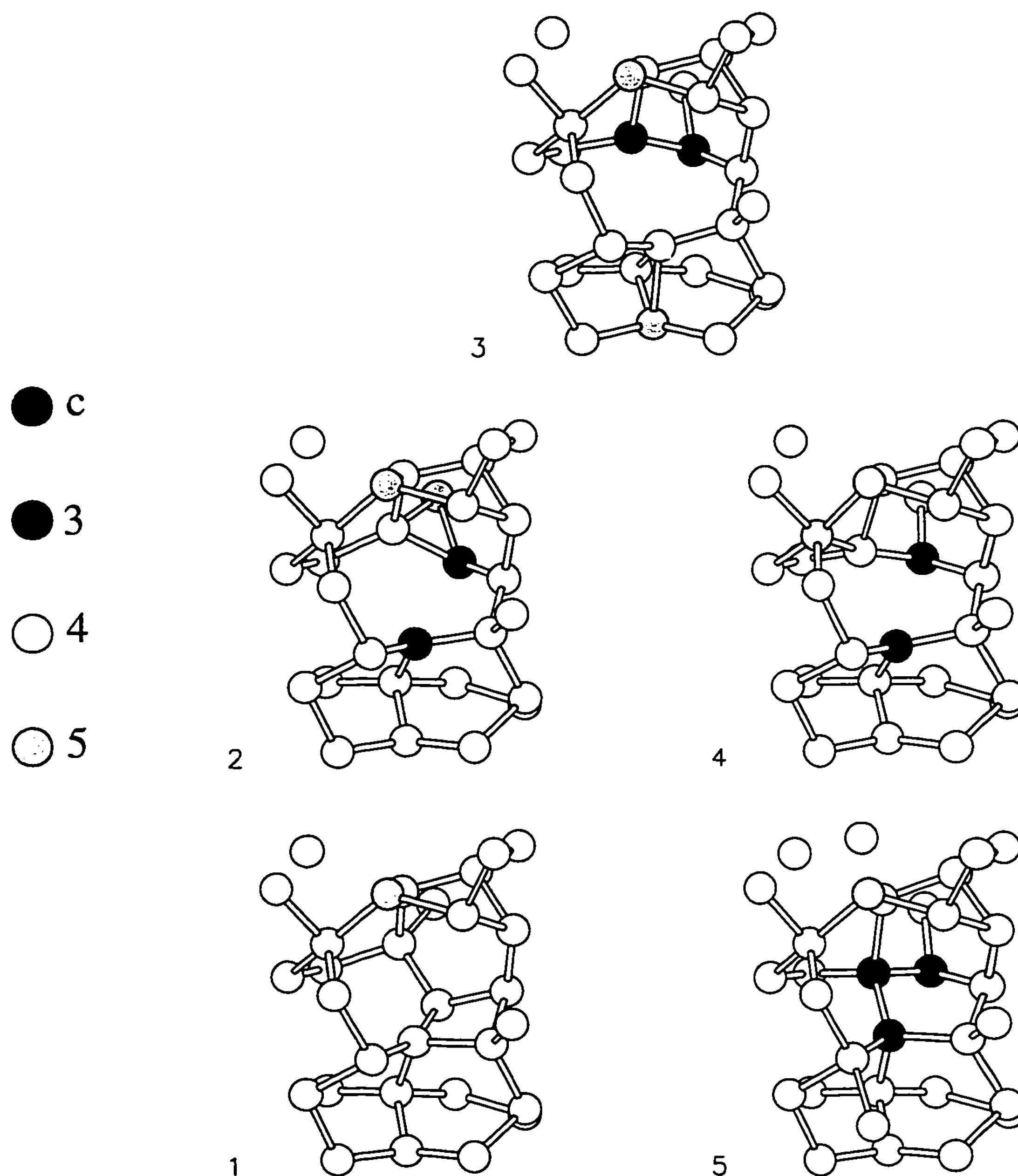

Figure 5.8: Five relaxed atomic configurations along a crystallization path. For clarity, only atoms in a thin slice parallel to the interface are shown. Atoms of type (c) are crystalline, and the others are amorphous atoms with three-fold, four-fold, or five-fold coordination. In configuration 1, a quenched in coordination defect is present. Two coordination defects nucleate in config. 2, and hop around in configs. 3 and 4. In config. 5, the two new coordination defects have annihilated each other, and only the original quenched in defect remains.

possibility is that EDIP, while giving a good description of the energetics of the system, is simply incapable of describing the corresponding structure deformations, although this would be inconsistent with the qualitatively correct activation volumes inferred from the nonhydrostatic stress simulations in sec. 5.3.3.

Several aspects of this mechanism are quite intriguing. The activation energy is quite low compared to the experimental activation energy for SPEG. This particular mechanism did come from the sample that had the lowest activation energy from the Arrhenius fit, and from an annealing run at 900 K, at the transition region between the low and high slopes on the Arrhenius plot. The presence of the floating bond in the initial configuration may be an indication that we are in a regime dominated by existing defects. This floating bond may be weakening the lattice around it enough to allow the defect pair we observe to nucleate with relatively little energy. We will need to explore more instances of crystallization to see if this correlation between existing defects and low activation energy holds. The other interesting observation is that floating bonds and dangling bonds do not need to retain their character. In Spaepen and Turnbull's description of their model [18], a single bond was broken to produce two dangling bonds that keep their character as the crystallization progressed. What we see instead is that an (undercoordinated) atom with a dangling bond can move towards a neighboring atom, satisfying its own dangling bond (and becoming fully coordinated) but causing the neighbor atom to become overcoordinated, creating a floating bond, a process suggested by Pantelides [36]. In fact, as the dangling bonds diffuse in the Spaepen and Turnbull mechanism the system goes through overcoordinated configurations corresponding to floating bonds, although they did not name this defect or emphasize its importance. They implicitly assumed that the undercoordinated configurations are lower in energy than the overcoordinated configurations, and the former should be considered the metastable states along the path.

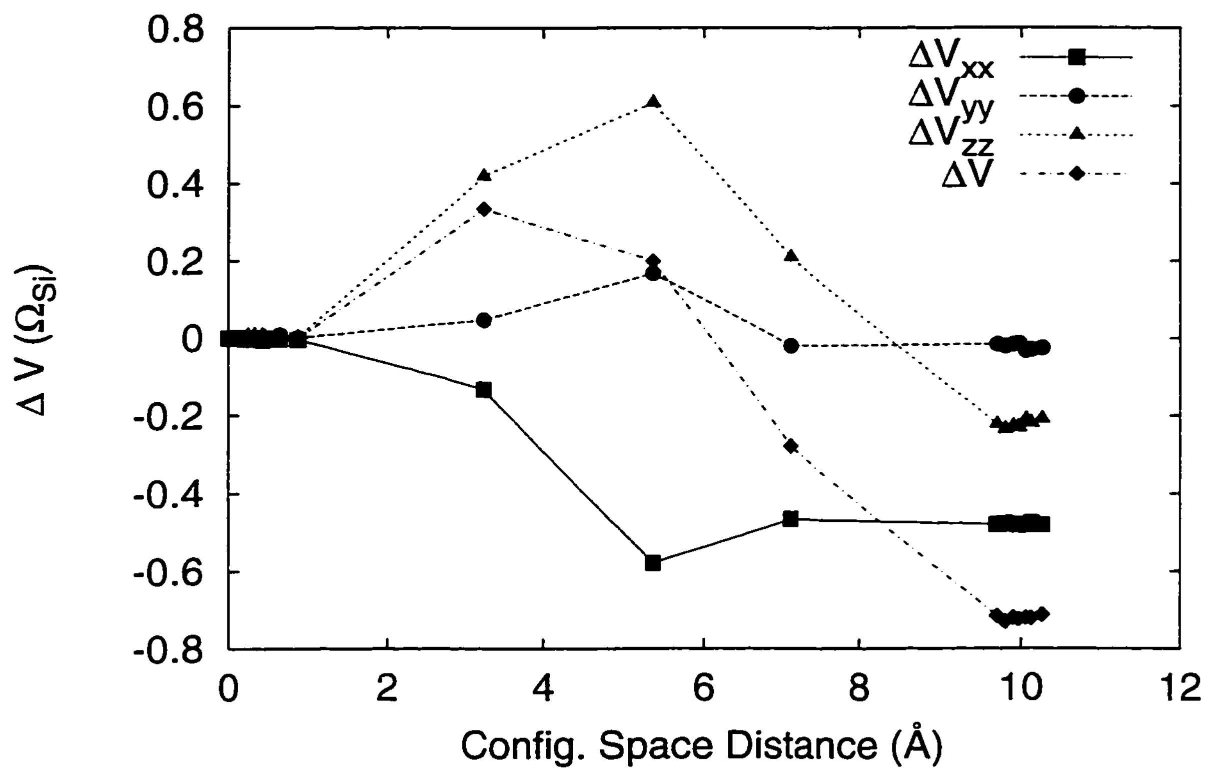

Figure 5.9: Volume and unit cell shape variation along a crystallization path. Note that the unit cell size and shape were only relaxed at the solid points, and the connecting lines are simply interpolations, unlike the energy in Fig. 5.7.

5.5 Discussion

Using EDIP, a new empirical interatomic potential for silicon, we have simulated solid phase epitaxial growth. Since we are using an empirical potential we can simulate larger samples than discussed in the chap. 4. One way to make these samples is by melting and quenching part of the sample while keeping some atoms constrained to their crystal lattice positions with a harmonic potential. Another is to take bulk amorphous and crystal samples and sandwich them together. In a constant temperature anneal, samples generated in both ways show growth of the crystal. The rate of growth is unsteady, and different runs with the same sample at the same applied temperature can give substantially different growth rates. Despite the noise, it is clear that the interface speed increases with increasing temperature.

If Arrhenius kinetics with a single activation energy were to hold, plots of $\log(v)$ vs. $1/T$ would lie along one line with the slope given by the activation energy. We instead observe two regions, a low activation energy region at low temperatures and a high activation energy region at high temperatures. This is most apparent in the sample created by sandwiching two bulk phases samples, where we have done the most runs and scatter is smallest. The activation energies we get are all lower than seen in experiment, off by an order of magnitude in the low T region and a factor of 2 to 4 in the high temperature region. The two slopes may be caused by a crossover from a regime dominated by the migration of existing defects (which occur at much higher concentrations in our simulations than in experiment) to a regime dominated by the formation of new defects to mediate growth. However, more investigation is necessary to conclusively determine what causes the change in activation energy.

By zooming into one region at one interval in time in one run where we see crystallization occur we have extracted a microscopic mechanism for growth. Near an existing floating bond, a dangling bon-dfloating bond pair is nucleated. Both defects hop, facilitating the crystallization of a few atoms, and then annihilate each other. At the

end the system has gained energy equivalent to the crystallization of about two atoms, consistent with the pictures indicating that three atoms have joined (110) crystal chains, but with some distorted bond angles. This mechanism is similar to the one proposed by Spaepen and Turnbull, where the rate limiting step is the formation and migration of the defects at the interface. It's also similar to the framework of the model suggested by Pantelides [32] where floating bonds are the defects reponsible for rearranging the connectivity of the network, although that work is unclear on what precisely is the rate limiting step that governs the growth rate. To determine whether the mechanism we observed is indeed the only mechanism, or even a typical one, we must develop a technique to automate the zoom in process so we can examine many more crystallization events.

Chapter 6

Summary and Conclusions

A wide range of materials phenomena occur in the bulk of solid systems, where atomic resolution probes can not reach. The only way these systems can be studied is over longer length scales, or in terms of the effects of their thermodyanmics. However, these sorts of measurements can be hard to interpret in microscopic terms. A prime example of such a system is SPEG at the interface between the amorphous and crystal phases of a covalent material such as silicon. This system has been studied extensively by measuring the effects of a wide range of parameters on the growth rate of the crystal out of the amorphous phase at the interface. The growth rate increases with temperature, indicating a thermally activated process, where the transformation occurs when the system can overcome an energy barrier. The growth rate varies exponentially with inverse temperature over the entire range where it can be measured, with the same slope over ten orders in magnitude in interface speed. Applied pressure also increases the growth rate exponentially, as does uniaxial compression perpendicular to the interface, but biaxial compression in the plane slows crystal growth. The effects of the interface orientation relative to the crystallographic directions, as well as the effects of doping have also been studied.

Despite this wealth of experimental information, the microscopic mechanism for growth is still unclear. Several types of mechanisms have been suggested in the literature.

All depend on the action of some type of defect to facilitate the growth of the crystal. In some the rate limiting step is the formation and migration of this defect from the bulk crystal or amorphous phases to the interface. In others the rate limiting step is at the interface, when the amorphous atoms are moving into crystal lattice positions. The bulk defect mechanisms can be ruled out because they are not consistent with the measured diffusivity in the crystal phase, the existence of nonhydrostatic stress effects, or the interface orientation effects. The interface defect mechanisms are consistent with all of the observations, but the details of the defects involved and the pathways for crystallization are unclear. An atomistic simulation of the interface structure and its evolution could help shed light on the microscopic mechanisms for SPEG.

6.1 Tight-Binding Models

To be able to simulate the behavior of a collection of atoms we need a formalism for evaluating the energy of the system, as well as the forces on the atoms, given an atomic configuration. The most accurate way of doing this is with an *ab-initio* quantum-mechanical method, such as DFT/LDA, a formalism that has proven to be very accurate for a wide range of materials and structures without the need for fitting. However, it is too slow to simulate the large systems necessary to describe a reasonable amorphous phase, and the time scales necessary to observe SPEG. To speed up the calculation, we developed a simpler quantum-mechanical model for silicon that preserves the important physics based on the nonorthogonal TB method. We also tested two similar models that had been previously presented in the literature. One of these models got most of its parameters *a-priori* from other theories, and the other calculated the parameters by evaluating them using DFT/LDA calculations. Both fit a very small subset of the parameters to experimental measurements and calculations for the energy of the diamond structure and the silicon dimer. In contrast, all of the parameters in our model were fit to a database of experimental and DFT/LDA total energies, as well as some band structure information.

The choice of structures allowed us to optimize our model for the geometries we expect to see in the systems we are interested in studying.

We tested the three TB models and compared their results to DFT/LDA calculations for several bulk structures, some ideal and relaxed point defects, and surface energies. Our results illustrate the need for careful fitting and testing of semiempirical methods such as TB. We found a wide range of behaviors among the three models. Our TB model did quite well for the structures that were in the fitting database, including the bulk diamond and β-Sn structures and the ideal point defects. It did less well for the other bulk structures, although all were higher in energy than the diamond structure in agreement with experiment and DFT/LDA simulation. The point defect relaxation energies, which were not in the fitting database, were also reasonable. The other two TB models did much less well in reproducing the bulk structures we tested. They also overestimated the ideal defect formation energies by as much as a factor of three. While it would be ideal to have a fast parameter free model, our test show the importance of fitting in the development of a semiempirical method such as TB. To test our TB model on configurations that vary substantially from those in the fitting database we calculated the surface energies for two low energy surfaces of silicon, as well as the energies of some reconstructions on those surfaces. As in the case of the point defects the other two TB models calculated higher energies than our TB model, although in this case our model underestimated the surface energies while the other two models were more accurate. This result underscores the importance of extensive testing of semiempirical methods like TB. A model that works well for a particular set of geometries is not guaranteed to work in other situations, and the range of structures tested must be designed to encompass the structures expected in the application of the model.

6.2 Amorphous-Crystal Interfaces

Using a combination of the Stillinger-Weber empirical interatomic potential and our TB model we created a number of *a*-c interface samples. Using the empirical potential and MD we simulated the melting and quenching of part of a silicon sample. We then relaxed the resulting interface samples to the nearest local energy minimum using the TB model. This procedure was many orders of magnitude faster than using TB to simulate the whole process but still gave us reasonable results. We then analyzed the resulting interface structures, and calculated the interfacial tension between the amorphous and crystal phases.

Bulk measures such as the pair correlation function and bond angle distribution indicated that we had a high quality amorphous phase, as did measurements of the co-ordination statistics in the sample. These measurements, however, do not shed light on the details of the interface structure. We therefore used three local measures of order: the bond angle deviation, the sum of the nearest neighbor vectors, and the Voronoi volume associated with each atom. The first gives a local measure of angular distortion. The second is a measurement of the local asymmetry around the atom. The third is a local measure of the space around the atom which is inversly proportional to the density. All three measures showed distinct differences between the two phases when plotted as a function of the distance perpendicular to the interface, averaged over planes parallel to the interface and over the different samples. In all cases the values appeared to interpolate smoothly between the two bulk values over a thickness of about 7 Å. There was no sign of the excess bond angle deviation seen by Spaepen in his hand built model of the (111) interface, or the excess free volume seen by Erkoç at the interface. While the methods we used to simulate this system are far from perfect, we feel that they are an improvement over past work, and that the differences among the results should perhaps be investigated with more accurate methods such as DFT/LDA, although this would be a substantial undertaking.

To better understand the atomistic features of the interface we examined pictures

of slices of the samples parallel to the interface. The most obvious structural feature seen was chains of atoms along [110] directions in the crystal. In a few places we observed dimer defects in these chains where two atoms from adjacent chains came together, presumably during the melt or quench when bonds to the adjacent liquid phase were relatively weak. On the nominally amorphous side of the interface substantial numbers of atoms were actually in crystal lattice positions, although most were in more disordered configurations.

The interfacial tension between the amorphous and crystal phases is an important property of the interface, affecting the nucleation of one phase in the other. To calculate it, we subtracted the energy of reference bulk crystal and amorphous phases from the energy of a sample with an interface. To appropriately weight the reference sample energies we needed to partition the atoms into amorphous and crystal portions. To do that we used a topological criterion, where each atom that was bonded to two crystal atoms on one side was considered crystalline. This ensured that each crystal atom saw a crystal-like environment on at least one side. The interfacial tension we calculated was 0.49 J/m^2, about a factor of two higher than previous calculations for hand built models, and in almost perfect agreement with values extracted from fitting of experiments to a physically motivated theory. This agreement is almost certainly fortuitous, since very small errors in determining the energy of the reference samples, particularly likely for the amorphous phase, as well as the potentially arbitrary nature of the partitioning of atoms into crystal and amorphous portions, implies an uncertainty in the interfacial tension of at least 30%. Improvements in this value could be made by using larger samples to reduce the statistical noise, and by the addition of entropic factors which are difficult to compute but potentially important at finite temperatures. Ultimately, this will remain a difficult measurement, because as long as the two phases are not in equilibrium the atoms in the samples will need to be partitioned. Since the a-c interface appears to be several Å thick, an unambiguous distinction between the two phases will probably remain hard to formulate.

6.3 Solid Phase Epitaxial Growth

With an understanding of the structure of the *a*-c interface. we proceeded to directly simulate SPEG and try to extract a mechanism for growth. Assuming growth would proceed at a rate similar to that seen in experiment, the TB model is too slow to use for direct simulation. Instead we used EDIP, an empirical interatomic potential that was optimized for the same geometries as our TB model, and is substantially more accurate than Stillinger-Weber for these systems. We created two samples by simulating a melt-quench process, keeping some of the atoms constrained to form the crystal part of the sample, and varying the quench rate. We also created a sample by sandwiching a bulk amorphous sample to a bulk crystal sample and relaxing the resulting system.

Upon annealing these samples at temperatures from 800–1050 K we observed growth of the crystal. At the high temperature anneal we could follow the growth of a large number of crystal layers. and found that the grown material was nearly free of imperfections. There was a lot of variation among runs at the same temperature started with different initial velocities for the atoms. The variation is due to the small sample size and the chaotic nature of the strongly nonlinear atomic motion. The growth rate follows Arrhenius kinetics, but each sample shows two different activation energies. a low one at low temperatures and a high one at high temperatures. This conflicts with experimental results that show only one activation energy over a much wider range of temperatures. Perhaps the low temperature regime is dominated by existing defects. which are much more plentiful in our samples than in experiment, and the activation energy, which is five to ten times lower than in experiment, is simply the migration energy of these defects. At high temperatures the thermally generated defects dominate over the quenched defect population, and the activation energy, which is about 40% lower than in experiment. is the sum of the formation and migration parts. It is possible that if measurements could be made on more defective samples at low temperatures the low activation energy regime could be seen in experiment.

The largest sample we examined, created by sandwiching bulk amorphous and crystal samples, had the least scatter and an activation energy that most closely matched experiment. We used this sample, at a temperature corresponding to the high activation energy, to study the effect of applied pressure and nonhydrostatic stress on growth. Applying hydrostatic pressure sped up growth, with a high activation volume at low pressures and a lower one at high pressures. We suspect that the high pressure behavior indicates the melting of the amorphous, although this is not seen in experiment up to substantially higher temperatures. However, the liquid phase is not well described by EDIP, so this transition is probably unrealistic. The activation volume observed at low pressures is about twice as large as in experiment, but of the same sign. The effects of nonhydrostatic stress are also consistent with what is seen in experiment: the activated states is "short and fat," although in EDIP simulations the in plane components of the activation strain are nearly equal to zero, rather than positive as in experiment. Even this qualitative agreement between the EDIP simulation and experiment on such a subtle aspect as the structure of the activated state is quite encouraging. It indicates that our simulations are probably capturing the essential physics of the growth process.

To extract a microscopic mechanism we zoomed in on specific regions and times in several annealing runs where we determined by eye that some atoms had crystallized. We then froze the motion of the atoms away from the active region, and relaxed the configurations taken from the MD run. Unfortunately the only set of configurations that showed clear evidence of crystallization was from a run at a temparature where the activation energy is low. By finding a low energy path connecting these configurations we extracted a mechanism for crystallization. In the vicinity of an overcoordinated atom a pair of defects forms, one dangling bond and one floating bond. These defects make several hops, facilitating the crystallization of several atoms, and annihilate each other, leaving the original floating bond in place. This mechanism is quite similar to the dangling bond mechanism proposed by Spaepen and Turnbull and the floating bond mechanism proposed

by Pantelides. However, in our simulations the identity of the active defects is maleable, transforming between floating and dangling bonds.

6.4 Future Directions

While I hope that this work has helped further the understanding of some aspects of *a*-c interfaces in silicon, it is clear that many questions remain. The development of TB models for covalent systems still clearly requires a large amount of guesswork. Our work has shown that fitting and testing are vital for the development of semi-empirical methods like TB, but more work on the optimal functional forms is necessary. A far better solution would be a method for calculating TB interactions without fitting, especially important for multicomponent systems where the number of parameters would be excessive. The particular model we tested has some important shortcomings, but perhaps some elaboration such as a larger basis set or an electron-electron interaction correction could improve it.

Using empirical potentials to create *a*-c interface samples is a straightforward process. Thanks to new potentials such as EDIP it can be done with a direct simulation, without the need for tricks such as increasing the bond angle forces, as was needed for previous empirical potentials. Since empirical potentials do have some potentially significant problems, specifically an inaccurate description of the liquid and no interaction past the first neighbor shell, they will not necessarily give correct amorphous structures, although the results so far are plausible. A detailed comparison of these structures to fully quantum-mechanical calculations, either with TB or DFT/LDA, with more atoms than have been simulated in the past could resolve whether more subtle aspects of the structure are correct. While simple quantities such as the coordination statistics appear to be reproduced by empirical potential simulations, the accuracy of ring statistics is harder to judge because of the paucity of data from the small samples that have been simulated so far with QM methods. The robustness of specific features of our interfaces, such as the dimers between crystal chains, could also be verified. Appropriate simulations would require at

least tens of thousands of MD steps for annealing an existing sample, more for simulating the entire melt-quench process. They would be quite time consuming, although perhaps feasible with TB simulations using linear scaling algorithms on more advanced computers than are available now. Unfortunately, it is hard to predict *a-priori* how much difference the QM treatment would make, although it would be useful as a reliable confirmation.

Direct simulations of SPEG using EDIP have shown that we can reproduce qualitative features of growth such as the activation energy and strain. More work remains to be done in extracting mechanisms from these simulations. One approach would be to automate the selection of a region and a time to focus on, so more possible pathways could be tested. Another is to take two configurations separated in time by a larger interval and use a more sophisticated transition path finding algorithm, perhaps one based on extensive annealing of the path rather than just a simple energy minimization, to find crystallization mechanisms. Unfortunately, there is no simple way of using the information from the empirical potential simulations to guide a QM simulation. Upon relaxing an empirical potential sample with a TB model the details of the network connectivity change so much that it is impossible to apply a mechanism that occured in the empirical potential simulation to the TB relaxed configuration. Direct simulation of tens of crystallization events with TB simulations is slow, but only a factor of ten improvement in computer speed could make it feasible to do one of these simulations in a few CPU days.

Bibliography

[1] G. A. Baraff and M. Schlüter, Phys. Rev. B **30**, 3460 (1984).

[2] V. Fiorentini and A. Baldereschi, Phys. Rev. B **51**, 17196 (1995).

[3] N. W. Ashcroft and N. D. Mermin, in *Solid State Physics* (Saunders College, Philadelphia, 1976), p. 76.

[4] J. W. Mayer, L. Eriksson, and J. A. Davies, Can. J. Phys. **45**, 663 (1968).

[5] G. L. Olson and J. A. Roth, Mater. Sci. Rep. **3**, 1 (1988).

[6] G. L. Olson, S. A. Kokorowski, R. A. McFarlane, and L. D. Hess, Appl. Phys. Lett. **37**, 1019 (1980).

[7] L. Csepregi, R. P. Küllen, J. W. Mayer, and T. W. Sigmon, Solid State Comm. **21**, 1019 (1977).

[8] E. P. Donovan *et al.*, J. Appl. Phys. **57**, 1795 (1985).

[9] G. Q. Lu, E. Nygren, and M. J. Aziz, J. Appl. Phys. **70**, 5323 (1991).

[10] M. J. Aziz, P. C. Sabin, and G. Q. Lu, Phys. Rev. B **44**, 9812 (1991).

[11] W. B. Carter and M. J. Aziz, in *Thin Films: Stresses and Mechanical Properties V*, MRS Symposia Proceedings No. 356 (Materials Research Society, Pittsburgh, 1995), p. 87.

[12] W. B. Carter, Ph.D. thesis, Harvard University, 1997.

[13] J. A. Roth, G. L. Olson, D. C. Jacobson, and J. M. Poate, Appl. Phys. Lett. **57**, 1340 (1990).

[14] J. A. Roth *et al.*, in *Kinetics of Phase Transformations*, MRS Symposia Proceedings No. 205, edited by M. O. Thompson, M. J. Aziz, and G. B. Stephenson (Materials Research Society, Pittsburgh, 1992), p. 45.

[15] F. Spaepen, Acta Metall. **26**, 1167 (1978).

[16] F. Spaepen, in *Amorphous Materials, Modeling of Structures and Properties*, edited by V. Vitek (TMS-AIME, New York, 1983), p. 265.

[17] P. N. Keating, Phys. Rev. **145**, 637 (1966).

[18] F. Spaepen and D. Turnbull, in *Laser-Solid Interactions and Laser Processing-1978*, A.I.P. Conference Proceedings Vol. 50, edited by S. D. Ferris, H. J. Leamy, and J. M. Poate (A.I.P., New York, 1979), p. 73.

[19] T. Saito and I. Ohdomari, Phil. Mag. B **43**, 673 (1981).

[20] T. Saito and I. Ohdomari, Phil. Mag. B **49**, 471 (1984).

[21] F. Wooten and D. Weaire, J. Non. Cryst. Solids **114**, 681 (1989).

[22] F. Wooten, K. Winer, and D. Weaire, Phys. Rev. Lett. **54**, 1391 (1985).

[23] N. Metropolis *et al.*, J. Chem. Phys. **21**, 1087 (1953).

[24] Ş. Erkoç, T. Halicioglu, and W. A. Tiller, J. Non. Cryst. Solids **94**, 28 (1987).

[25] G. H. Gilmer and C. Roland, Appl. Phys. Lett. **65**, 824 (1994).

[26] M. H. Grabow, G. H. Gilmer, and A. F. Bakker, in *Atomic scale calculations in materials science*, MRS Symposia Proceedings No. 141, edited by J. Tersoff, D. Vanderbilt, and V. Vitek (Materials Research Society, Pittsburgh, 1989), p. 349.

[27] M.-J. Caturla, T. D. de la Rubia, and G. H. Gilmer, J. Appl. Phys. **77**, 3121 (1995).

[28] F. H. Stillinger and T. A. Weber, Phys. Rev. B **31**, 5262 (1985).

[29] L. A. Marqués, M.-J. Caturla, T. D. de la Rubia, and G. Gilmer, J. Appl. Phys. **80**, 6160 (1996).

[30] J. S. Williams and R. G. Elliman, Phys. Rev. Lett. **51**, 1069 (1983).

[31] L. E. Mosley and M. A. Paesler, Appl. Phys. Lett. **45**, 86 (1984).

[32] S. T. Pantelides, in *Fundamentals of Beam-Solid Interactions and Transient Thermal Processing*, MRS Symposia Proceedings No. 100, edited by M. J. Aziz, L. E. Rehn, and B. Stritzker (Materials Research Society, Pittburgh, 1988), p. 387.

[33] J. Narayan, J. Appl. Phys. **53**, 8607 (1982).

[34] C. Licoppe and Y. I. Nissim, J. Appl. Phys. **59**, 432 (1986).

[35] M. Tang, L. Colombo, J. Zhu, and T. D. de la Rubia, Phys. Rev. B **55**, 14279 (1997).

[36] S. T. Pantelides, Phys. Rev. Lett. **57**, 2979 (1986).

[37] B. Park, Ph.D. thesis, Harvard University, 1989.

[38] E. Nygren, B. Park, L. M. Goldman, and F. Spaepen, Appl. Phys. Lett. **56**, 294 (1990).

[39] A. Witvrouw and F. Spaepen, in *Kinetics of Phase Transformations*, MRS Symposia Proceedings No. 205, edited by M. O. Thompson, M. J. Aziz, and G. B. Stephenson (Materials Research Society, Pittsburgh, 1992), p. 21.

[40] A. Witvrouw and F. Spaepen, J. Appl. Phys. **74**, 7154 (1993).

[41] L. Csepregi, E. F. Kennedy, J. W. Mayer, and T. W. Sigmon, J. Appl. Phys. **49**, 3906 (1978).

[42] N. W. Ashcroft and N. D. Mermin, in *Solid State Physics* (Saunders College, Philadelphia, 1976), p. 425.

[43] P. Hohenberg and W. Kohn, Phys. Rev. **136**, B864 (1964).

[44] W. Kohn and L. J. Sham, Phys. Rev. **140**, A1133 (1965).

[45] J. C. Slater and G. F. Koster, Phys. Rev. **94**, 1498 (1954).

[46] W. A. Harrison, in *Electronic Structure and the Properties of Solids* (Freeman, San Francisco, 1980), Chap. B.

[47] X.-P. Li, R. W. Nunes, and D. Vanderbilt, Phys. Rev. B **47**, 10891 (1993).

[48] M. Daw, Phys. Rev. B **47**, 10895 (1993).

[49] R. W. Nunes and D. Vanderbilt, Phys. Rev. B **50**, 17611 (1994).

[50] J. Kim, F. Mauri, and G. Galli, Phys. Rev. B **52**, 1640 (1995).

[51] S. Goedecker and L. Colombo, Phys. Rev. Lett. **73**, 122 (1994).

[52] A. M. Stoneham, V. T. B. Torres, P. M. Masri, and H. R. Schober, Phil. Mag. A **58**, 93 (1988).

[53] H. Balamane, T. Halicioglu, and W. A. Tiller, Phys. Rev. B **46**, 2250 (1992), see also references therein.

[54] M. P. Allen and D. J. Tildesley, in *Computer Simulations of Liquids* (Oxford University Press, Oxford, 1987), p. 78.

[55] M. P. Allen and D. J. Tildesley, in *Computer Simulations of Liquids* (Oxford University Press, Oxford, 1987), p. 82.

[56] S. Nosé, Mol. Phys. **52**, 255 (1984).

[57] M. P. Allen and D. J. Tildesley, in *Computer Simulations of Liquids* (Oxford University Press, Oxford, 1987), p. 46.

[58] H. C. Andersen, J. Chem. Phys. **72**, 2384 (1980).

[59] M. Parrinello and A. Rahman, Phys. Rev. Lett. **45**, 1196 (1980).

[60] M. Parrinello and A. Rahman, J. Appl. Phys. **52**, 7182 (1981).

[61] M. Parrinello and A. Rahman, J. Chem. Phys. **76**, 2662 (1982).

[62] W. H. Press, B. P. Flannery, S. A. Teukolsky, and W. T. Vetterling, in *Numerical Recipes in C* (Cambridge University Press, Cambridge, 1988), p. 317.

[63] W. H. Press, B. P. Flannery, S. A. Teukolsky, and W. T. Vetterling, in *Numerical Recipes in C* (Cambridge University Press, Cambridge, 1988), p. 343.

[64] M. Karplus and R. Elber, Chem. Phys. Lett. **139**, 375 (1987).

[65] W. A. Harrison, *Electronic Structure and the Properties of Solids* (Freeman, San Francisco, 1980).

[66] C. M. Goringe, D. R. Bowler, and E. Hernaández, Rep. Prog. Phys. **60**, 1447 (1998).

[67] C. Z. Wang, K. M. Ho, and C. T. Chan, Comp. Mat. Sci. **2**, 93 (1994).

[68] C. Z. Wang *et al.*, in *Materials Theory, Simulations, and Parallel Algorithms*, MRS Symposia Proceedings No. 408, edited by E. Kaxiras, J. Joannopoulos, P. Vashishta, and R. Kalia (Materials Research Society, Pittsburgh, 1996), p. 37.

[69] J. L. Mercer, Jr., and M. Y. Chou, Phys. Rev. B **49**, 8506 (1994).

[70] A. P. Sutton, M. W. Finnis, D. G. Pettifor, and Y. Ohta, J. Phys. C **21**, 35 (1988).

[71] L. Goodwin, A. J. Skinner, and D. G. Pettifor, Europhys. Lett. **9**, 701 (1989).

[72] C. Z. Wang, K. M. Ho, and C. T. Chan, Phys. Rev. Lett. **70**, 611 (1993).

[73] I. Kwon *et al.*, Phys. Rev. B **49**, 7242 (1994).

[74] M. Menon and K. R. Subbaswamy, Phys. Rev. B **47**, 12754 (1993).

[75] M. Menon and K. R. Subbaswamy, Phys. Rev. B **50**, 11577 (1994).

[76] M. Menon and K. R. Subbaswamy, Phys. Rev. B **55**, 9231 (1997).

[77] P. Blaudeck *et al.*, J. Phys.: Condens. Matter **C4**, 6389 (1992).

[78] T. Frauenheim *et al.*, Phys. Rev. B **52**, 11492 (1995).

[79] N. Bernstein and E. Kaxiras, in *Materials Theory, Simulations, and Parallel Algorithms*, MRS Symposia Proceedings No. 408, edited by E. Kaxiras, J. Joannopoulos, P. Vashishta, and R. Kalia (Materials Research Society, Pittsburgh, 1996), p. 55.

[80] N. Bernstein and E. Kaxiras, Phys. Rev. B **56**, 10488 (1997).

[81] R. Hoffman, J. Chem. Phys. **39**, 1397 (1963).

[82] W. A. Harrison, in *Electronic Structure and the Properties of Solids* (Freeman, San Francisco, 1980), Chap. 20.

[83] W. A. Harrison, in *Electronic Structure and the Properties of Solids* (Freeman, San Francisco, 1980), Chap. 3.

[84] H. Hellmann, in *Einfürung in die Quantenchemie* (Deuticke, Leipzig, 1937), pp. 61,285.

[85] R. P. Feynman, Phys. Rev. **56**, 340 (1939).

[86] W. A. Harrison, in *Electronic Structure and the Properties of Solids* (Freeman, San Francisco, 1980), solid State Table of the Elements.

[87] S. M. Hu, Materials Science and Engineeting R: Reports **R13**, 105 (1994).

[88] K. C. Pandey, Phys. Rev. Lett. **57**, 2287 (1986).

[89] S. Roorda *et al.*, Phys. Rev. B **44**, 3702 (1991).

[90] J. C. Jamieson, Science **139**, 762 (1963).

[91] M. I. McMahon and R. J. Nelmes, Phys. Rev. B **47**, 8337 (1993), see also references therein.

[92] M. T. Yin and M. L. Cohen, Phys. Rev. B **26**, 5668 (1982).

[93] L. L. Boyer *et al.*, Phys. Rev. Lett. **67**, 715 (1991).

[94] N. Moll *et al.*, Phys. Rev. B **52**, 2550 (1995).

[95] F. D. Murnaghan, Proc. Nat. Acad. Sci. U.S.A. **30**, 244 (1944).

[96] A. Fukumoto, Phys. Rev. B **42**, 7462 (1990).

[97] Y. Bar-Yam and J. D. Joannopoulos, Phys. Rev. Lett. **52**, 1129 (1984).

[98] P. J. Kelly and R. Car, Phys. Rev. B **45**, 6543 (1992).

[99] H. Seong and L. J. Lewis, Phys. Rev. B **53**, 9791 (1996).

[100] M. Nastar, V. V. Bulatov, and S. Yip, Phys. Rev. B **53**, 13521 (1996).

[101] I. P. Batra, Phys. Rev. B **41**, 5048 (1990).

[102] J. Dąbrowksi and M. Scheffler, Appl. Surf. Sci. **56–58**, 15 (1992).

[103] G. Binnig, H. Rohrer, C. Gerber, and E. Weibel, Phys. Rev. Lett. **50**, 120 (1983).

[104] K. Takayanagi, Y. Tanishiro, M. Takahashi, and S. Takahashi, J. Vac. Sci. Tech. A **3**, 1502 (1985).

[105] J. E. Northrup, Phys. Rev. Lett. **57**, 154 (1986).

[106] I.-W. Lyo, E. Kaxiras, and P. Avouris, Phys. Rev. Lett. **63**, 1261 (1989).

[107] W. D. Luedtke and U. Landman, Phys. Rev. B **37**, 4656 (1988).

[108] I. Štich, R. Car, , and M. Parrinello, Phys. Rev. B **44**, 11092 (1991).

[109] S. Kugler *et al.*, Phys. Rev. B **40**, 8030 (1989).

[110] J. Fortner and J. S. Lannin, Phys. Rev. B **39**, 5527 (1989).

[111] S. V. King, Nature **213**, 1112 (1967).

[112] F. Wooten and D. Weaire, Solid State Phys. **40**, 1 (1987).

[113] N. Mousseau and L. J. Lewis, Phys. Rev. Lett. **78**, 1484 (1997).

[114] J. S. Custer *et al.*, Appl. Phys. Lett. **64**, 437 (1994).

[115] J. Y. Tsao and P. S. Peercy, Phys. Rev. B **58**, 2782 (1987).

[116] C. M. Yang, Ph.D. thesis, California Institute of Technology, 1997.

[117] U. Köster, Phys. Status Solidi A **48**, 313 (1978).

[118] A. F. Voter, Phys. Rev. Lett. **78**, 3908 (1997).

[119] A. F. Voter, J. Chem. Phys. **106**, 4665 (1997).

[120] M. Z. Bazant, E. Kaxiras, and J. F. Justo, Phys. Rev. B **56**, 8542 (1997).

[121] C. N. Waddell *et al.*, J. Appl. Phys. **55**, 4361 (1984).

[122] F. Priolo and E. Rimini, Mater. Sci. Rep. **5**, 319 (1990).

IMAGE EVALUATION
TEST TARGET (QA-3)

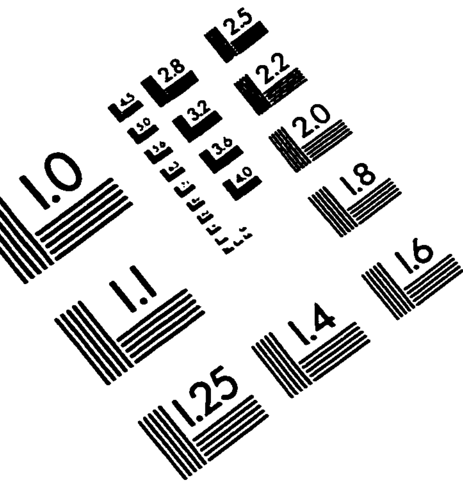
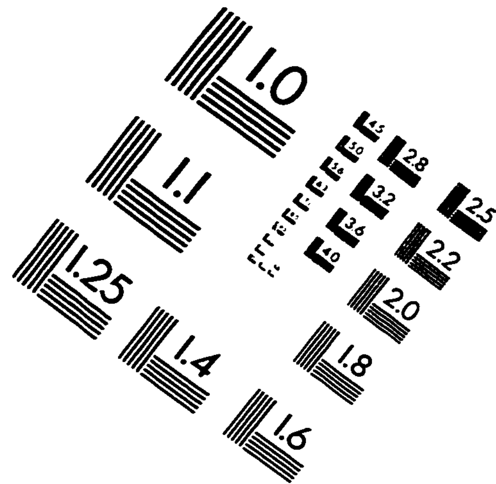
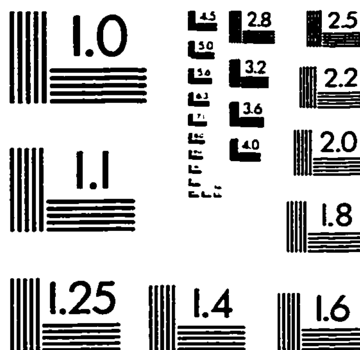
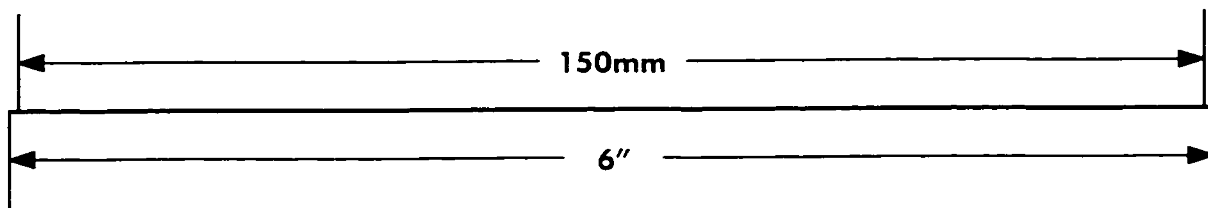

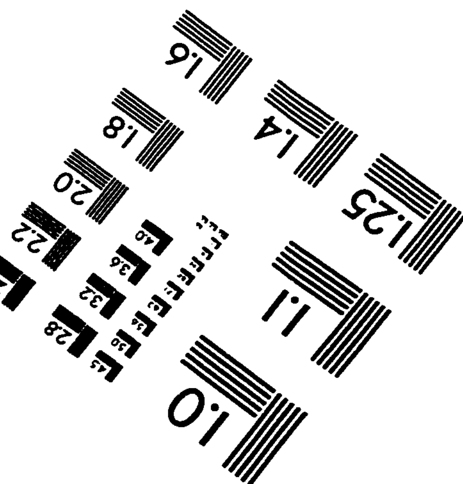

APPLIED IMAGE, Inc
1653 East Main Street
Rochester, NY 14609 USA
Phone: 716/482-0300
Fax: 716/288-5989

© 1993, Applied Image, Inc., All Rights Reserved